Preparation of Entangled States and Quantum Teleportation with Atomic Qubits

Dissertation

zur Erlangung des Doktorgrades an der
Fakultät für Mathematik, Informatik und Physik
der Leopold-Franzens-Universität Innsbruck

vorgelegt von

Mark Riebe

durchgeführt am Institut für Experimentalphysik
unter der Leitung von
o. Univ. Prof. Dr. R. Blatt

Innsbruck
Mai 2005

Abstract

Quantum information processing has been the subject of intense study for the past ten years. Entanglement is an essential ingredient in order to achieve the exponential speed-up promised by certain quantum algorithms. One system proposed for the implementation of quantum information processing is a string of ions in a linear Paul trap. In this thesis the ability to deterministically prepare and manipulate entangled states of two and three ions with such an experimental setup is investigated.

The essential tools for an ion trap quantum computer, in particular a two ion controlled-NOT gate, were demonstrated. The entangled states could be controlled with such precision that it was possible to realize a deterministic quantum state teleportation between ions. The experiments described were carried out with $^{40}Ca^+$ ions stored in a linear Paul trap. The physical representation of the qubits was with the $S_{1/2}$ ground state and the metastable $D_{5/2}$ state of the Ca^+ ions. The operations necessary for entangling the ionic qubits were implemented with a series of laser pulses at 729 nm, addressing the quadrupole transition between the $S_{1/2}$ and $D_{5/2}$ states.

With this experimental setup two ionic qubits were prepared in all four Bell states and three ionic qubits were prepared in both possible classes of tripartite entangled states, namely GHZ- and W-states. The entangled states were investigated using quantum state tomography, which provided complete information about the quantum system in the form of its density matrix. The lifetime of these entangled states were studied. As predicted by theory, some particular types of entangled state were found to be particulary stable against the predominant source of noise in our experiment, namely correlated phase noise due to laser frequency fluctuations.

A technique to measure the state of one ionic qubit without affecting the other qubits in the ion string was implemented. The effect of such a measurement on GHZ- and W-states was studied. Furthermore the experimental setup was improved, such that single-qubit operations could be applied depending on the outcome of a previous measurement of one or more qubits. This technique was used to transform a GHZ-state into a pure bipartite entangled state using only local operations.

Finally, the advanced techniques developed to manipulate the entanglement of the ionic qubits were combined to allow the implementation of a quantum teleportation protocol. This was the first demonstration of a completely deterministic teleportation protocol with massive particles. In particular, it was possible to use the outcome of a complete Bell-measurement to reconstruct the input state, a step which was omitted in all previous experimental realizations of teleportation.

Zusammenfassung

Quanteninformationverarbeitung wurde im Laufe der vergangenen Jahre intensiv diskutiert. Verschränkung ist dabei ein wesentlicher Bestandteil, der gewisse Quantenalgorithmen gegenüber den entsprechenden klassischen Algorithmen exponentiell beschleunigen kann. Ein System, das sich für Quanteninformationverarbeitung besonders eignet, sind in einer linearen Paulfalle gespeicherte Ketten von Ionen. In der vorliegenden Arbeit werden verschränkte Zustände von zwei und drei Ionen erzeugt und gezielt manipuliert.

Die wesentlichen Werkzeuge für einen Ionenfallen-Quantencomputer, speziell ein controlled-NOT Quantengatter zwischen zwei Ionen, werden demonstriert. Die verschränkten Zustände können mit solcher Genauigkeit kontrolliert werden, dass es möglich war deterministische Quantenzustands-Teleportation zwischen Ionen durchzuführen. Die beschriebenen Experimente wurden mit in einer linearen Paul-Falle gespeicherten Ketten von $^{40}\text{Ca}^+$-Ionen durchgeführt. Die Quantenbits werden dabei durch den $S_{1/2}$-Grundzustand und den metastabilen $D_{5/2}$-Zustand der Ca^+-Ionen dargestellt. Die notwendigen Operationen für die Verschränkung von Ionen-Quantenbits werden durch eine Abfolge von Laserpulsen bei 729 nm umgesetzt, die den Quadrupolübergang zwischen dem $S_{1/2}$ und $D_{5/2}$-Zustand anregen.

Mit diesem experimentellen Aufbau wurden zwei Ionen in allen vier Bellzuständen präpariert. Mit drei Ionen wurden beide existierende Klassen von verschränkten Dreiteilchenzuständen, GHZ- und W-Zustände, erzeugt. Die verschränkten Zustände wurden mittels Quantenzustandstomografie untersucht, die die vollständige Information über das Quantensystem in Form von dessen Dichtematrix liefert. Zusätzlich wurde die Lebensdauern der verschränkten Zustände untersucht. Wie theoretisch erwartet, erweisen sich bestimmte Zustände als besonders robust gegenüber der dominierenden Fehlerquelle in unseren Experimenten, korreliertes Phasenrauschen aufgrund von Laserfrequenz-Fluktuationen, herausgestellt.

Eine Methode um ein einzelnes Ionen-Quantenbit zu messen ohne die anderen Quantenbits innerhalb der Ionenkette zu stören wurde verwirklicht. Die Auswirkung einer solchen Messung auf GHZ- und W-Zustände wurde untersucht. Zusätzlich wurde der experimentelle Aufbau erweitert, so dass Operationen auf einzelnen Quantenbits ausgeführt werden können, die vom Ergebnis einer unmittelbar vorher stattgefundenen Messung eines oder zweier Quantenbits abhängen. Mit Hilfe dieser Technik wurde ein GHZ-Zustand nur mittels lokaler Operationen in einen reinen zweiteilchenverschränkten Zustand überführt.

Abschliessend, wurden die entwickelten Techniken zur Manipulation von Verschränkung von Ionen-Quantenbits kombiniert angewendet, um ein vollständig deterministisches Teleportationsprotokoll mit massiven Teilchen zu realisieren. Vor allem gelang es eine vollständige Bellmessung auszuführen und das Ergebnis dieser Messung unmittelbar zur Rekonstruktion des Eingangszustands zu verwenden, ein Schritt der bei den bisherigen experimentellen Umsetzungen von Teleportation ausgelassen wurde.

iv

Contents

Contents

Contents

viii

1. Introduction

Entanglement is possibly one of the most peculiar aspects of quantum mechanics. In an entangled composite quantum system the individual subsystems are strongly linked to each other even if they are far apart and no longer interact with each other. The whole composite quantum system can be well described as a definite pure state, while for the state of its subsystems such a description is not possible[1]. A measurement on one of the subsystems will affect the outcome of measurements performed in the other subsystems, a feature which obviously contradicts local-realism, i.e. that the quantum states of spatially separated non-interacting particles are independent. This phenomenon was first discussed by Einstein, Podolsky and Rosen in their seminal paper in 1935 [1] in which they investigated the results of incompatible measurements on one part of a two-particle system, which interacted once but are spatially separated at the time of the measurement[2]. The contradiction arising in Einstein et al.'s argument, which let them question the completeness of quantum mechanics, was rooted in their insistence on local-realism.

In the 1960s John S. Bell discussed the EPR argument and was able to show that the correlations between the results of measurements on the subsystems of an entangled state predicted by quantum mechanics go beyond what can be explained by any theory assuming local-realism [3–5]. The inequalities derived by Bell and others [4, 6, 7] allowed for an experimental test of quantum mechanics. Such experiments were carried out with entangled photons confirming the predictions of quantum mechanics [8, 9].

In this context entanglement appears only as a source for paradoxes and counterintuitive phenomena, which challenge our understanding of reality and quantum mechanics in particular. However, in the last two decades quantum mechanical systems have been discussed as means to store and process information. In this context entanglement is not a peculiarity but a useful or even indispensable tool.

In quantum information theory the smallest unit is usually a two-level quantum system, where the levels are denoted as $|0\rangle$ and $|1\rangle$. For such a system due to its obvious resemblance to a bit of classical information the notion *qubit* was coined [10]. Qubits offer a special feature in contrast to classical bits, since they can be prepared in a superposition of their logical basis states $|0\rangle$ and $|1\rangle$. Thus, qubits offer new possibilities for information processing. At the same time, however, quantum mechanics imposes restrictions on what we can do with them. For instance it is not possible to determine the state of a single qubit in a superposition $(a|0\rangle + b|1\rangle)$ without disturbing the qubit. A measurement in the logical basis will inevitably project the state into $|0\rangle$ or $|1\rangle$ revealing little or no information about the parameters a and b.

---

[1]More precisely, this means that the state of the composite system cannot be decomposed in a product of pure states of its subsystems.

[2]The authors did not use the term *entanglement* in Ref. [1]. It seems that Schrödinger, in a reply to EPR published in [2], used this term for the first time.

1. Introduction

Suppose one unknown qubit of quantum information is to be transferred from one party, whom we call Alice, to another called Bob. Suppose Alice and Bob have no means to directly exchange a quantum system carrying the information, i.e. no *quantum channel* is available to them. Alice could try to measure the qubit in order to obtain classical information, which she would convey to Bob via a classical channel, who would then try to reconstruct the original state based on this information. But such an attempt would be in vain, since such a measurement doesn't reveal much useful information about the quantum state. What can Alice and Bob do? This is the point where entanglement as a useful resource comes into play. Bennett et al. devised a recipe they called *teleportation* which allows Alice and Bob to perfectly transfer a quantum state provided that they both share one half of an entangled pair of particles[3] [12]. All Alice has to do is to measure the unknown qubit and her part of the entangled pair in a certain basis and convey the outcome of her measurement, i.e. two bits of classical information, to Bob. Thereupon Bob has the necessary knowledge to reconstruct the original state in his part of the entangled pair. The information-transfer in teleportation seems to happen almost miraculously, letting a quantum state disappear at one place and appear at a totally different place, and indeed to precisely imagine or explain what happens leads to the same interpretational difficulties as with the EPR-Paradoxon (c.f. Wootters in [13]). Nevertheless, teleportation has been demonstrated with entangled photons [14, 15] and in a few other physical systems [16, 17].

Another field in which entanglement plays a vital role is quantum computation, i.e. the processing of quantum information stored in a register of qubits. The idea that a computer exploiting the laws of quantum mechanics can potentially solve problems which are intractable with a classical computer was first pointed out by Feynman in 1982. He noted that a simulation of the dynamics of a quantum system on a classical computer requires an exponentially growing computational effort with the size of the quantum system . However, a suitable well-controlled quantum system could be used to mimic and therefore simulate the dynamics of the investigated quantum system [18, 19]. In 1985 David Deutsch defined a quantum Turing machine [20], i.e. the quantum mechanical analogue to the Turing machine, which is a fundamental computational model in classical computation (c.f. Nielsen and Chuang [21]). He later formulated another computational model for the quantum computer, namely the *quantum circuit model* in which an arbitrary computation is carried out by applying a finite set of unitary operations or *quantum gates* on a register of qubits [22].

The discussion about quantum computers wouldn't be much more than of academic interest, if there weren't tasks which a quantum computer could perform which are less efficiently solved or even intractable by a classical computer. Apart from the previously mentioned possibility to simulate the dynamics of quantum systems, a collection of algorithms for a quantum computer were discovered which would solve their respective problems much faster than their classical counterparts. The first quantum algorithm was found by D. Deutsch and is nowadays known as the *Deutsch-Jozsa algorithm*, which can decide whether a given boolean function is constant or balanced in a single evaluation of the function, while a classical computer would need at least two evaluations [20, 23]. Another kind of quantum algorithm is a *quantum search algorithm*,

---

[3]This entangled pair of spin-1/2 particles or qubits is usually denoted as an EPR-pair alluding to Einstein, Podolsky and Rosen's paper [1]. However, the well known version of the EPR-paradox using spin-1/2 particles was formulated much later by Bohm [11].

2

which can search for a particular entry in a database. The most prominent one of these is the algorithm formulated by L. Grover [24, 25]. The most spectacular quantum algorithm is certainly the *Shor algorithm*, which was found by Peter Shor in 1994 [26]. The Shor algorithm allows one to find the prime factors of a number N in a time which only grows polynomially with N. This problem is seen as inefficient on a classical computer, i.e. the necessary time for finding the prime factors grows exponentially with N. Shor's discovery drew a lot of attention to the field of quantum computation, since the security of common cryptographic protocols like the RSA cryptosystem relies on the inability of classical computers to factorize large numbers [27].

Given the fact that quantum computers can solve certain problems exponentially faster than their classical counterparts it is tempting to ask which exact feature of a quantum computer gives rise to this speed-up? This question was extensively discussed by Jozsa, Ekert and others in [28–32]. At first glance, the ability to prepare a register of N qubits in a superposition of all 2^N possible combinations and perform a computation on all these possibilities at once in a kind of parallel computation might be identified as the distinctive feature of a quantum computer. But Jozsa showed that superpositions alone are not the unique feature of a quantum computer, since superpositions of logical states could be mimicked by classical waves. However, in general, the register of qubits will become entangled in course of the computation, which can't be simulated by classical waves without exponentially growing resources [28]. It turns out that entanglement is the essential non-classical feature in a quantum computer, providing the exponential speed-up in quantum algorithms like the Shor algorithm [29].

Entanglement can also improve the performance of a quantum computer in another respect. Error correction is an important technique when it comes to realize a working quantum computer, because in reality qubits will be subjected to various kinds of noise changing the state of the qubits. Peter Shor devised in 1995 a quantum-error correction scheme in which phase and bit-flip errors can be detected and corrected [33]. The basic idea in this scheme is use two additional *ancilla qubits* to encode the state of a qubit $|\Psi\rangle = (a|0\rangle + b|1\rangle)$ as $a|000\rangle + b|111\rangle$, i.e. the quantum information of one qubit is encoded in an entangled state of three qubits. An error inflicted upon one of the qubits can be detected by applying the inverse encoding procedure and measuring the state of the ancilla bits. The outcome of the measurement, also called the *syndrome*, reveals if an error occcured.

In order to implement a quantum computer a physical system has to meet several requirements. Such a list of requirements was given by DiVincenzo [34]:

1. A scalable physical system with well characterized qubits

2. The ability to initialize the state of the qubits to a simple well-defined state, such as $|000...\rangle$

3. Long relevant decoherence times, much longer than the gate operation time

4. A universal set of quantum gates

5. A qubit specific measurement capability

Meeting these requirements is a demanding task. Various physical systems were proposed for implementing a quantum computer, including:

- Optical photon quantum computer [35]

- Optical cavity quantum electrodynamics [36]

- Ion traps [37, 38]

- Nuclear magnetic resonance (NMR) [39, 40]

- Josephson junctions [41–43]

- Quantum dots [44]

- Silicon-based nuclear spin quantum computer [45]

This list and the references therein are by no means exhaustive. The most complex quantum algorithms have been so far realized with NMR quantum computing [46]. However, NMR quantum computing lacks scalability and is often criticized for working with highly mixed, separable states [47–50]. The latter three proposals are solid-state systems which are tempting given the success of solid-state devices in today's technology. However, the experimental progress in realizing these proposals has so far been limited, although recently basic operations were demonstrated [51–56].

Ion traps have served as a tool for investigating systems of a few or even single ions with laser spectroscopic techniques since the late 1970s. Trapped ions represent a suitable system for quantum computing, since quantum information can be encoded in qubits made up of the ground state $|g\rangle$ and and a metastable excited state $|e\rangle$ of the ions. Single qubits can be manipulated by addressing them with suitable laser pulses. Interactions between the internal states of different ions necessary for two-qubit quantum gates can be mediated using one of the vibrational modes common to all ions. Such a two-qubit gate was first proposed by I. Cirac and P. Zoller in 1995 [37] and was followed by several other proposals also utilizing the interaction mediated by a common vibrational mode [57, 58].

In recent years considerable progress has been made in implementing an ion trap quantum computer. In the group of D.J. Wineland at NIST in Boulder the basic steps for implementing the Cirac-Zoller quantum gate had already been realized in 1995 [59]. In the following years they were able to prepare entangled states of, first two [60], and later four, ions [61]. A two-qubit quantum gate was demonstrated employing a spin-dependent optical dipole force in 2003 [62]. Recently they demonstrated the preparation of GHZ-states, quantum teleportation and error correction.

In our experimental setup the basic techniques of laser cooling and manipulation of single qubits were demonstrated [63–65]. This allowed us to implement the Deutsch-Jozsa algorithm with a single ion, the first demonstration of a quantum algorithm outside of NMR quantum computing [66]. The Cirac-Zoller quantum gate was implemented for two ions [67], such that we have a complete set of operations at hand necessary for quantum computing.

As was pointed out, entangled states are a crucial ingredient for quantum computing. Quantum algorithms will in general entangle the register of qubits. The lifetime and stability against noise of these states will substantially determine the performance of our quantum computer. Therefore, the aim of this thesis is to investigate our ability to prepare and manipulate entangled states of trapped ions. This thesis is structured as follows: In Chapter 2 qubits and the

operations acting upon them are outlined. Furthermore means to identify and quantify entangled states are introduced. In Chapter 3 the dynamics of ions in linear Paul traps is briefly reviewed. Chapter 4 describes the interaction of laser light with the trapped ions. The internal electronic energy levels and transitions of $^{40}Ca^+$ we excite in our experiments are shown. The quadrupole transition connecting the states which make up our qubit is investigated in detail. Finally, it is shown how the previously introduced laser-ion interaction serves to implement the single-qubit operations outlined in Chapter 2. The experimental setup is explained in Chapter 5. Basic experimental techniques which are required for more complex experiments are described in Chapter 6. The following Chapters 7 - 10 present the experimental results achieved in this thesis. Chapter 7 describes the preparation of Bell-states of two trapped ions. The lifetime of the different prepared Bell-states is investigated. In Chapter 8 the realization of the Cirac-Zoller controlled-NOT quantum gate with two ions is presented. Initial results of these measurements were already presented in the thesis of Stephan Gulde [68]. Here a complete analysis of the CNOT gate is given. In Chapter 9 the results concerning entangled states of three ions are presented. Both possible classes of tripartite entangled states were generated and their lifetime was investigated. Important experiments like teleportation and quantum-error-correction involve the measurement of a part of the qubit register and subsequent operations conditioned by the outcome of this measurement. Therefore, the effect of a measurement on the different entangled states of three ions was investigated. By implementing a subsequent conditional operation a tripartite entangled state was tranferred into a pure bipartite entangled state. Finally the highlight of this thesis is presented in Chapter 10. The experimental techniques developed for handling entangled states allowed us to perform a textbook-style implementation of quantum teleportation. For the first time a teleportation experiment was carried out in which the necessary entangled pair was generated on demand and the outcome of a complete Bell-measurement was used to reconstruct the original quantum state.

1. Introduction

6

2. Quantum bits

2.1. Single qubits

The quantum state of a two level system, consisting of the levels $|0\rangle$ and $|1\rangle$, can be written as:

$$|\psi\rangle = a\,|0\rangle + b\,|1\rangle\,. \tag{2.1}$$

Here a and b are complex numbers, which satisfy the normality condition $|a|^2 + |b|^2 = 1$. Such a system is capable of storing binary information in analogy with a classical bit with logical states 0 and 1, which has led to the notion of *quantum bits* or *qubits*.

Operations mapping a quantum state $|\Psi\rangle = a|0\rangle + b|1\rangle$ onto another quantum state $|\Psi'\rangle = a'|0\rangle + b'|1\rangle$ are unitary transformations and preserve the norm. They can be expressed as unitary 2×2 matrices acting on a quantum state vector $|\Psi\rangle$, which reads:

$$|\psi\rangle = \begin{pmatrix} a \\ b \end{pmatrix}. \tag{2.2}$$

An example of such an operation is the *Hadamard* operation:

$$H = \frac{1}{\sqrt{2}} \begin{pmatrix} 1 & 1 \\ 1 & -1 \end{pmatrix}, \tag{2.3}$$

which transfers the state $|0\rangle$ or $|1\rangle$ into an equal superposition $(|0\rangle \pm |1\rangle)/\sqrt{2}$.

A useful way to visualize the state of a two level system is to represent it as a point with polar coordinates θ and φ on a unit sphere, as shown in Fig. 2.1. This picture is generally known as the *Bloch sphere representation* and the vector $\vec{\lambda} = (\cos\varphi\sin\theta, \sin\varphi\sin\theta, \cos\theta)$ as the Bloch vector. In this picture, Eq. 2.1 can be expressed as:

$$|\psi\rangle = e^{i\gamma}\left[\cos\left(\frac{\theta}{2}\right)|0\rangle + e^{i\varphi}\sin\left(\frac{\theta}{2}\right)|1\rangle\right] \tag{2.4}$$

Here the global phase factor $e^{i\gamma}$ has no observable effect and is therefore usually omitted. Unitary operations act in the Bloch sphere representation as rotations of the Bloch vector.
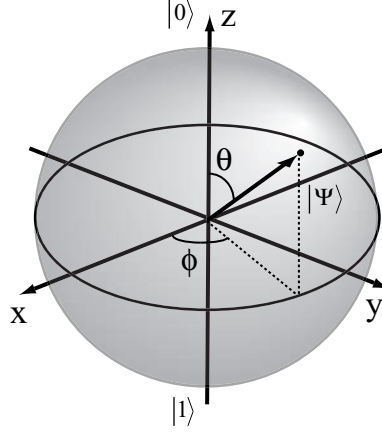
Figure 2.1.: Bloch sphere representation of a two level system.

Thereby, rotations about the x-, y- and z- axes are given respectively by[1] :

$$R_x(\theta) = e^{-i\frac{\theta}{2}X} = \cos\frac{\theta}{2}I - i\sin\frac{\theta}{2}X = \begin{pmatrix} \cos\frac{\theta}{2} & -i\sin\frac{\theta}{2} \\ -i\sin\frac{\theta}{2} & \cos\frac{\theta}{2} \end{pmatrix}$$

$$R_y(\theta) = e^{-i\frac{\theta}{2}Y} = \cos\frac{\theta}{2}I - i\sin\frac{\theta}{2}Y = \begin{pmatrix} \cos\frac{\theta}{2} & -\sin\frac{\theta}{2} \\ \sin\frac{\theta}{2} & \cos\frac{\theta}{2} \end{pmatrix}$$

$$R_z(\theta) = e^{-i\frac{\theta}{2}Z} = \cos\frac{\theta}{2}I - i\sin\frac{\theta}{2}Z = \begin{pmatrix} e^{-i\frac{\theta}{2}} & 0 \\ 0 & e^{i\frac{\theta}{2}} \end{pmatrix}, \tag{2.5}$$

where X,Y and Z are the Pauli matrices and I the identity matrix. These matrices are defined by:

$$X = \begin{pmatrix} 0 & 1 \\ 1 & 0 \end{pmatrix} \qquad\qquad Y = \begin{pmatrix} 0 & -i \\ i & 0 \end{pmatrix}$$

$$Z = \begin{pmatrix} 1 & 0 \\ 0 & -1 \end{pmatrix} \qquad\qquad I = \begin{pmatrix} 1 & 0 \\ 0 & 1 \end{pmatrix}. \tag{2.6}$$

More generally, the rotation of the Bloch vector by θ around a real unit vector $\vec{n} = (n_x, n_y, n_z)$ is given by:

$$R_{\vec{n}} = \exp(-i\theta\vec{n} \cdot \vec{\sigma}/2) = \cos\left(\frac{\theta}{2}\right)I - i\sin\left(\frac{\theta}{2}\right)(n_xX + n_yY + n_zZ), \tag{2.7}$$

where $\vec{\sigma}$ denotes the three-component vector (X, Y, Z) of Pauli matrices.

---

[1] Rotation around an axis in the Bloch sphere picture can be imagined as looking along the respective axis in the positive direction and turning the Bloch vector clockwise.

2.2. Multiple qubits

For a system of N qubits a suitable set of basis states is given by the 2^N-product states of the individual qubit states $\{|0\rangle, |1\rangle\}$:

$$|n\rangle = |i_N\rangle \otimes |i_{N-1}\rangle \otimes ... \otimes |i_1\rangle, \tag{2.8}$$

where $i_k \epsilon \{0, 1\}$ and $n = \sum_{k=1}^{N} i_k \cdot 2^{k-1}$. Please note that the rightmost state in this tensor product belongs to the first qubit, which might be counterintuitive in the first place. Every N qubit quantum state can be expressed as a decomposition of these *computational basis states*. For example in the case of two qubits we have:

$$|\psi\rangle = a_0 |00\rangle + a_1 |01\rangle + a_2 |10\rangle + a_3 |11\rangle, \tag{2.9}$$

where the coefficients a_k obey the normality condition $\sum_{i=0}^{N-1} |a_k|^2 = 1$. Quantum operations acting on a system of N qubits are described by unitary $N \times N$ matrices. For two qubits for example the operation $I \otimes X$, i.e performing the identity operation on the second qubit and X on the first, is described by:

$$I \otimes X = \begin{pmatrix} 0 & 1 & 0 & 0 \\ 1 & 0 & 0 & 0 \\ 0 & 0 & 0 & 1 \\ 0 & 0 & 1 & 0 \end{pmatrix}, \tag{2.10}$$

where the matrix is notated with respect to the basis order $\{|00\rangle, |01\rangle, |10\rangle, |11\rangle\}$. This matrix notation will be used throughout this thesis.

2.3. Controlled quantum gates

Operations where the state of one qubit is changed depending on the state of another qubit are called *controlled operations*. An important example for a controlled operation is the *controlled-NOT* or CNOT operation:

$$U_{\mathrm{CNOT}}^{21} = \begin{pmatrix} 1 & 0 & 0 & 0 \\ 0 & 1 & 0 & 0 \\ 0 & 0 & 0 & 1 \\ 0 & 0 & 1 & 0 \end{pmatrix}. \tag{2.11}$$

This operation flips the state of the first qubit (the *target* qubit) if the second qubit (the *control* qubit) is in state $|1\rangle$ and leaves the target qubit unchanged if it's in state $|0\rangle$. We adopt the notation $U_{\mathrm{CNOT}}^{\mathrm{control,target}}$ in order to denote which qubit acts as control and which as target qubit. Another controlled two qubit operation is the controlled Z or *phase* gate:

$$\Phi = \begin{pmatrix} 1 & 0 & 0 & 0 \\ 0 & 1 & 0 & 0 \\ 0 & 0 & 1 & 0 \\ 0 & 0 & 0 & -1 \end{pmatrix}. \tag{2.12}$$

In the case of the phase gate the role of control and target qubit are interchangeable. Phase gate and controlled NOT operations are closely related, since the controlled NOT gate can be decomposed into two Hadamard operation and a phase gate:

$$U_{\text{CNOT}}^{21} = H_1 \cdot \Phi \cdot H_1, \tag{2.13}$$

where $H_1 = I \otimes H$ is the Hadamard operation acting on the first qubit:

$$H_1 = \frac{1}{\sqrt{2}} \begin{pmatrix} 1 & 1 & 0 & 0 \\ 1 & -1 & 0 & 0 \\ 0 & 0 & 1 & 1 \\ 0 & 0 & 1 & -1 \end{pmatrix}. \tag{2.14}$$

The qubit to which the Hadamard operations are applied acts as the target qubit.

Controlled operations are of vital importance for quantum computing. It has been shown, that the controlled NOT operation and single qubit rotations are *universal* [69], i.e an arbitrary unitary operation can be realized by a combination of controlled NOT and single qubit operations.

2.4. Measurements

2.4.1. Projective measurements

The ability to read out a register of qubits by measurements is a key ingredient for quantum computing. The type of measurement usually encountered in experiments are *projective measurements*, where the measurement of an observable M causes the quantum system subjected to the measurement to be projected onto one of the eigenstates of the operator $\hat{M}$. The Hermitian operator $\hat{M}$ can be expressed as:

$$\hat{M} = \sum_m m P_m \tag{2.15}$$

where P_m is the projector onto the eigenspace of $\hat{M}$ with eigenvalue m. The probability that the outcome m occurs is given by:

$$p(m) = \langle \psi | P_m | \psi \rangle \tag{2.16}$$

and the state of the quantum system is projected onto the state:

$$\left| \psi' \right\rangle = \frac{P_m \left| \psi \right\rangle}{\sqrt{p(m)}}. \tag{2.17}$$

2.4.2. Measurement in the Bell basis

A special case of a measurement is a projective measurement in the Bell state basis. This basis is given by the four Bell states, which are expressed in the computational basis as:

$$
\begin{aligned}
\Psi_+ &= \tfrac{1}{\sqrt{2}}\left(|10\rangle + |01\rangle\right) \\
\Psi_- &= \tfrac{1}{\sqrt{2}}\left(|10\rangle - |01\rangle\right) \\
\Phi_+ &= \tfrac{1}{\sqrt{2}}\left(|00\rangle + |11\rangle\right) \\
\Phi_- &= \tfrac{1}{\sqrt{2}}\left(|00\rangle - |11\rangle\right).
\end{aligned}
\tag{2.18}
$$

In most experimental setups measurements are preferably done in the computational basis $\{|0\rangle, |1\rangle\}$. Therefore, in order to perform a measurement in the Bell basis, the Basis states $\{\Phi_+, \Phi_-, \Psi_+, \Psi_-\}$ must be mapped onto the computational basis states of two qubits $\{|00\rangle, |01\rangle, |10\rangle, |11\rangle\}$.

This is achieved by first applying a controlled NOT U_{CNOT}^{12}, where qubit 1 is the control qubit and qubit 2 the target qubit, and then a Hadamard operation H_1 to qubit 1. As an example, consider the action of these operations on the Bell state Ψ_+:

$$
\frac{1}{\sqrt{2}}\left(|10\rangle + |01\rangle\right) \xrightarrow{U_{\mathrm{CNOT}}^{12}} \frac{1}{\sqrt{2}}(|10\rangle + |11\rangle) = \frac{1}{\sqrt{2}}|1\rangle(|0\rangle + |1\rangle) \xrightarrow{H_1} |10\rangle.
\tag{2.19}
$$

Interestingly, this procedure works in both directions, i.e starting from the computational basis states, applying a Hadamard operation first and then the CNOT gate, will generate Bell states.

2.5. Sequences of quantum operations: Quantum circuits

In the previous sections the most fundamental operations, which can be applied to one qubit or a register of multiple qubits were introduced. In general an algorithm running on a quantum computer will comprise many of these operations. Such a sequence of operations is also called a *quantum circuit*, an analogy to classical computing, where a computation is built up of a network of different logic gates[2]. In the following, different ways of expressing quantum algorithms are shown and the corresponding conventions and notations introduced, which will be used throughout this thesis.

First of all, when using the bra- and ket-notation for quantum states, the qubits will be ordered as:

$$
|\mathrm{qubit}_n, ..., \mathrm{qubit}_2, \mathrm{qubit}_1\rangle.
$$

Outer products of operators will be ordered in the same way, such that for example in $I \otimes I \otimes X$ denotes an X-operation on qubit 1 and the identity operation on qubits 2 and 3. Subsequent unitary operations on a register of qubits can be expressed by the product of the corresponding operators, giving the overall unitary operation $U = ...Op_3 \cdot Op_2 \cdot Op_1 \cdot |\Psi_{in}\rangle$.

---

[2]In fact quantum circuits are a *computational model*, i.e. a generic model, how a computation is done. It is not the only way a computer can work. Other models would be the one-way quantum computer or the more abstract quantum Turing machine [70, 71]
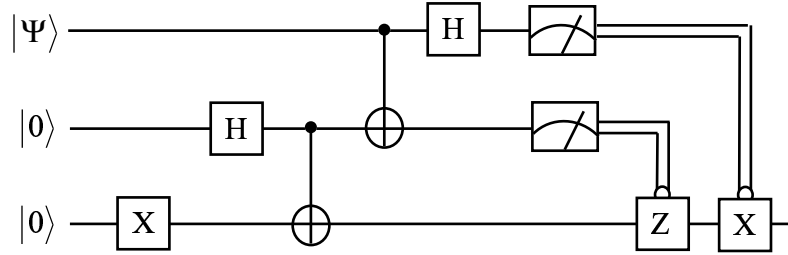
Figure 2.2.: Graphical representation of a quantum circuit. The circuit shown is implementing quantum teleportation. The temporal order is from left to right. Each horizontal lines represent the state of one qubit. Operations acting upon the qubits are indicated by different symbols, which are explained in Fig. 2.3.

Another way of representing a quantum circuit is shown in Fig. 2.2. This graphical representation of a register of qubits and the operations acting upon them should be read as follows: Each horizontal line represents the state of one qubit. The operations acting upon the qubits are represented by different symbols, which are explained in Fig. 2.3. Time is increasing, when the circuit is read from left to right.

In Sec. 4.5 this notation will be adapted to the ion trap quantum computer by replacing the abstract operators by the corresponding laser pulses.

2.6. Quantum state tomography

The state of a quantum system is completely described by its density matrix ρ. Quantum state tomography is a procedure to determine the density matrix of quantum system, provided that this system is available in many copies. This procedure relies on the fact that every density matrix ρ of a n-qubit system can be expanded into a series of mutually orthogonal operators O_i [3], such that ρ can be written as:

$$\rho = \sum_{i=1}^{4^n} \lambda_i O_i. \tag{2.20}$$

The coefficients λ_i can be obtained by measuring the expectation value of their corresponding operator O_i:

$$\lambda_i = tr(\rho \cdot O_i) \tag{2.21}$$

Therefore, the density matrix ρ of a given state can be reconstructed by measuring the expectation values of the operators O_i. The actual set of operators used in our experiments is given in Appendix A.1.

---

[3]Mutually orthogonal means that the operators O_i obey the equation $tr(O_i O_j) = 2^n \delta_{ij}$
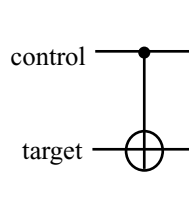
Pauli operators:

$$-\boxed{X}- \;=\; \begin{pmatrix} 0 & 1 \\ 1 & 0 \end{pmatrix} \qquad -\boxed{Y}- \;=\; \begin{pmatrix} 0 & -i \\ i & 0 \end{pmatrix} \qquad -\boxed{Z}- \;=\; \begin{pmatrix} 1 & 0 \\ 0 & -1 \end{pmatrix}$$

Hadamard operation:
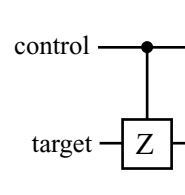
$$-\boxed{H}- \;=\; \frac{1}{\sqrt{2}} \begin{pmatrix} 1 & 1 \\ 1 & -1 \end{pmatrix}$$

Controlled NOT:

Controlled Z/ Phase gate:

$$= \begin{pmatrix} 1 & 0 & 0 & 0 \\ 0 & 1 & 0 & 0 \\ 0 & 0 & 0 & 1 \\ 0 & 0 & 1 & 0 \end{pmatrix} \qquad\qquad = \begin{pmatrix} 1 & 0 & 0 & 0 \\ 0 & 1 & 0 & 0 \\ 0 & 0 & 1 & 0 \\ 0 & 0 & 0 & -1 \end{pmatrix}$$

Measurement:
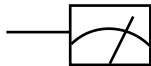
Classical controlled Z:
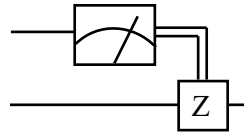
Figure 2.3.: Symbols of quantum operations and the corresponding unitary matrices.

2.7. Entanglement

2.7.1. Entangled states of two qubits

A definition of entanglement of a quantum system containing multiple subsystems is usually associated with the question whether its quantum state can be decomposed into a product of its subsystems states.

This approach can be illustrated by considering a bipartite system consisting of two qubits in a pure state. A state Ψ of this bipartite system is called a *product state* or *separable*, if it can be written as a product of its subsystems states:

$$\Psi = \psi_1 \otimes \psi_2 \tag{2.22}$$

In this situation both subsystems are completely independent of each other. A measurement performed on the one subsystem will not affect the state of the other. Measurement results on both subsystems will be uncorrelated.

In contrast to this, a state which cannot be written as a product of subsystem states is called an *entangled state*. A prominent example of entangled states are the Bell states given in Eq. 2.18.

Here the subsystems are no longer independent. A measurement performed on the one subsystem will result in a state reduction in both subsystems with strongly correlated measurement results.

For mixed states this definition can be expanded as follows: A state, described by the density matrix ρ, is said to be separable if a decomposition into product states exist:

$$\rho = \sum_i p_i \cdot \rho_1 \otimes \rho_2; \quad p_i > 0 \,, \sum_i p_i = 1 \tag{2.23}$$

The nonexistence of such a decomposition identifies an entangled mixed state. In addition to quantum correlations, mixed states can also contain classical correlations, which are characterized by the propabilities p_i.

Unfortunately, for a given density matrix ρ it is not easy to directly verify whether a decomposition like that in Eq. 2.24 exists or not. However, for bipartite systems, a criterion exists to determine whether a state is separable or not, which relies on the behavior of the partial transpose ρ^{PT}. The partial transpose ρ^{PT} is defined by:

$$\rho^{PT} = (\sigma_x \otimes I) \cdot \rho \tag{2.24}$$

It has been shown that a mixed state ρ is entangled if and only if its partial transpose ρ^{PT} has a negative eigenvalue [72].

2.7.2. Quantifying entanglement

A quantitative discussion of entanglement is possible by defining *entanglement measures*. It is reasonable to start the discussion of entanglement measures by considering pure states of a bipartite quantum system. Using the Schmidt decomposition [71] any pure state $\Psi(A, B)$ can be written as:

$$\Psi(A, B) = \sum_{i=1}^{n} c_i |\alpha_i\rangle \otimes |\beta_i\rangle, \tag{2.25}$$

where $\{\alpha_i\}$ and $\{\beta_i\}$ are a orthonormal basis of the subsystems A and B, respectively, and the coefficients c_i are positive, real numbers. An entanglement measure for such a state is given by the entropy of one of the subsystems:

$$E(\Psi) = S(\text{Tr}_A |\Psi\rangle\langle\Psi|) = S(\text{Tr}_B |\Psi\rangle\langle\Psi|) = -\sum_{i=1}^{n} c_i^2 \log_2 c_i^2, \tag{2.26}$$

where $S(\rho) = -\text{Tr}(\rho \log \rho)$ is the *von Neumann entropy*. The definition of the quantity $E(\Psi)$ is connected to the question how many singlet pairs of the type $|\Psi_-\rangle = |0\rangle_A|1\rangle_B - |1\rangle_A|0\rangle_B$ are necessary to create n copies of a given bipartite state $\Phi(A,B)$. It has been shown that approximately $nE(\Phi)$ singlet states are necessary to perform this task [73].

For mixed states of bipartite systems a definition of an entanglement measure becomes more difficult. The von Neumann entropy of one of the subsystems $E(\rho)$ is no longer a good measure for entanglement, since it can be nonzero even if the state is separable. Again the definition of an entanglement measure can be connected to the question of how many single pairs Ψ_- are necessary to generate n copies of a mixed state ρ. Every mixed state ρ can be written as a decomposition into pure states:

$$\rho = \sum_{i=1}^{N} p_i |\Phi_i\rangle\langle\Phi_i|, \quad \text{with } \sum_{i=1}^{N} p_i = 1, \tag{2.27}$$

where the states $\{|\Phi_i\rangle\}$ are normalized states of the bipartite system. Considering the result obtained for pure states, it is reasonable to estimate the number of singlets necessary to create n copies of ρ as:

$$n \cdot \sum_{i=1}^{N} p_i E(\Phi_i). \tag{2.28}$$

However the quantity $\sum p_i E(\Phi_i)$ is still not a good measure of entanglement, since it depends on the particular decomposition of ρ. This line of reasoning leads to the definition of *entanglement of formation*:

$$E_f(\rho) = \inf \sum_j p_j E(\Phi_j). \tag{2.29}$$

Here the infimum of $\sum p_i E(\Phi_i)$ over all possible decompositions of ρ into pure states is taken as an entanglement measure. The definition of entanglement of formation given in Eq. 2.30 involves an optimization problem to find the infimum, which in case of higher dimensional systems is an unsolved problem. However for bipartite systems an algebraic solution is known, which allows calculation of the entanglement of formation from the given density matrix [74, 75].

2. Quantum bits

3. Linear Paul traps

3.1. Linear Paul traps

Radiofrequency traps were originally invented by Wolfgang Paul in the 1950s as mass filters and later on were used as traps for charged particles. A linear Paul trap has an electrode configuration as can be seen in Fig. 3.1. Four rod shaped electrodes generate a potential for confinement in the x-y plane, while the endcap electrodes generate a confining axial potential.

Suppose a radiofrequency voltage $V = V_0 \cdot \cos(\Omega t)$ is applied to two of the rods, which lie diagonally opposite each other, while the other pair of electrodes is held at ground potential. If the electrodes are assumed to have hyberbolical shape, the time varying quadrupole potential Φ in the x-y or radial plane is given by

$$\Phi(x, y, t) = \frac{x^2 - y^2}{2r_0^2} \cdot V_0 \cos(\Omega t), \qquad (3.1)$$

where r_0 is the minimum distance from the trap center to the electrodes. In practice the trap electrodes are usually shaped like rods or blades to improve the optical access to the trap center. In this case the quadrupole potential above is only valid for small excursions around the trap axis. For larger excursions higher order corrections of the potential have to be taken into account to describe the motion of a charged particle properly.

Using the potential given in Eq. 3.1 the equations of motion for a charged particle with mass M and charge e in the radial plane are:

$$\frac{d^2x}{dt^2} - 2q\frac{\Omega^2}{4}\cos(\Omega t)x = 0$$
$$\frac{d^2y}{dt^2} + 2q\frac{\Omega^2}{4}\cos(\Omega t)y = 0,$$
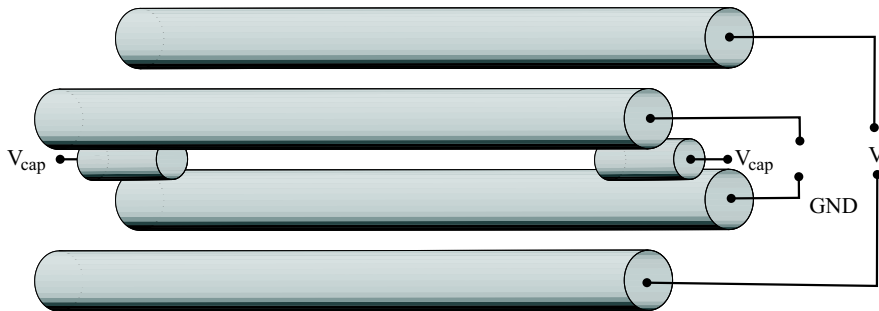

Figure 3.1.: Schematic drawing of linear Paul trap. Instead of of the ideal hyperbolic surfaces a more realistic design using rod shaped electrodes is shown.

where q is defined as:

$$q = \frac{2eV}{Mr_0^2\Omega^2}. \tag{3.2}$$

These equations take the form of the *Mathieu equations*. Stable solutions can be found for $0 < q < 0.908$ [76]. An analysis of the solutions shows that the motion can be separated into a slow *secular motion* around the trap center and a fast oscillation driven by the trap radiofrequency called *micromotion*. The secular motion of a charged particle is a harmonic motion with a frequency:

$$\omega_{r0} = \omega_x = \omega_y = \frac{\Omega q}{2\sqrt{2}}, \tag{3.3}$$

where the oscillation frequencies in x and y direction are assumed to be degenerate.

For complete confinement in all three dimensions an additional trapping potential along the axial z-direction is necessary. This is achieved by applying a DC voltage V_{cap} to the endcap electrodes. The equations of motion including the axial potential are then given by:

$$\frac{d^2x}{dt^2} + \frac{\Omega^2}{4}(b - 2q\cos(\Omega t)x) = 0$$
$$\frac{d^2y}{dt^2} + \frac{\Omega^2}{4}(b + 2q\cos(\Omega t)y) = 0$$
$$\frac{d^2z}{dt^2} + \frac{\Omega^2 b}{2}z = 0 \tag{3.4}$$

where b is given by:

$$b = \frac{e\alpha V_{cap}}{ML^2\Omega^2}. \tag{3.5}$$

Here L is the distance between the endcap electrodes and α is a numerical factor which depends on the trap geometry. The equation of motion for the axial direction is solved by a harmonic motion with a frequency of:

$$\omega_z = \sqrt{\frac{b}{2}}\Omega. \tag{3.6}$$

Adding an axial potential has also a defocusing effect on the frequency of the motion in the radial harmonic pseudopotential, which is now given by:

$$\omega_r = \sqrt{\omega_{r0}^2 - \frac{1}{2}\omega_z^2} \tag{3.7}$$

However in the case of our experiment we have $\omega_{r0} \gg \omega_z$ and therefore this effect can be neglected.

3.2. Equilibrium positions

In the following we consider N ions stored in a linear Paul trap, where the ions are assumed to be strongly bound in the radial direction but weakly bound by a harmonic potential in the

axial direction. In this case the ions will arrange themselves in a linear chain configuration[1]. The potential energy of the string with N ions of mass M and charge e is given by:

$$U = \frac{M}{2} \sum_{n=1}^{N} \omega_z^2 z_n^2 + \frac{e^2}{8\pi\epsilon_0} \sum_{n,m=1;m\neq n}^{N} \frac{1}{|z_n - z_m|}. \tag{3.8}$$

Here we only take the axial direction into account, assuming a linear configuration with $x_n = y_n = 0$. The first term is the potential energy of the ions in the axial trap potential, while the second one describes the ions' mutual Couloumb interaction. The equilibrium positions $z_n^{(0)}$ can be determined by the following equation:

$$\left[\frac{\partial U}{\partial z_n} \right]_{z_n = z_n^{(0)}} = 0. \tag{3.9}$$

For $N = 2$ and $N = 3$ this equation can be solved analytically [78]:

$$N = 2: \quad z_1 = -\left(\frac{1}{2} \right)^{2/3} l, \, z_2 = \left(\frac{1}{2} \right)^{2/3} l \tag{3.10}$$

$$N = 3: \quad z_1 = -\left(\frac{5}{4} \right)^{1/3} l, \, z_2 = 0, \, z_3 = \left(\frac{5}{4} \right)^{1/3} l, \tag{3.11}$$

where the length scale l is defined as:

$$l = \left(\frac{e^2}{4\pi\epsilon_0 M \omega_z^2} \right)^{1/3} \tag{3.12}$$

For more than three ions the equation has to be solved numerically. The distance between the ions is minimal at the center and increases towards the outside of the string. The minimum separation between the ions can be approximated up to $N \simeq 1000$ by:

$$\Delta z_{min} \cong 2.0 \cdot \ln^{-0.57} \tag{3.13}$$

With an increasing number of ions the minimum separation between the ions decreases. Quantum computing using trapped ions requires the ability to apply laser pulses to single ions without affecting the other ions within a crystal. For an increasing number of ions in the same trap, it therefore becomes increasingly difficult to meet this requirement.

3.3. Normal modes

Considering only small oscillations around the equilibrium positions $y_n^{(0)} = 0$, $x_n^{(0)} = 0$, $z_n^{(0)}$, the equation of motions can be solved and a set of of normal modes and the respective oscillation frequencies be obtained. Here only the results of such a calculation will be discussed, a detailed treatment can be found in [78]. For an ion crystal with N ions, where we assume the motions

---

[1]If the ratio between the radial and the axial trap depth is not large enough or a large number of ions is stored in the trap a transition to a zig-zag configuration is possible. More details about the stability of the linear ion configuration can be found in [77]
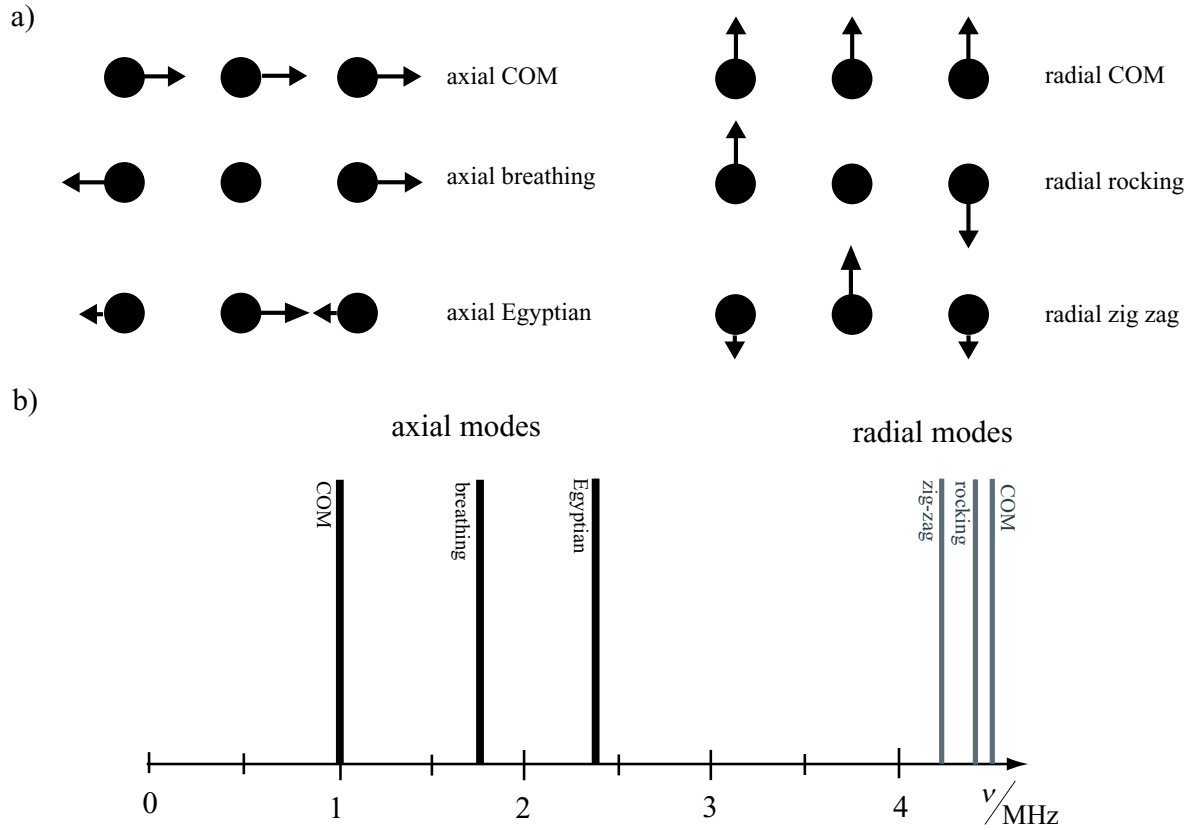
Figure 3.2.: a) Normal modes for a three ion crystal are shown. The arrows indicate the direction in which the ions move with respect to each other. Ions without an arrow are not moving, as is the case for the axial breathing and radial rocking mode. The length of the arrows indicates the amplitude of oscillation. For the axial Egyptian and radial zig-zag mode, the central ion has twice the amplitude as the outer ions. b) Spectrum of oscillation frequencies. An excitation spectrum of an atomic transition will show the same features. The normal modes will show up as sidebands in the excitation spectrum.

in the radial x-y plane to be degenerate, a set of N axial and a set of $2N$ radial modes is obtained.

The principal mode in the axial direction is the *center of mass* or axial COM mode in which all ions oscillate together with the same amplitude. The oscillation frequency of the COM mode is ω_z, the single ion axial trap frequency, which is given by Eq. 3.6. All higher order modes have larger frequencies. The second axial mode is called the *breathing mode* and has a frequency of $\sqrt{3}\omega_z$. The frequencies of the center of mass and the breathing mode are independent on the number of ions. For higher order modes the vibrational frequency depends on the number of ions. However for $N \leq 10$ this dependence is very weak, such that the axial mode frequency are to high degree of accuracy given by $\{1, \sqrt{3}, \sqrt{29/5}, 3.051, 3.671, 4.272, 4.864, 5.443, 6.013, 6.576\}$ in units of ω_z.

In the radial set of normal modes the principal mode is again the center of mass mode, where the ions oscillate with frequency ω_r (see Eq. 3.7). In contrast to the case of the axial modes, all higher order radial modes have a lower oscillation frequency than the center of mass mode. The eigenvectors of the radial normal modes are formally identical to the eigenvectors of the axial modes. In Fig. 3.2(a) all axial and radial modes of a three ion crystal are depicted. The corresponding spectrum of oscillation frequencies is given in Fig. 3.2(b).

3. Linear Paul traps

4. Laser–Ion Interaction

4.1. The Hamiltonian

An ion trapped in a harmonic potential with frequency ω interacting with a travelling wave from a single mode laser tuned close to a transition can be treated as an effective two level system. The Hamiltonian of the ion in the absence of interaction with the light field is given by:

$$H_0 = H^{(m)} + H^{(e)} \tag{4.1}$$

$$H^{(m)} = \frac{p^2}{2m} + \frac{1}{2}m\omega^2 x^2 \tag{4.2}$$

$$H^{(e)} = \frac{1}{2}\hbar\omega_a\sigma_z. \tag{4.3}$$

Here the Hamiltonian $H^{(m)}$ describes the motion in the harmonic potential, while $H^{(e)}$ describes the ion's internal electronic state. The Hamiltonian for the interaction of the light field with the ion is:

$$H^{(i)} = \frac{1}{2}\hbar\Omega\left(\sigma^+ + \sigma^-\right)\left(e^{i(k\hat{x}-\omega_l t+\phi)} + e^{-i(k\hat{x}-\omega_l t+\phi)}\right), \tag{4.4}$$

where k is the wave number, ω_l the frequency and ϕ the phase of the travelling light wave. All details about the exact form of the atom-light interaction are included in the coupling constant Ω, which is usually called the *Rabi frequency*.

The harmonic motion of the ion can be described using creation and annihilation operators $a^\dagger$ and a. Then the Hamiltonians $H^{(m)}$ and $H^{(i)}$ can be expressed as:

$$H^{(m)} = \hbar\omega\left(a^\dagger a + \frac{1}{2}\right) \tag{4.5}$$

$$H^{(i)} = \frac{1}{2}\hbar\Omega\left(e^{i\eta(a+a^\dagger)}\sigma^+ e^{-i(\omega_l t+\phi)} + e^{-i\eta(a+a^\dagger)}\sigma^- e^{i(\omega_l t+\phi)}\right). \tag{4.6}$$

Here the *Lamb Dicke parameter* η is used, which is defined by[1]

$$\eta = k\sqrt{\frac{\hbar}{2m\omega}}. \tag{4.7}$$

The transformation into the interaction picture is done with the free Hamiltonian $H_0 = H^{(m)} + H^{(e)}$ and the interaction Hamiltonian $V(t) = H^{(i)}$. In the interaction picture, defined by the

---

[1]An angle β between the oscillation axis and the wavevector k, has to be taken into account by setting $\eta = k\cos\beta\sqrt{\hbar/2m\omega}$.

transformation $H_{int} = U^\dagger V(t)U$ with $U = e^{iH_0t/\hbar}$, the transformed interaction Hamiltonian is:

$$H_{int}(t) = \frac{\hbar}{2}\Omega\left(\sigma^+ e^{i\eta(ae^{-i\omega t}+a^\dagger e^{i\omega t})}e^{i(\phi-\delta t)} + H.c.\right), \tag{4.8}$$

where $\delta = \omega_l - \omega_a$. Here terms oscillating with frequency $(\omega_l + \omega_a)$ have been omitted, i.e. the *rotating wave approximation* has been applied.

Depending on the detuning δ, this interaction Hamiltonian will couple certain motional and electronic states. An expansion of the exponentials containing the annihilation and creation operators of the harmonic oscillator will result in a sum of terms of the form $\sigma_\pm a^l a^{\dagger m}$. If $\delta \approx (l-m)\omega$ these terms will result in a coupling of the level $|S\rangle|n\rangle$ with $|D\rangle|n+s\rangle$, where $|S\rangle$ and $|D\rangle$ denote the two electronic states of our two-level system and $s = l - m$. The Rabi frequency for this transition is given by:

$$\Omega_{n,n+s} = \Omega\|\langle n+s|\,e^{i\eta(a+a^\dagger)}\,|n\rangle\|. \tag{4.9}$$

Transitions of this kind are called the $|s|$th blue ($s > 0$) or red ($s < 0$) sideband transition. In the special case where $s = 0$, in which only the electronic state is changed while the vibrational state is unaffected, the transitions are denoted as *carrier transitions*.

4.2. Lamb Dicke limit

The calculation of the interaction Hamiltonian in Eq. 4.8 and the Rabi frequencies in Eq. 4.9 can be simplified in the so-called *Lamb-Dicke regime*, in which the extension of the ions wavefunction is much smaller than the light field's wavelength. In this regime the inequality $\eta^2(2n+1) \ll 1$ must be fulfilled. The exponential in Eq. 4.8 can be expanded and only terms in lowest order in η are kept, such that we obtain:

$$H_{LD} = \frac{\hbar}{2}\Omega\sigma^+\{1 + i\eta(ae^{-i\omega t} + a^\dagger e^{i\omega t}\}e^{i(\phi-\delta t)} + H.c. \tag{4.10}$$

This Hamiltonian will give rise to three resonances. For $\delta = 0$ the *carrier transition* is excited and the Hamiltonian is:

$$H_{car} = \frac{\hbar}{2}\Omega(\sigma^+ e^{i\phi} + \sigma^- e^{-i\phi}). \tag{4.11}$$

This Hamiltonian couples the levels $|S\rangle|n\rangle$ and $|D\rangle|n\rangle$ with a Rabi frequency Ω.

For $\delta = -1$ the resonance is called the *red sideband* and the Hamiltonian is:

$$H_{rsb} = \frac{\hbar}{2}\Omega(a\sigma^+ e^{i\phi} + a^\dagger\sigma^- e^{-i\phi}), \tag{4.12}$$

which gives rise to transitions of the type $|S\rangle|n\rangle \longleftrightarrow |D\rangle|n-1\rangle$ with Rabi frequency

$$\Omega_{n,n-1} = \Omega\sqrt{n}\,\eta. \tag{4.13}$$

The third resonance occurs for $\delta = +1$ and is called the *blue sideband*. In this case the Hamiltonian takes the form:

$$H_{bsb} = \frac{\hbar}{2}\Omega(a^\dagger\sigma^+ e^{i\phi} + a\sigma^- e^{-i\phi}). \tag{4.14}$$

Here transitions of the kind $|S\rangle|n\rangle \longleftrightarrow |D\rangle|n+1\rangle$ occur with a Rabi frequency

$$\Omega_{n,n+1} = \Omega\sqrt{n+1}\,\eta. \tag{4.15}$$

4.3. Generalizations of the Model

So far only the laser-ion interaction of a single ion trapped in a one-dimensional potential was discussed. In the following the results from the previous section will be generalized to three-dimensional systems of multiple ions.

4.3.1. Three-dimensional potential

Generalizing the results obtained for one dimension to three dimensions is straightforward, since it only involves replacing products kx by the scalar product of the vectors $\vec{k} \cdot \vec{r}$. Therefore, the operator $\exp(i\eta(a^\dagger + a))$ in the one-dimensional case, takes the form $\exp(i\vec{k} \cdot \vec{r}) = \exp i \sum_l \eta_l(a_l^\dagger + a_l)$ in three dimensions, where the sum runs over all normal modes of the three-dimensional harmonic oscillator and $a_l^\dagger$ and a_l are the creation and annihilation operators of the harmonic oscillator's normal modes.

The Rabi frequency of a transition changing only the phonon number of one vibrational mode is given by $\Omega_{n,n+s} = \Omega \|\langle n + s, ...| \exp i \sum_l \eta_l(a_l^\dagger + a_l)|n, ...\rangle\|$. Again, in the Lamb-Dicke-regime this can be approximated using a Taylor expansion. For instance by applying the expansion up to second order and keeping only first order terms of the operator $a_i^\dagger$, the blue sideband Rabi frequency of the mode i is given by:

$$\Omega_{n_i,n_{i+1}} = \Omega \eta_i \sqrt{n_i + 1} \left[1 - \sum_{l \neq i} \eta_l^2(2n_l + 1) \right]. \tag{4.16}$$

Therefore, the Rabi frequency of a sideband transition will slightly depend on the population of all other vibrational modes.

4.3.2. Multiple-ion-crystal

For a crystal of N ions the interaction of the light field with each of the ions and $3 \times N$ normal modes have to be taken into account, such that the interaction Hamiltonian for one ion in Eq. 4.8 becomes:

$$H_{\text{int}} = \frac{\hbar}{2} \sum_{j=1}^{N} \Omega_j \sigma_j^+ \exp\left(i \sum_l \eta_l^j(a_l^\dagger + a_l) \right) e^{-i(\omega_L t - \phi_j)} + H.c. \tag{4.17}$$

In the experiments presented in this thesis the laser beam is focussed on one of the ions at a time, such that coupling to all other ions is negligible and the sum over j can be dropped.

4.4. Spectroscopy with ^{40}Ca$^+$

4.4.1. Level scheme

In the experiments presented in this thesis the ion species of choice was ^{40}Ca$^+$. The level scheme containing only the important transitions is shown in Fig. 4.1. As can be seen in the level scheme four transitions are driven by laser radiation. The quadrupole transition from
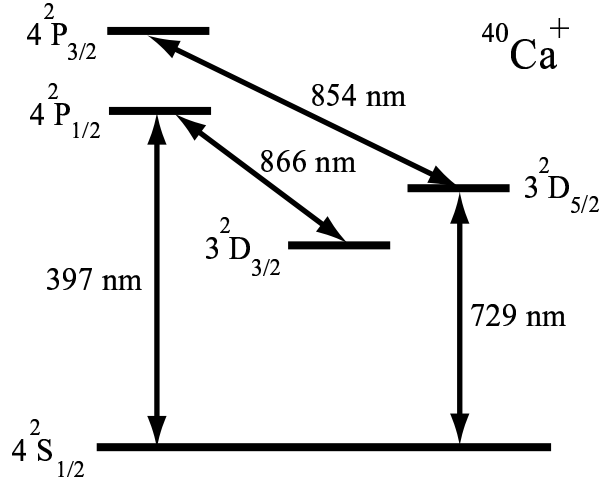
Figure 4.1.: Level scheme for ^{40}Ca containing only the states which are populated within our experiments.

the $S_{1/2}$ ground state to the $D_{5/2}$ state is used to implement the qubit, i.e. the logical states $|0\rangle$ and $|1\rangle$ are associated with these levels and laser pulses at 729 nm are used to carry out unitary operations. Furthermore this transition is used for sideband cooling of the ion string to the ground state of the vibrational modes.

The dipole transition connecting the $S_{1/2}$ ground state and the $P_{1/2}$ state serves two purposes, namely the Doppler laser cooling of the ion string and the detection of the qubit's state. Additionally two light fields at 866 nm and 854 nm are used to deplete the metastable D-levels.

4.4.2. The $S_{1/2} \leftrightarrow P_{1/2}$ transition

The transition $S_{1/2} \leftrightarrow P_{1/2}$ is at a wavelength of $\lambda = 397$ nm and has a linewidth of 20.7 MHz. The $P_{1/2}$ level decays with 7 % (branching ratio 15 : 1) probability into the metastable $D_{3/2}$ state. Therefore, in order to avoid optical pumping into this state, the $D_{3/2} \leftrightarrow P_{1/2}$ transition at 866 nm is excited to deplete the $D_{3/2}$ level.

Doppler cooling

For Doppler laser cooling the laser at 397 nm is red detuned by approximately half of the linewidth, i.e. $\delta = 10$ MHz. The influence of the decay from the $P_{1/2}$ to the $D_{3/2}$ level due to the favorable branching ratio is negligible, such that the cooling limit can be expected to be close to the theoretical limit for Doppler cooling of a two-level-atom.

Qubit state detection

The qubit's state can be read out by employing an *electron shelving technique*. Applying light at 397 nm and thereby driving the $S_{1/2} \leftrightarrow P_{1/2}$ transition will cause a $S_{1/2} - D_{5/2}$ superposition

to collapse and project the ion onto either the $S_{1/2}$ or $D_{5/2}$ state. In case of projection onto the $S_{1/2}$ state the ion will interact with the light at 397 nm and resonance fluorescence can be detected, while in the case of projection onto the $D_{5/2}$ state no fluorescence will be detected. Therefore by detecting the presence or absence of the strong fluorescence signal at 397 nm the qubit's state after projection can be determined. By repeatedly preparing the ion in the same quantum state and measuring the fluorescence the $D_{5/2}$ population can be determined. The detection efficiency of this method can be as high as 99.9 % and is only limited by the finite lifetime of the $D_{5/2}$ level [64].

4.4.3. The $\mathbf{S_{1/2} \leftrightarrow D_{5/2}}$ transition

The $S_{1/2} \leftrightarrow D_{5/2}$ quadrupole transition is at a wavelength of 729 nm. Since this transition is dipole forbidden, the $D_{5/2}$ level is a metastable level with a lifetime of $\tau \approx 1s$.

In order to return the ions into the ground state at the beginning of every experiment and to achieve sideband cooling at a reasonable rate it is necessary to deplete the $D_{5/2}$ level without relying solely on spontaneous decay. For this purpose the $D_{5/2} \leftrightarrow P_{3/2}$ transition can be excited with light at 854 nm. From the $P_{3/2}$ level the ions will most probably decay back into the S ground state. With a small probability a decay back into one of the $D_{5/2}$ or $D_{3/2}$ levels occurs, where the latter, as mentioned above, can be depleted by light at 866 nm.

Zeeman structure

The $S_{1/2}$ ground state has two Zeeman sublevels with $m = \pm 1/2$ and the $D_{5/2}$ six Zeeman sublevels with $m = \pm 1/2, \pm 3/2, \pm 5/2$. For a quadrupole transition changes in the magnetic quantum number of $\Delta m' = 0, 1, 2$ are allowed, which results in ten possible transitions between the magnetic sublevels. These transitions have different coupling strength depending on the (m, m') combination and the angles between the light's wave vector $\mathbf{k}$ and the polarization ϵ and the direction of an externally applied magnetic field $\mathbf{B}$.

In case of a quadrupole transition the induced electric quadrupole moment of the ion Q couples to gradient of the electromagnetic field. Therefore, the Hamiltonian given by:

$$H_I = Q \nabla E(t) \tag{4.18}$$

is obtained. If this interaction Hamiltonian is written in the form of Eq. 4.4 the Rabi frequency is defined by [68]:

$$\Omega = \left| \frac{eE_0}{2\hbar} \left\langle S_{1/2}, m \left| (\epsilon \cdot \mathbf{r})(\mathbf{k} \cdot \mathbf{r}) \right| D_{5/2}, m' \right\rangle \right|, \tag{4.19}$$

where E_0 is the electric field amplitude, $\mathbf{r}$ is the position operator of the valence electron relative to the atom's center of mass and m and m' denote the magnetic quantum numbers. This expression for the Rabi frequency can be further evaluated, such that we obtain:

$$\Omega = \kappa E_0 \sqrt{\frac{A}{k^3}} \Lambda(m, m') g^{(\Delta m)}(\phi, \gamma), \tag{4.20}$$

with

$$\kappa = \frac{e}{2\hbar} \left(\frac{15}{c\alpha} \right)^{1/2} = 30.089 \cdot 10^{12} V^{-1} (sm)^{-1/2}.$$

Here A is the spontaneous decay rate of the $D_{5/2}$ level. The factors $\Gamma(m, m')$ are the specific Clebsch-Gordan coefficients, which in the case of our $S_{1/2} \leftrightarrow D_{5/2}$ transition are given by:

m	-1/2	-1/2	-1/2	-1/2	-1/2
m'	-5/2	-3/2	-1/2	1/2	3/2
$\Lambda(m, m')$	1	$\sqrt{4/5}$	$\sqrt{3/5}$	$\sqrt{2/5}$	$\sqrt{1/5}$

Here only the coefficients for the case $m = -1/2$ are listed. The coefficients for $m = +1/2$ can be derived using the fact that the $\Lambda(m, m')$ are invariant under the inversion $(m \to -m; m' \to -m')$.

The functions $g^{(\Delta m)}(\phi, \gamma)$ contain the geometry dependence of Ω. Here ϕ denotes the angle between light's k vector and the magnetic field and γ the angle between the polarization and the magnetic field vector projected onto the plane of incidence. Explicit expressions for these functions can be found in [64,68]. In the specific geometry of our experiment, we have $\phi = 45°$ and $\gamma = 0$ and the values for the $g^{(\Delta m)}$ are:

$$g^{(\Delta m=0)} = \frac{1}{2}$$

$$g^{(\Delta m=1)} = 0$$

$$g^{(\Delta m=2)} = \frac{1}{\sqrt{24}}$$

Therefore in the chosen geometry transitions with $\Delta m = 1, 2$ are suppressed. Additionally, in the experiment the ion's state is prepared in the $m = -1/2$ by σ^- polarized light at 397 nm, before starting coherent operations on the $S_{1/2} \leftrightarrow D_{5/2}$ transition, such that only three available transitions, namely $S(m = -1/2) \leftrightarrow D(m' = -5/2, -1/2, 3/2)$ are left. In Fig. 4.2(a) the squared Clebsch-Gordan coefficients are shown and in (b) the relative line strength ($\propto \Omega^2$) for the geometry $\gamma = 0°$ and $\phi = 45°$ are given.

4.5. Manipulating ion qubits with laser pulses

In Sec. 2.5 the fundamental operations necessary to implement any kind of unitary operation on a quantum computer were shown. In order to implement a quantum computer using trapped ^{40}Ca ions, these operations have to be realized by employing the laser-ion interaction described in the previous section.

Our qubits consist of the ground state $S_{1/2}(m = -1/2)$ and the metastable $D_{5/2}(m = -1/2)$ state of ^{40}Ca ions. These states will often only be denoted by $|S\rangle$ and $|D\rangle$, without explicitly giving all quantum numbers. Furthermore these states are mapped to the logical basis states by $|S\rangle \leftrightarrow |1_L\rangle$ and $|D\rangle \leftrightarrow |0_L\rangle$. For a state of N ions the notation is[2]

$$|ion\ N, ..., ion\ 3, ion\ 2, ion\ 1\rangle.$$

The qubit's quantum state is manipulated by laser pulses of 729 nm light, which couples to the $|S\rangle \leftrightarrow |D\rangle$ transition. The corresponding interaction Hamiltonian was given in Eq. 4.11

---

[2]The definition of the logical states and the notation will be consistently used in this thesis. However, one has to be careful when referring to earlier publications of the presented results, in which often other conventions were used.

a)

b)

Figure 4.2.: Zeeman splitting of the quadrupole transition in a non-zero magnetic field. The splitting is drawn in units of $u = \mu_b B/h$. The height of the components in a) is given by the squared Clebsch-Gordan coefficients. All ten allowed transitions are shown. b) Height of the components is given by the square of the product of geometric factors $g^{(\Delta m)}$ and the Clebsch-Gordan coefficients. Because of the chosen geometry $\phi = 45°, \gamma = 0°$ only six transitions are left.

for carrier transitions and in Eq. 4.14 for blue sideband transitions. In order to express the length of laser pulses independent of the actual Rabi frequency, the angle $\theta = \Omega \cdot t$ will be used, which is identical to the angle of rotation used in Eq. 2.5-2.7. Throughout this thesis the length of pulses will be given in units of this angle, i.e a pulse of length π actually means a pulse of length $t = \pi/\Omega$. In the following, the action of carrier and sideband laser pulses on a string of ions will be discussed in the context of implementing the operations necessary for a quantum computer

4.5.1. Carrier transitions

Laser pulses resonant with the carrier of the $S_{1/2} \leftrightarrow D_{5/2}$ transition, realize the single qubit rotations introduced in Sec. 2.1. A laser pulse of length θ and phase ϕ corresponds to the unitary operation:

$$R(\theta, \phi) = \exp\left(\frac{i}{\hbar}H_{car}\theta\right) = \exp\left(i\hbar\frac{\theta}{2}(\sigma^+ e^{i\phi} + \sigma^- e^{-i\phi})\right). \tag{4.21}$$

Using the identity given in Eq. 2.7 this can be transformed into the more convenient form:

$$R(\theta, \phi) = \cos\left(\frac{\theta}{2}\right)I + i\sin\left(\frac{\theta}{2}\right)\begin{pmatrix} 0 & e^{i\phi} \\ e^{-i\phi} & 0 \end{pmatrix} \tag{4.22}$$

By comparing this equation with Eq. 2.7, we see that this unitary operation corresponds to a rotation of the Bloch vector around an axis lying in the x-y-plane. The special cases of rotations around the x and y-axes, as given in Eq. 2.5, are realized by the following laser pulses:

$$R_x(\theta) = R(\theta, \pi) \qquad R_{\bar{x}}(\theta) = R(\theta, 0)$$
$$R_y(\theta) = R(\theta, 3\pi/2) \qquad R_{\bar{y}}(\theta) = R(\theta, \pi/2), \tag{4.23}$$

where $\bar{x}$ and $\bar{y}$ denote rotations around the $-x$ and $-y$-axis, respectively. Those operations are already sufficient to implement any kind of single qubit operation, since every rotation around an axis $\bar{n}$ can be decomposed in rotations around the x and y-axis or in general in rotations around any pair of non-collinear axes. A rotation $R_z(\theta)$ around the z-axis can for example be replaced by:

$$R_z(\theta) = R\left(\frac{\pi}{2}, \pi\right) \cdot R\left(\theta, -\frac{\pi}{2}\right) \cdot R\left(\frac{\pi}{2}, 0\right) \tag{4.24}$$

A widely used operation is the Hadamard transformation given in Eq. 2.3, which implements the transformation $|0\rangle \leftrightarrow (|0\rangle + |1\rangle)/\sqrt{2}$ and $|1\rangle \leftrightarrow (|0\rangle - |1\rangle)/\sqrt{2}$. This operation can be decomposed into rotations around the x- and y-axis by:

$$H = -i\, R_{\bar{y}}\left(\frac{\pi}{4}\right) \cdot R_{\bar{x}}\left(\frac{\pi}{2}\right) \cdot R_y\left(\frac{\pi}{4}\right). \tag{4.25}$$

Instead of using this sequence of three rotations, we usually mimic the action of the Hadamard operation by applying single $\pi/2$ pulses, where equal superpositions are prepared by a $R_{\bar{x}}(\pi/2)$ rotation and the corresponding inverse operation is implemented by a $R_x(\pi/2)$ rotation.
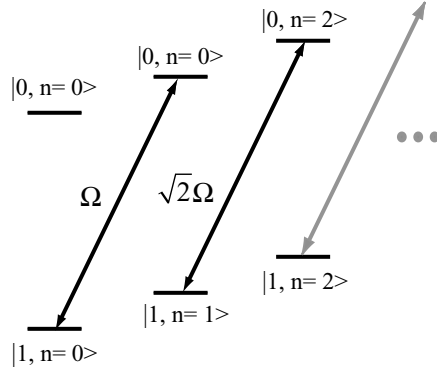
Figure 4.3.: Ladder of energy levels of one vibrational mode and the ion's internal states. Arrows indicate coupling due to excitation of the blue sideband.

4.5.2. Sideband transitions

Laser pulses set to a frequency of one of the vibrational sidebands are an additional tool available in ion traps. By driving a sideband transition the state of the ion string's corresponding vibrational mode is manipulated. Provided its vibrational state is well defined, the respective vibrational mode can serve as an additional qubit. However, this additional "qubit" is not only attributed to a single ion but rather belongs to and is accessible from all ions within an ion string.

In our experiments we have so far exclusively employed blue sideband transitions for qubit manipulation and therefore the discussion will be limited to this kind of transition. The interaction Hamiltionian for blue sideband transitions was given in Eq. 4.14. A laser pulse of length $\theta = t/\Omega_{\mathrm{blue}}$ and phase ϕ, will correspond to a unitary operation given by:

$$R^+(\theta, \phi) = \cos\left(\frac{\theta}{2}\right) I + i \sin\left(\frac{\theta}{2}\right) \left(a^\dagger \sigma^+ e^{i\phi} + a\sigma^- e^{-i\phi}\right), \qquad (4.26)$$

where $a^\dagger$ and a are the creation and annihilation operators of the harmonic oscillator attributed to the respective vibrational mode. The pulse notation given in Eq. 4.27 will often be used with an additional subscript, as $R_n^+(\theta, \phi)$, where the subscript n indicates the number of the ion adressed by the laser pulse.

The dynamics given by Eq. 4.27 is more complicated than the simple two-level dynamics in the case of carrier transitions. The harmonic oscillator provides a system of an infinite number of equidistant levels, where an operation $R^+(\theta, \phi)$ will couple all neighboring levels $|n\rangle \leftrightarrow |n+1\rangle$ apart from coupling the ion's internal qubit states $|S\rangle$ and $|D\rangle$. The ladder of the harmonic oscillator and the ion's internal states is illustrated in Fig. 4.3. An additional problem arises from the fact that the coupling strength of the transition $|S, n\rangle \leftrightarrow |D, n+1\rangle$ depends on the phonon number n with $\Omega_{\mathrm{blue}} \propto \sqrt{n+1}$. Therefore, a pulse of given length will result in different rotations of the Bloch vector for each pair of levels $|S, n\rangle \leftrightarrow |D, n+1\rangle$.

In spite of these difficulties vibrational modes can be employed as an effective qubit by restricting the vibrational levels which are populated in course of a pulse sequence to $|0\rangle$ and $|1\rangle$, such that the available computational subspace is given by $\{|D, 0\rangle, |D, 1\rangle, |S, 1\rangle, |S, 0\rangle\}$.

In the following two examples for blue sideband operations will be given, which will be used frequently in the experiments presented in this thesis.

Pseudo-SWAP: Consider the action of a laser pulse $R^+(\pi, -\pi/2)$, which will transfer a superposition of an internal qubit $(\alpha|S\rangle + \beta|D\rangle)|0\rangle$ to $|D\rangle(\alpha|1\rangle + \beta|0\rangle)$, i.e such a pulse swaps the state of the internal qubit with the vibrational state. However, this is only a valid SWAP operation as long as the vibrational mode is in $|n = 0\rangle$ prior to the operation. An initial population of $|n = 1\rangle$ would be partially transferred to the $|n = 2\rangle$ state and would therefore leave the computational subspace. A full SWAP operation allowing a population of $|n = 1\rangle$ would require a more sophisticated pulse sequence employing the composite pulse technique (c.f. [66, 68, 79]).

Entangling electronic and vibrational state: Another interesting example is the action of $R^+(\pi/2, 0)$ pulse, which transfers an ion from the $|S, 0\rangle$ state to a $(|S, 0\rangle + |D, 1\rangle)/\sqrt{2}$ superposition. Formally this state can be considered as an entangled state of the vibrational qubit with the internal qubit of the ion. Of course this kind of entanglement is of limited use, since both qubits cannot be separated spatially nor a separate measurement of one of the qubits without affecting the other is possible. However, applying our previously discussed SWAP operation $R^+(\pi, -\pi/2)$ to another ion in the string, which has been prepared in the $|D\rangle$ state prior to this operation, will map the vibrational mode's state onto the internal state of this ion and will therefore create an entangled state of two ions. This technique will be employed in Ch. 7 in order two create pairs of entangled ion qubits.

4.6. Non-resonant interactions

So far only resonant interactions have been considered. However, non-resonant interactions have to be taken into account, especially when working with sideband transitions. Due to the small coupling strength of these transitions, which is only 1-2 % of the coupling strength to a carrier transition (c.f. Eq. 4.15) higher light intensities are usually employed to achieve sufficiently high Rabi frequencies. These high light intensities increase problems with non-resonant coupling to the much stronger carrier transitions. In the following discussion, population transfers and light shifts due to this coupling will be discussed.

4.6.1. Population Transfer

A light field resonant with the $|S, 0\rangle \leftrightarrow |D, 1\rangle$ transition, will drive Rabi oscillations on this transition[3]. At the same time this light field will non-resonantly drive Rabi oscillations on the carrier transition $|S, 0\rangle \leftrightarrow |D, 0\rangle$. In order to understand this effect, consider the time dependence of the population of the upper level, which is obtained as the solution of the Bloch equations [80]:

$$P_D = \frac{\Omega^2}{\Omega^2 + \Delta^2} \sin^2\left(\frac{1}{2}\sqrt{\Omega^2 + \Delta^2}\, t\right), \tag{4.27}$$

where $\Delta = \omega_l - \omega_a$ is the detuning of the light field's frequency from the atomic resonance frequency. In case of the resonantly excited $|S, 0\rangle \leftrightarrow |D, 1\rangle$ sideband transition, we have $\Delta = 0$

---

[3]Here it is assumed that the respective vibrational mode is cooled to the ground state $|n = 0\rangle$, such that we only have to consider sideband transitions between levels with $n = 0$ and $n = 1$.

and therefore Rabi oscillations with Rabi frequency Ω_{blue} and an amplitude of one will occur. Rabi oscillations due to non-resonant excitation of the carrier have a frequency $\sqrt{\Omega_{\text{car}}^2 + \Delta^2}$ and an amplitude of $1/(1 + (\Delta/\Omega)^2)$, where we have $\Omega_{\text{car}} = \Omega_{\text{blue}}/\eta$.

In order to implement quantum computations with high fidelity, it is required to implement the operations shown in Sec. 4.5 as perfect as possible. Unwanted non-resonant excitation of the carrier transition will transfer populations into the wrong states of the computational subspace. Therefore it is desirable to keep the amplitude of the off-resonant Rabi oscillations given by:

$$A_{\text{off-resonant}} = \frac{1}{1 + [\frac{\eta \Delta}{\Omega_{\text{blue}}}]^2}, \tag{4.28}$$

as small as possible by reducing the Rabi frequency Ω_{blue} on the sideband transition. This measure will however increase the time necessary for operations containing sideband pulses, which limits the number of operations, that can be carried out within the coherence time of the qubits. Therefore, setting the Rabi frequency of the sideband transition is a trade-off between the speed of the quantum gates and the quality of these gates.

In our experiments, the blue sideband transition belonging to the center-of-mass mode is usually excited with a Rabi frequency on the order of $\Omega_{\text{blue}} = 2\pi \cdot 5$ kHz. Typically, the center-of-mass mode will be 1.2 MHz away from the carrier resonance and will have a Lamb-Dicke parameter of $\eta = 2.4$ %. The non-resonant Rabi oscillation of the carrier transition are expected to have a frequency of $\Omega_{rabi} = 2\pi \cdot 1.22$ MHz and an amplitude of $3 \cdot 10^{-2}$.

4.6.2. Light Shifts

A non-resonant light field will shift atomic levels, an effect known as *light shift* or *AC-Stark-effect*. Suppose the unperturbed energy difference of two atomic levels is given by $E = \hbar \omega_A$ and the light field is detuned by $\Delta = \omega_L - \omega_A$ from the unperturbed transition frequency, where ω_L is the frequency of the light field. Further suppose that the light field's intensity is such that the Rabi frequency is given by Ω. Then, the energetically lower level will be shifted by $\Omega^2/4\Delta$ and the energetically upper level by $-\Omega^2/4\Delta$, where the level shifts are given in units of angular frequency. These shifts will result in a change of the atomic resonance frequency by $\Omega^2/2\Delta$, which is illustrated in Fig. 4.4 for both signs of the detuning Δ. For red-detuned light ($\Delta < 0$) the transition frequency is shifted to a larger frequency, while in case of blue-detuned light ($\Delta > 0$) the transition frequency is shifted to a lower frequency. Unlike non-resonant population transfers, light shifts can be cancelled. The corresponding compensation technique will be introduced in Sec. 6.4.
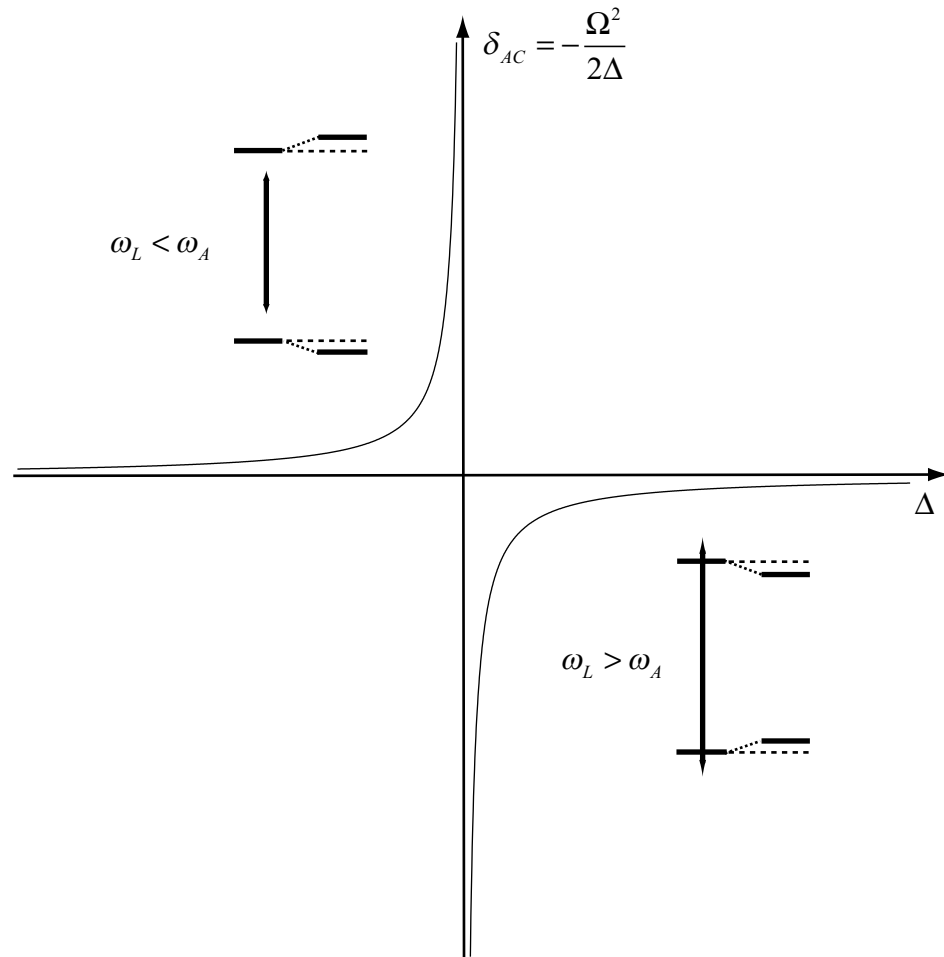
Figure 4.4.: Light shift of the resonance frequency of a transition depending on the detuning Δ. For red-detuned light the resonance frequency is shifted to a higher frequency, while for blue-detuned light the resonance frequency is shifted to a lower frequency. In case the light is at resonance with the transition ($\Delta = 0$) no light shift occurs.

5. Experimental Setup

5.1. Linear Ion Trap

The linear ion trap used in this PhD thesis, was designed by Stephan Gulde and the specifications and design are thoroughly discussed in his PhD thesis [68]. A picture and schematic drawings of the trap can be seen in Fig. 5.1. One of the major goals of this trap design was to increase the trap frequencies in the radial and axial direction with respect to earlier trap designs by decreasing the size of the trap [63, 65].

As can be seen in Fig. 5.1 the radial trap electrodes have a blade-like shape. This design was chosen because such a structure can be machined with higher precision than rod-like electrodes which were used in earlier experiments.
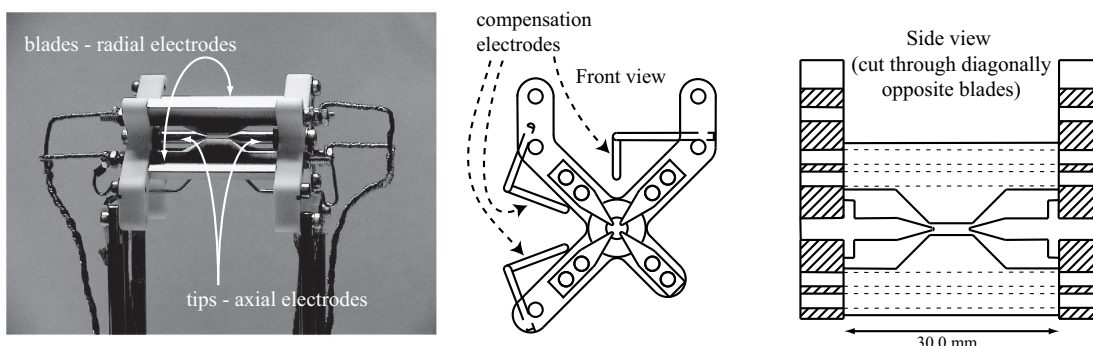

Figure 5.1.: Picture and a schematic drawing of the linear ion trap. The distance between the axial electrodes is $L = 5.0$ mm, the diagonal distance between two radial electrodes $r = 1.6$ mm. Picture and drawings from [68].

The ion trap is operated at a drive frequency of 23.5 MHz. The radiofrequency power of up to 15 W is produced by a signal generator and an RF-amplifier. The RF power is adjustable by a variable attenuator. The radiofrequency signal is then coupled into a helical resonator, which is driven at its resonant frequency and therefore enhances the RF amplitude. The axial trap potential is created by applying a DC voltage of up to 2000 V to the endcap electrodes.

A standard choice for the trap parameters in the experiments presented in this thesis were an RF power of $P = 11 - 12$ W and an endcap voltage of $V = 1000$ V. With such a configuration the frequency of the center-of-mass mode in the radial direction was $\omega_r \approx 2\pi \cdot 4.4$ MHz and in the axial direction $\omega_z \approx 2\pi \cdot 1.2$ MHz. In this configuration the chosen parameters are below

their maximum values and therefore the trap frequencies are not as high as possible. But at higher RF powers or endcap voltages it was observed that the ions more frequently left the desired linear crystal configuration, which is supposedly due to nonlinear resonances of the ion's oscillations.

5.2. Laser Systems

In Sec. 4.4.1 on page 26 a part of the level scheme of $^{40}Ca^+$ was shown, containing the transitions important for our experiments. Four laser sources are needed, a laser at 397 nm to cool and monitor the ions, one at 729 nm to drive the qubit transition and lasers at 866 and 854 nm to deplete the metastable D-levels.

Fig. 5.2 gives an overview of the laser systems and the optical setup. The setup is spread over two optical tables. On optical table 1 the laser light at 729 and 397 nm is generated and sent to optical table 2 via optical fibres. On optical table 2 the vacuum vessel containing the linear ion trap and two diode laser systems, generating the light at 866 and 854 nm, are installed.

The laser light at 397 nm is split into three parts. Two beams are used for Doppler cooling and monitoring of the ions and are denoted Dop1 and Dop2 in Fig. 5.2. These laser beams are overlapped with the light at 866 and 854 nm. For this purpose a glass substrate is used which has a high reflectivity coating for 397 nm on one side and an anti-reflection coating for infrared light around 860 nm on the other side. The third 397 nm beam is used to produce a circularly polarized light beam, denoted as 397σ, for optical pumping of the ions into the $S_{1/2}(m = -1/2)$ state.

To be able to adjust the lasers' wavelengths coarsely close to the atomic resonances, two wavemeters are used with which the wavelengths can be determined with a precision of 10^{-3} to 10^{-4} nm.

5.2.1. 397 nm Laser System

The light at 397 nm is generated by frequency doubling the light from a Ti:Sapphire laser at 794 nm. The Ti:Sapphire laser is pumped by a diode pumped solid state laser system (DPSS)[1] at 532 nm with a power of up to 10 W. The Ti:Sapphire laser is frequency stabilized to a reference cavity using the Pound-Drever-Hall method [81]. To isolate the reference cavity from temperature fluctuations of the environment, it is built into a temperature stabilized vessel. One of the reference cavity's mirrors is mounted on a piezoelectric transducer (PZT). By changing the voltage applied to this PZT, the length and therefore, resonant frequency of the cavity are changed. At the same time the laser's frequency is changed by virtue of the feedback loop. The laser light at 794 nm is coupled into a commercial frequency doubler to generate laser light at 397 nm.

Switching of the 397 nm light is achieved by an acousto-optical modulator (AOM) placed before the fibre which transports the light to optical table 2, where the trap is located. Only light diffracted into the first order is coupled into the fibre. Switching off the RF power of the

---

[1]Coherent Verdi 10 W

Optical Table 1

Ti:Sapphire laser 729 nm

DPSS Laser 2 532 nm

Lock

AOM

Lock

AOM

frequency doubling to 397 nm

Ti:Sapphire laser 793 nm

DPSS Laser 1 532 nm

fibres

AOM

AOM

Addressing optics

729 nm

Lock

diode laser system 866 nm

AOM

397σ

Dop 1

diode laser system 854 nm

Linear Ion Trap

Dop 2

Lock

AOM

Optical Table 2

1/4 wave plate
1/2 wave plate
dichroic mirror
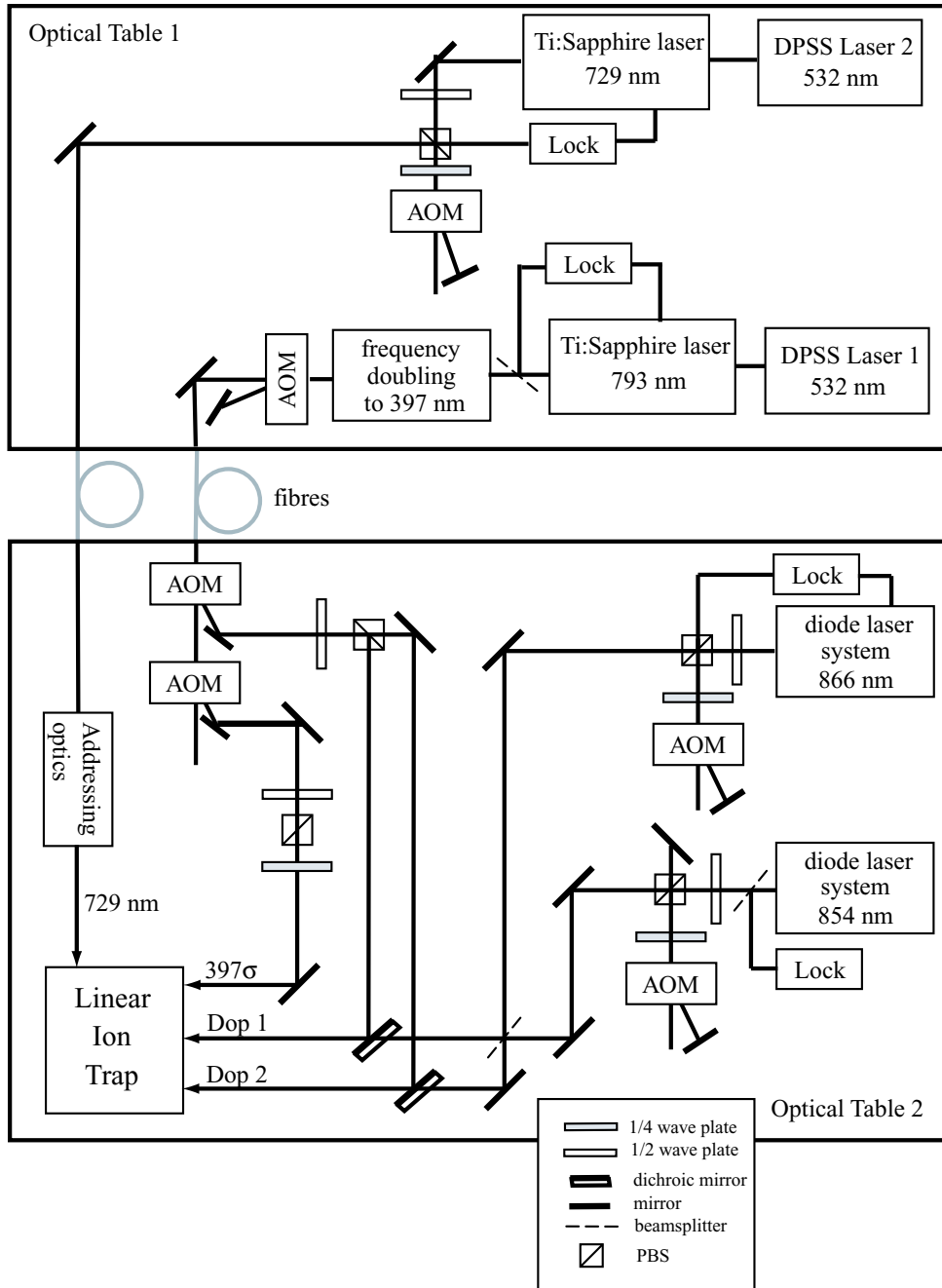mirror
beamsplitter
PBS

Figure 5.2.: Overview of the laser systems and optical setup. The laser systems for 729 nm and 397 nm are installed on optical table 1. This laser light is transferred to the second optical table via optical fibres. On optical table 2 the vacuum vessel containing the ion trap and the diode laser systems at 866 nm and 854 nm are installed.

37

AOM will switch off the light at 397 nm on optical table 2. Additionally by changing the RF power the light power at 397 nm on optical table 2 can be adjusted.

5.2.2. 866 nm and 854 nm Laser Systems

The light at 866 nm and 854 nm is generated by two diode laser systems. A detailed desciption of the design and specifications of these laser systems can be found in [82]. Both diode laser systems are frequency stabilized using optical feedback from a grating and modulation of the laser diode's injection current. Optical resonators are used as frequency references and are placed in temperature stabilized vessels. The diode lasers are locked using the Pound-Drever-Hall method. The frequency of both diode laser systems can be adjusted by changing the RF drive frequency of acousto-optical modulators in a double pass configuration.

5.2.3. 729 nm Laser System

Frequency stabilization

Laser light at 729 nm is generated by a second Ti:Sapphire laser, which is pumped by another DPSS laser system (see Sec. 5.2.1). The 729 nm laser system provides the light for coherent manipulation of our ion qubits. The laser's frequency is required to be highly stable on both long and short time scales. In order to meet this requirement a sophisticated frequency lock of the Ti:Sapphire laser at 729 nm was developed which is thoroughly described in [65]. As a frequency reference a high finesse resonator (F=230000) is used. The resonator is placed in a temperature stabilized vacuum tank to isolate it from thermal fluctuations and acoustic noise. Additionally, the vacuum vessel is placed in a closed box, whose inner temperature is also stabilized. In this way changes in the resonators temperature are minimized, such that the resonator's resonance frequency drift is below 1 Hz/s. The Ti:Sapphire laser is stabilized onto the resonator using the Pound-Drever-Hall method. The feedback circuit has a bandwidth of up to 10 MHz. Slow frequency fluctuations (below 18 kHz) are compensated by adjusting the laser's cavity length, with a PZT which is mounted below one of the cavity mirrors. High frequency fluctuations are compensated for by an electro-optical modulator, which is placed in the laser resonator.

Frequency and phase control

The qubits are manipulated by laser pulses of light at 729 nm. The length and power of these pulses and the frequency and phase of the laser light have to be precisely controlled.

The light at 729 nm passes through an acousto-optical modulator (AOM) in a double pass configuration, such that only light which is first-order diffracted will be coupled into the fibre transporting the light to the ion trap. The frequency and phase of the light are adjusted by changing the AOM's RF drive frequency and phase. Additionally by switching on and off the RF drive power of the AOM, the 729 nm light pulses of well defined length can be produced.

Usually every single run of an experiment takes 20 - 40 ms, including an initial period for Doppler and sideband cooling of about 16 ms, a period containing the pulses for coherent manipulation of the qubit of up to 2 ms and a final period in which the qubit's state is read out. During the second period, sequences of a few tens of 729 nm pulses at the different
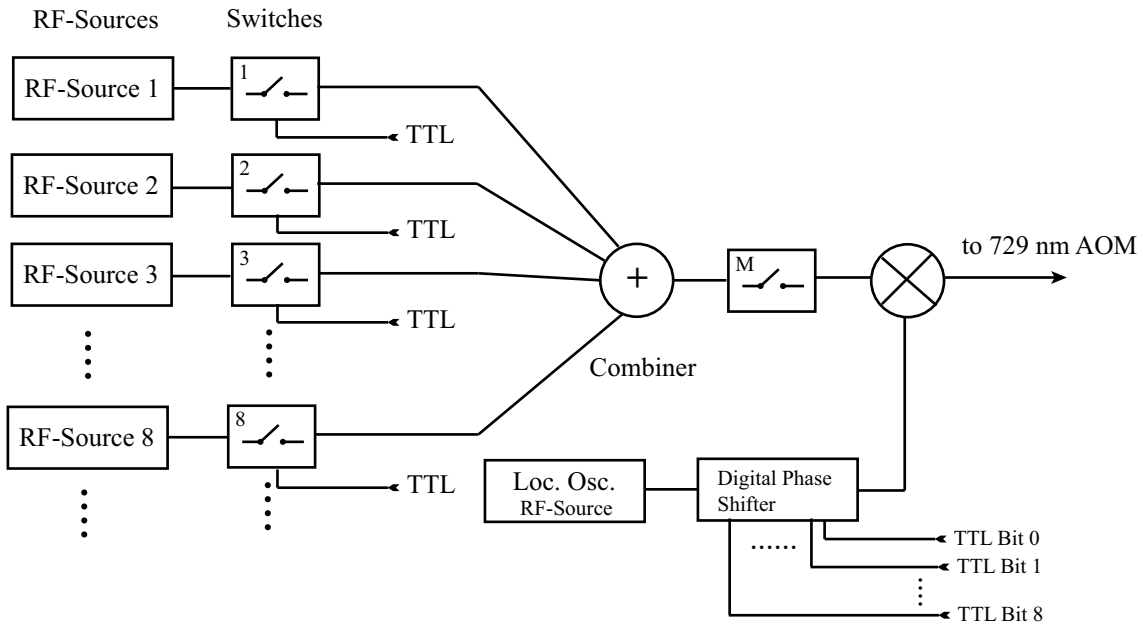
Figure 5.3.: RF network to control phase and frequency of the 729 nm laser light via an acousto optical modulator. For every desired laser frequency one RF synthesizer is necessary. The radiofrequency signal from every RF source can be turned on and off by RF switches, controlled by TTL signals. All signals from the RF sources are mixed with the signal from the local oscillator, to obtain an RF signal around the acousto-optical modulators center frequency of 230 MHz. In the branch of the local oscillator a digital phase shifter is present to control the phase of the radiofrequency sent to the acousto-optical modulator. The RF-synthesizers are all phase locked to the 10 MHz signal from a Rubidium atomic clock.

carrier and sideband frequencies with different power and phases have to be generated, by changing the parameters of AOM's RF drive. This is achieved by the RF-network, whose architecture is shown in Fig. 5.3[2]. For every frequency needed within an experimental run one RF synthesizer[3] is present, which is set to the desired frequency and power. TTL controlled RF-switches are installed at the output of all RF-synthesizers, such that the RF-source driving the AOM can be switched in a time below a microsecond and the length of the 729 nm laser pulses can be controlled by the length of the applied TTL pulses. After the switches the RF signals are combined and sent through another switch, which can be used to mask pulses or whole pulse sequences sent to the other switches.

The actual RF signal which is sent to the AOM is generated by mixing the signal of the RF sources with another RF source which serves as a local oscillator. The advantage of this approach is as follows: The frequency of the 729 nm laser will slowly drift away from the atomic resonance, due to a slow drift of the resonance frequency of the 729 nm laser's reference cavity. Additionally slow changes of the ambient magnetic field will change the atomic resonance frequency via the Zeeman effect. Both effects have to be compensated for by resetting the 729 nm frequency using the AOM. Now, instead of adjusting every single RF source only the frequency of the local oscillator has to be adjusted. Additionally a digital phase shifter is placed after the local oscillator . A phase shift of the radiofrequency signal applied to the acousto-optical modulator will result in an equal phase shift of the first order diffracted laser light passing through the modulator.

Addressing optics

Our approach to ion trap quantum computing relies on the ability to manipulate one qubit within an ion string at a time while leaving all other qubits in the ion string undisturbed. Therefore it is necessary to focus the 729 nm laser beam onto the ions with a spot size smaller than the inter-ion distance. Additionally it must be possible to shift the focus from one ion location to another within a few microseconds.

Recalling the results in Sec. 3.2 the expected inter-ion distance for the usual trap parameters ($\omega_z = 2\pi \cdot 1.2$ MHz) can be calculated to be:

$$N = 2 : \Delta z = 4.96 \ \mu m$$
$$N = 3 : \Delta z = 4.24 \ \mu m$$

To meet these demands the optical setup shown in Fig. 5.2.3 is used. After adjusting the 729 laser beam polarisation by a polarizing beam splitter and half wave plates the beam passes through an electro-optical-deflector (EOD). This element deflects the laser beam dependent on the voltage applied to the device. The voltage applied to the electro optical deflector can be switched within 10 μs in a range of -1000 V to +1000 V. This voltage amplitude results in a shift of the focus at the location of the ion string of $\approx$20-25 μm. In order to align the deflection plane of the EOD with the axis of the ion string, the EOD had to be turned by about 10° with respect to the horizontal plane. The EOD only works properly with light

---

[2]Currently efforts are underway to replace this network by a single device, which can switch between the needed frequencies, phases and power with the necessary time resolution
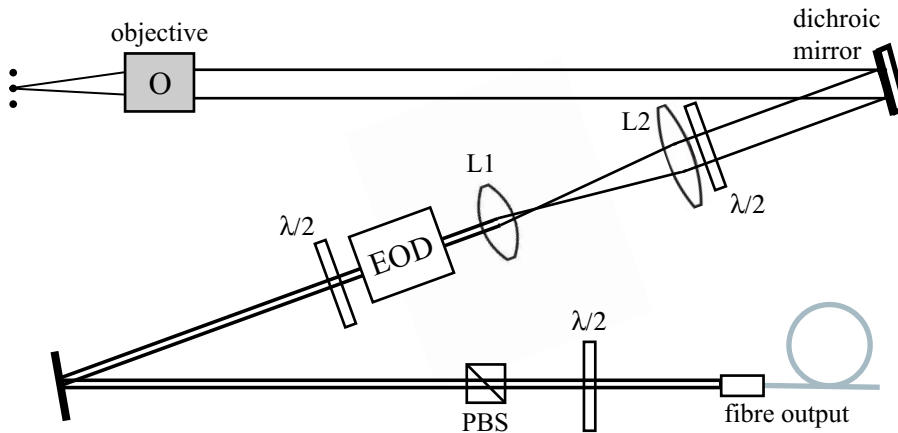[3]Marconi 2023, LFR 2023A

Figure 5.4.: Schematic drawing of the optics for adressing single ions. An electro-optical deflector is used to change the lateral position of the 729 nm focus. To achieve a beam waist on the order of a few micrometers, the 729 nm beam is first expanded by a telescope and then focussed onto the ion string by a microscope objective.

whose polarization is normal to the EOD's deflection plane. Therefore, two additional half wave plates are necessary, to turn the polarization such that it matches to the deflector and to turn the polarization back to the vertical. The beam is expanded using a telescope consisting of a lens L1 (f=25 mm) and a second lens L2 (L=160 mm) and finally focused onto the ions by a commercial microscope objective[4], which has a working distance of 65 mm. The path backwards through the objective is also used to image the fluorescence light of the ions at 397 nm onto the CCD camera. In order to split the light at 729 nm and 397 nm a dichroic mirror is used, which is only highly reflective for the light at 729 nm.

The waist of the focus at the position of the ions has been measured to be $w = 2.50(8)\mu$m. Assuming a Gaussian shape of the beam, one would expect the intensity at the position of the next neighboring ion to be only a fraction of $3.4 \cdot 10^{-4}$ and therefore the Rabi frequency to be a fraction of 1.8%. Measurements of the Rabi frequencies of adjacent ions, where the 729 nm laser beam is focused onto one of the ions, yields a ratio of 2.9 % [68].

5.3. Vacuum Vessel and Optical Access

5.3.1. Vacuum vessel

The vacuum vessel is built up out of a CF 63 double cross with eight extra CF 35 flanges. The linear ion trap is attached to the flange on top of the vacuum vessel. At the bottom, two ovens containing calcium are installed (cf. Sec. 5.4). All vacuum related devices are installed on one arm, to the side of the vessel. Two pumps are installed: a constantly running ion-getter-pump and an titanium sublimation pump, which is turned on from time to time to keep the pressure on the order of $10^{-11} - 10^{-10}$ bar.
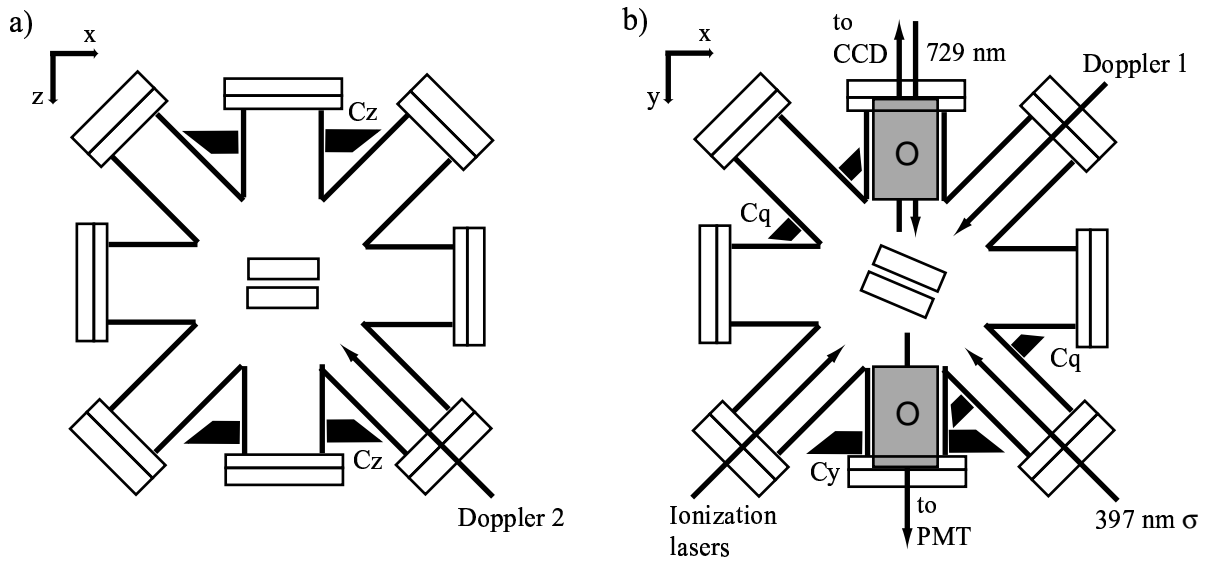
---

[4]Nikon MNH-23150 ED Plan 1.5x

Figure 5.5.: Schematic drawing of the vacuum vessel and the laser beams entering it, a) cross-section of the vacuum vessel in the vertical plane, b) cross-section in the horizontal plane. The grey boxes denoted with O represent the microscope objectives imaging the 729 nm light onto the ions and the fluorescence light onto the PMT. The flanges in which the objectives are built in are inverted viewports, which allows one to place the objectives close enough to the trap. The coils generating the magnetic field are denoted as Cx, Cy and Cz.

5.3.2. Optical access

The geometry of the vacuum vessel can be seen in Fig. 5.5. The trap is located in the center of the vacuum vessel. The trap axis does not coincide with the x-axis given of the vacuum vessel. The reason for this arrangement is the different demands on the coupling of the ions to the light beam at 729 nm, which is coupled in along the vacuum vessel's y-axis. On the one hand it has to be possible to address single ions within an ion chain with this beam, which is easiest when the beam hits the ion chain perpendicularly. On the other hand, for sideband cooling and quantum algorithms, a coupling to the ion's axial sidebands is necessary, which is largest when the 729 nm light beam passes along the trap axis. Therefore, the trap axis deviates from the y-axis of vacuum chamber by an angle of $\alpha = 22.5°$.

As has been noted in the previous section the 729 nm beam is imaged onto the ions by a microscope objective with a working distance of 65 mm. The flanges, in which the objectives are installed, are inverted viewports, which allows one to place the objectives close enough to the trap. On the opposite side of the vacuum vessel another microscope objective is installed which images the ions' fluorescence onto the photo-multiplier-tube.

The so-called Doppler beams Dop1 and Dop2, containing the laser beams at 397 nm, 866 nm and 854 nm, are coupled in through two channels. One Doppler beam lies in the horizontal x-y plane, while the other is coupled in from below and lies in the x-z-plane. Both beams are coupled in through quartz viewports with an antireflection coating for 397 nm. Another two optical channels in the horizontal x-y-plane are used to couple in the light beams with circularly polarized 397 nm σ-beam and the light of the photoionization lasers.

For the experiments treated in this thesis a well-defined magnetic field has to be applied to achieve a splitting of the Zeeman-sublevels of the $S_{1/2} \leftrightarrow D_{5/2}$ transition. Coils are installed which produce magnetic fields along the x,y and z-axis of the vacuum vessel to compensate for the earth's magnetic field. Another pair of coils (Cq) produces a magnetic field of approximately 2.3 Gauss parallel to the σ^+ polarized 397 nm beam, which generates the desired Zeeman splitting.

5.4. Trap loading

In order to load ions into the trap a beam of neutral calcium atoms is used, which is ionized in the trap center. An atomic calcium beam is produced by an oven, which is built into the vacuum vessel. It consists of stainless steel tubes which are heated by an electric current. The atomic beam leaving the oven is collimated by another steel tube with a diameter of 4 mm that is attached to the end of the oven tube. The end of this collimating tube is 15 mm away from the trap center, such that the trap potential is not modified by the presence of the metallic oven. This construction results in an atomic beam of 6 mm diameter and a divergence of 17° at the trap center [68, 83].

Ionization of neutral atoms for loading of an ion trap, is usually done by electron impact. But this method has some serious disadvantages, namely [68]:

- After electron bombardment localized charges remain on the surface of the trap electrodes and surrounding structures, producing stray fields which have to be compensated

Continuum

390 nm

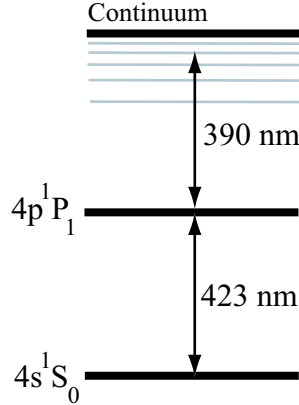$4p^1P_1$

423 nm

$4s^1S_0$

Figure 5.6.: Level scheme of neutral calcium and relevant wavelengths for ionization.

for to avoid micromotion. Because of the slow migration of these charges on a time scale of a few hours, the compensation fields have to be readjusted several times during a day.

- The flux of neutral calcium atoms, necessary to obtain a sufficient loading rate, can result in patches of calcium on the electrode surfaces, which aggravates the problems with unwanted charges deposited on the electrodes and the resulting stray fields.

- Not only neutral ^{40}Ca atoms but also atoms from the background gas or other calcium isotops are ionized using the electron impact method. Therefore impurity ions in the ion strings were frequently observed [63].

These problems were solved by discarding the electron impact method and adopt photoionization for trap loading [84]. Photoionization of calcium is achieved by a process shown in the level scheme in Fig. 5.4. First the calcium atoms are excited from the $4s^1S_0$ ground state to the $4p^1P_1$ with light at 423 nm. Then with light at 390 nm the calcium atoms are excited from the $4p^1P_1$ to Rydberg states near the continuum, where the atoms are field ionized by the electric fields in the trap volume. The light at 423 nm and 390 nm is generated by two diode laser systems. The excitation in the first step of the photoionization is a resonant process and therefore the wavelength of 423 nm laser system has to be tuned to the atomic resonance. We measure the laser's wavelength with a wavemeter and set the wavelength within 1×10^{-3} nm of the atomic resonance. Then the laser wavelength can be set to the $4s^1S_0 \leftrightarrow 4p^1P_1$ transition by using the signal from a hollow-cathode discharge lamp [84].

This photo-ionization process proved to be more than five orders of magnitude more efficient than the electron impact method [68]. The flux of neutral calcium and therefore the risk of producing patches on the electrodes could be reduced. Additionally, the fact that electrons are no longer used for ionization reduced the problem with unwanted stray fields. Another advantage of the photoionization scheme is that the used wavelengths are specific to neutral calcium and therefore other elements from the background gas are not ionized and loaded into the trap. It has been even shown that depending on the exact wavelength of the 423 nm laser the photoionization process is specific to different calcium isotopes [84].

5.5. Detection system

5.5.1. Photomultiplier (PMT)

The photomultiplier tube[5] consists of a bialkali photo cathode which is specified to have a quantum efficiency of 28% at 397 nm. The fluorescence from the ions is collected by a microscope objective, which images the trap center to focal plane 45 cm away from the objective. At this point four adjustable blades serve as an diaphragm to reduce unwanted straylight. Light at wavelengths other than 397 nm has to be suppressed. In particular the light of the 729 nm beam, which directly enters into the PMT channel after passing through the trap center, has to be filtered out. The photo cathode itself has a much lower quantum efficiency for light above 650 nm compared to 397 nm. Additionally the PMT window is covered by Schott glas filters type BG39 and BG3, which suppress light at 729 nm.

In Fig. 5.7 histograms of the photons counted by the PMT for exposure times of (a) 3.5 ms and (b) 300 μs are shown. In both cases only one ion was fluorescing and before the measurement the ion was prepared in a $S_{1/2} - D_{5/2}$ superposition. Two peaks can be seen in the histogram. One peak corresponds to the events where the ion is projected into the S-ground-state and the ion is fluorescing. The other peak corresponds to the cases where the ion is projected into the D-state and the ion doesn't emit fluorescence photons. The residual photons which are detected in this case are due to stray light of the 397 nm laser.

An exposure time of 3.5 ms is usually used to detect the quantum of the ion's at the end of one experimental run. As can be seen in the histogram Fig. 5.7(a) it is possible to detect the state of one ion with virtually 100% certainty. The shorter exposure time of 300 μs was used when a projective measurement of one qubit had to carried out and the result of this measurement was immediately used, i.e. within the coherence time of our qubits, to determine which further operations had to be applied to the qubit register. For this exposure time the state of the ion can be detected with a probability of 99%.

For three ions a typical histogram of the photons counted by our PMT is shown in Fig. 5.8. Three peaks can be seen, which correspond to events where non, one, two or three ions emitted light; therefore the number of fluorescing ions can be determined, however no information about which ions fluoresce is available.

5.5.2. CCD Camera

The second detection device used in our experimental setup is a CCD camera[6]. Fluorescence light emitted by the ions is imaged onto the CCD detector by the same objective used for focussing of the 729 nm beam (cf. Fig. 5.2.3). The CCD camera in our setup is equipped with an image intensifier, which increases the sensitivity of the camera system. The image intensifier consists of three components: a photocathode, a microchannel plate and a fluorescent screen. Photons incindent on the photocathode generate electrons via the photoelectric effect. These electrons enter the microchannel plate (MCP), which is a glass substrate with millions of transverse channels[7]. These channels contain secondary electron emitters on their inner walls,

---

[5]Electron Tubes, PMT type 9111

[6]Roper Scientific IPentaMAX (512x512 FT CCD, Red/Blue GenII Intensifier)

[7]Usually each of these channels has a diameter of 10-12 μm. The spacing between hexagonally arranged channels is about 12 - 15 μm [85]
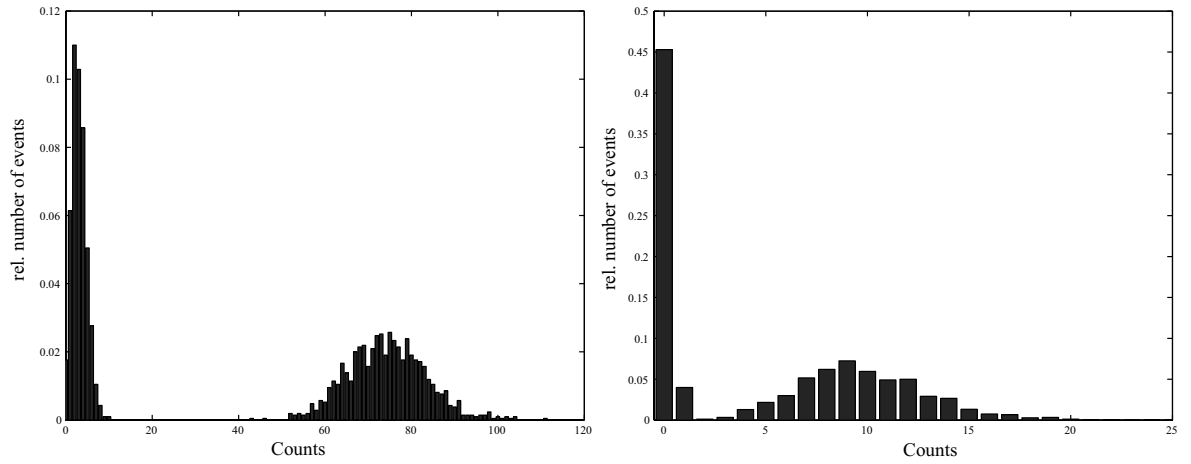
Figure 5.7.: Histograms of the photons counted by the PMT from one fluorescing ion for an exposure of a) 3.5 ms and b) 300 μs.
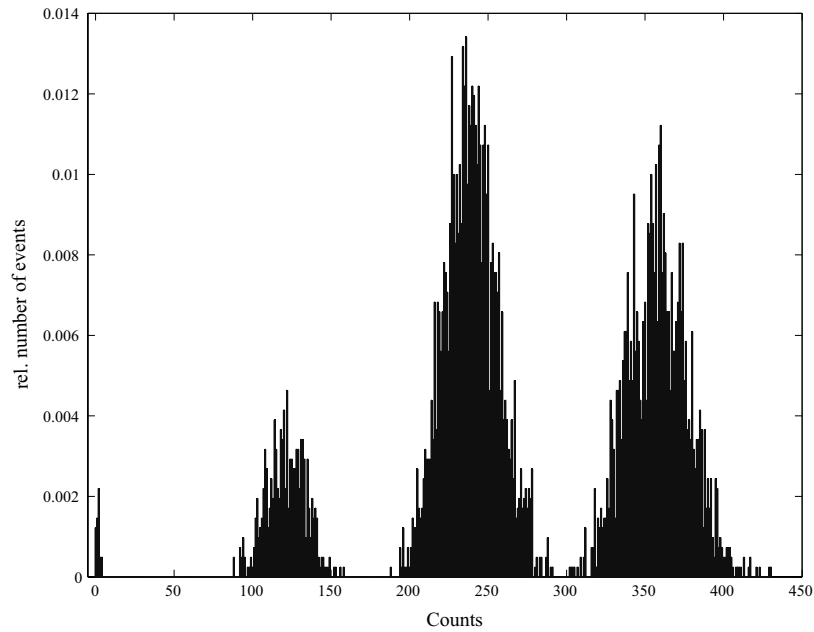

Figure 5.8.: Histogram of the photons counted by the PMT from three fluorescing ions for an exposure time of 3.5 ms. The four peaks correspond to events when no, one, two or three ions emit light.
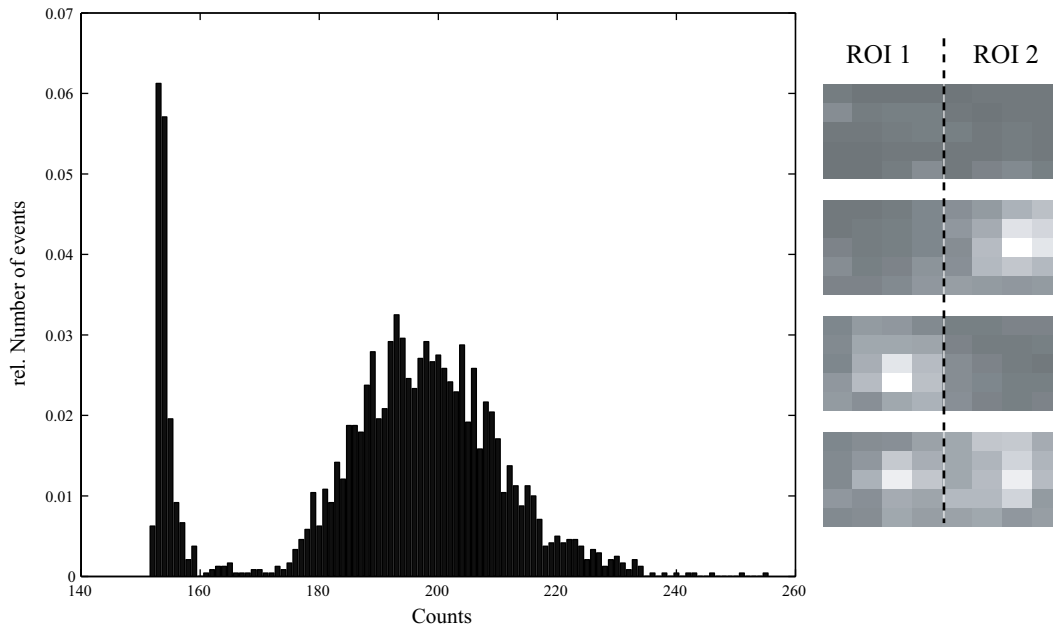
Figure 5.9.: Histogram of the average number of counts within an ROI containing one ion. The CCD cameras exposure time was set to 10 ms.

such that by applying a voltage across the MCP every channel works as a small photomultiplier device. Electrons leaving the MCP are accelerated by a voltage of 5-8 kV before they hit the fluorescent screen and generate photons, which are then detected by the CCD.

It is possible to define areas of pixels around the ion's images on the CCD, the so-called *regions of interest (ROI)*. Then only these small regions, which are usually 5x5 pixels large, are read out and digitized instead of the full array of 512x512 pixels. This way, the time necessary for reading-out the CCD chip and transferring the data to the PC can be decreased to appoximately 30 ms. The average number of counts for every ROI is calculated. In Fig. 5.9 a histogram of this average is shown for an exposure time of 10 ms. Two peaks can be seen corresponding to events where the ion contained in the ROI fluoresces or not. Provided a proper threshold between the two peaks is set, the ion's state can be determined with a probability of 99.3 %.

5. Experimental Setup

6. Experimental techniques and prerequisites

The experiments presented in the following chapters required several experimental techniques and procedures to be properly implemented. The most basic steps of loading ions and adjusting the lasers were already described in the PhD theses of Hanns-Christoph Nägerl [63], Harald Rohde [65] and Christian Roos [64]. In the following we assume that these initial steps have been already completed.

In the following some of the required experimental techniques are briefly reviewed. A more extensive description of these techniques can be found in the PhD thesis of Stefan Gulde [68].

6.1. Spectroscopy on the Qubit transition

Spectroscopic measurements on the qubit transition are made by employing a pulsed scheme. Every experimental cycle, which usually takes 20-40 ms[1], includes all necessary pulses for laser cooling, manipulation of the qubits and the read-out of the ion string. For one data point such a cycle is repeated for 100-200 times in order to determine the probability to find the ions in the D-state P_D, which will sometimes also be denoted as D-state probability or excitation probability. The estimation of the D-state population is subjected to quantum projection noise [86], such that the chosen number of cycles will depend on the allowed order of statistical noise.

A simple example for an experimental cycle is shown in Fig. 6.1. This sequence starts with 2 ms of Doppler cooling by applying 397 nm and 866 nm light. Light at 854 nm is simultaneously applied to return any population left in the $D_{5/2}$ state in the previous cycle to the $S_{1/2}$ ground state. In order to ensure that the ions are prepared in the $m = -1/2$ Zeeman level of the $S_{1/2}$ state, a short pulse of σ^- polarized light is applied, which transfers any population of the $m = +1/2$ Zeeman level to the $m = -1/2$ level.

Next the sequence of 729 nm laser pulses implementing the actual spectroscopic or quantum computational experiment is applied. Finally, the experimental cycle is concluded by applying light at 397 nm and 866 nm in order to measure the state of the ion string (cf. Sec. 4.4.2). The ion's fluorescence is detected with the photo-multiplier tube (PMT) or the CCD-camera. The detection time is set to 3.5 ms, if only the PMT is used, or is set to 10 ms, if the CCD-camera is also employed.

In Figs. 5.7 and 5.9 histograms of the number of photons counted with the PMT and CCD camera, respectively, were shown. Histograms of this kind are used to set a threshold in order to define whether an ion is fluorescing or not. For all cycles taken, the number of counted photons[2] is evaluated, the number of cycles in which the ion was not fluorescing counted and eventually the probability to find the ion in the D-state, P_D, determined.

---

[1]An exception are measurements of the lifetime of certain states, where an experimental cycle can include waiting times of up to a few seconds.

[2]In the case of the CCD camera the average fluorescence within one region of interest is taken (see Sec. 5.5.2)
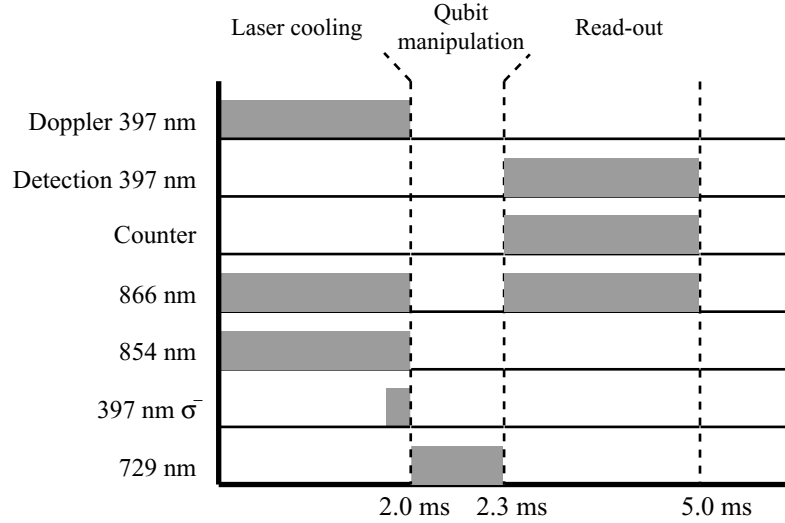
Figure 6.1.: Sequence of laser pulses in one experimental cycle. The grey rectangles indicate the periods, when the respective laser pulses are applied. The vertical dashed lines separate the stages of laser cooling, qubit manipulation and read-out of the ion string.

Evaluating the fluorescence data collected with the PMT for more than one ion is a little more complicated. For example, as can be seen in Fig. 5.8 a histogram for three ions contains four peaks, which correspond to events where three, two, one or none of the ions were fluorescing. In order to discriminate between these cases, thresholds are set in-between those peaks. For every single cycle the number of non-fluorescing ions n^{off} is determined and weighted by the total number of ions, n_{ion}. The excitation probability of the ion string is given by:

$$P_D = \frac{1}{N} \sum_{i=1}^{N} \frac{n_i^{\text{off}}}{n_{\text{ion}}}, \tag{6.1}$$

which becomes one if all ions are excited to the D-state.

Experimental cycles can be synchronized with the 50 Hz power line frequency. This measure minimizes the influence of magnetic field fluctuations, which usually have a 50 Hz periodicity. Therefore, most experiments, especially those presented in the later chapters, are performed with this synchronization, i.e. every cycle will start at the same phase of the 50 Hz power line (cf. Sec. 6.5). Experiments without synchronization are done only if less spectroscopic precision is acceptable and it is desired to acquire data points at a higher rate than the upper bound of 50 Hz for synchronized experiments.

An experiment as shown in Fig. 6.1, containing only a single 729 nm laser pulse, can serve for different kinds of measurements. In Fig. 6.2(a) the frequency of the laser pulse exciting the ions was varied, resulting in an excitation spectrum, containing information about the relative frequencies of the carrier and sideband resonances and therefore the trap frequencies. In Fig. 6.2(b) the frequency of the laser was set to the carrier resonance and the length of the pulse was varied, which results in Rabi oscillations. Such pulse length scans are used to
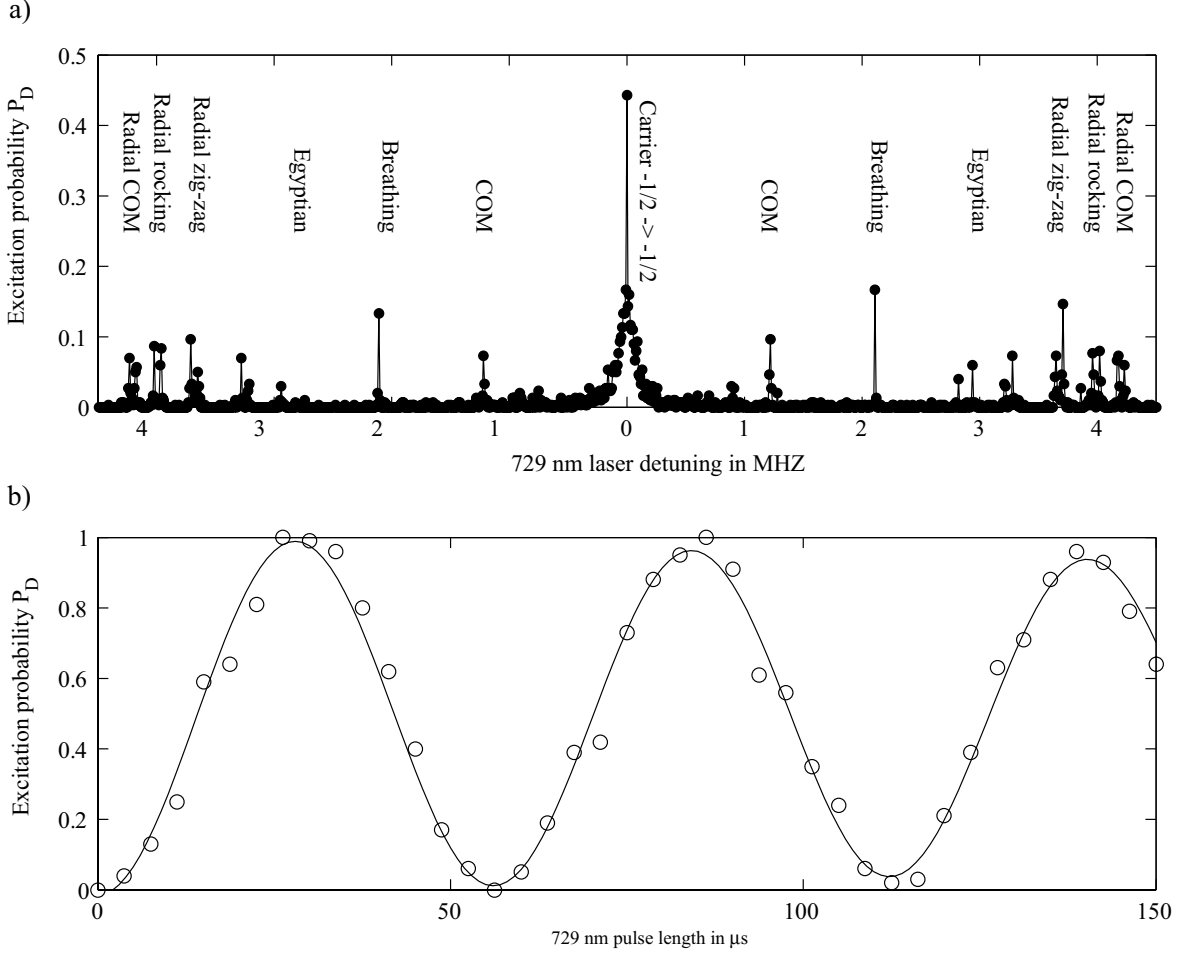
a)

b)

Figure 6.2.: a) Excitation spectrum of a 3-ion-crystal. The central resonance is the carrier of the $S_{1/2}(m = -1/2) \leftrightarrow D_{5/2}(m = -1/2)$ transition. Frequencies are given with respect to the carrier resonance. The axial and radial sidebands of the ion-crystal can be identified. The axial trap frequency is $\omega_{ax} = 2\pi \cdot 1.2$ MHz and the radial trap frequency is $\omega_r = 2\pi \cdot 4.2$ MHz. The radial sideband resonances are split, which is due to the radial oscillation frequencies being non-degenerate. b) Scan of the length of a laser pulse exciting a single ion. The laser frequency was set to the carrier resonance. Rabi oscillations with frequency $\Omega = 2\pi \cdot 18$ kHz are observed.

determine the Rabi frequency and/or the length of laser pulses implementing $\pi/2$-, π- and other rotations in more complex pulse sequences.

6.2. Laser cooling

Slowing down the motion of ions in our experiments via laser cooling techniques is done in order to to:

- crystallize the ions in linear configuration,

- reach the Lamb-Dicke limit,

- cool down one of the vibrational modes to its ground state $|n = 0\rangle$.

The first two goals can be accomplished by using only Doppler cooling, whereas the third goal can in case of our experiment only be accomplished by additional sideband cooling[3] of the respective vibrational mode. We apply each technique in turn to accomplish all these goals.

6.2.1. Doppler cooling

For Doppler cooling, light at 397 nm is used, which is red-detuned approximately half the natural line width of $\Gamma/2 \approx 11.5$ MHz from resonance with the $S_{1/2} \leftrightarrow P_{1/2}$ dipole transition. The lowest temperatures are reached if the intensity of the 397 nm laser is far below the saturation intensity of the dipole transition. This behavior is understandable given that the cooling limit is half the transition's line width, which would be increased by power broadening when using laser intensities above the saturation intensity.

As shown in the experimental cycle in Fig. 6.1 Doppler cooling is applied for 3.5 ms, which is sufficient to keep the ions crystallized in a linear chain configuration and to reach the Lamb-Dicke limit. For radial and axial trap frequencies of $\omega_r = 2\pi \cdot 5$ MHz and $\omega_{ax} = 2\pi \cdot 1$ MHz, respectively, the mean phonon number of the vibrational modes after doppler cooling were found to be $\bar{n}_{\mathrm{ax}} = 15$ for the axial modes and $\bar{n}_{\mathrm{rad}} = 4$ for the radial modes [68].

6.2.2. Sideband cooling

As has been discussed in Sec. 4.5.2, employing sideband transitions in order to implement well-defined quantum operations requires the available vibrational states to be restricted to $|n = 0\rangle$ and $|n = 1\rangle$. First of all this requires the respective vibrational mode to be initialized in $|n = 0\rangle$. In the experiments presented in the following chapters the center-of-mass mode was usually employed. After Doppler cooling this mode has a mean phonon population of $\bar{n} = 15$. The ground state is reached by laser cooling on the $S_{1/2}(m = -1/2) \leftrightarrow D_{5/2}(m = -5/2)$ transition. Since the natural linewidth of this transition is much smaller than the trap frequency, the vibrational sidebands can be resolved in the transition's spectrum, such that we speak of resolved sideband cooling. In Fig. 6.3 the basic laser cooling mechanism is depicted.

---

[3]Whether we speak of Doppler cooling or sideband cooling depends on the relation of the transition's natural linewidth Γ and the vibrational frequency ω. In the weak confinement regime ($\Gamma \gg \omega$) it is common to use the term Doppler cooling , while in the strong confinement limit ($\Gamma < \omega$) the term resolved-sideband cooling is employed [87].
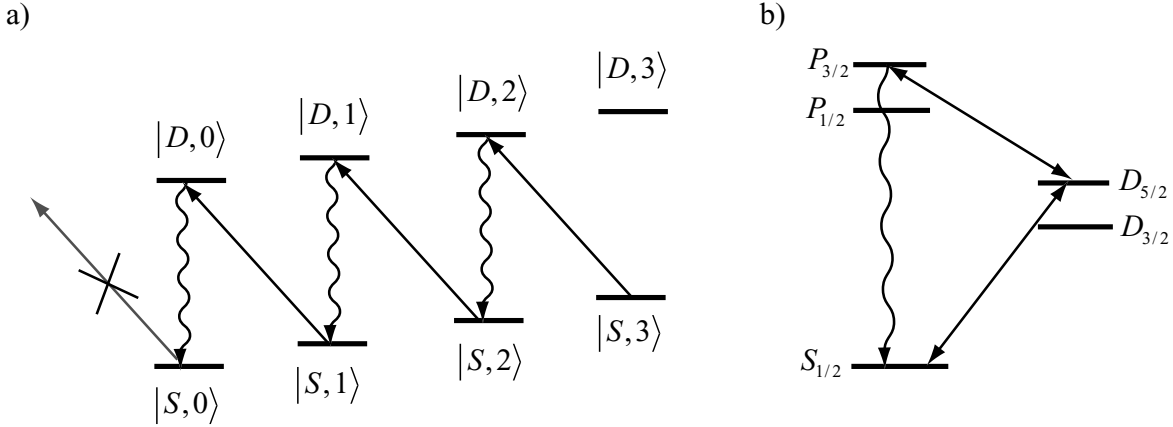
a)

b)

Figure 6.3.: a) Basic principle of sideband cooling. Excitation of an ion on the red sideband of the $S_{1/2}(m = -1/2) \leftrightarrow D_{5/2}(m = -5/2)$ reduces the phonon number by one. Spontaneous decay back into the ground state will most likely happen under conservation of the phonon number. By repeating these excitation-decay cycles the phonon number is stepwise reduced until the ground state is reached and the ions no longer interact with the light field at 729 nm. b) Level scheme of ^{40}Ca$^+$ with the transitions used for sideband cooling. The cooling rate is increased by applying light at 854 nm which depletes the $D_{5/2}$-level.

The laser at 729 nm is tuned to the red sideband of a vibrational mode of the $S_{1/2}(m = -1/2) \leftrightarrow D_{5/2}(m = -5/2)$ transition. An excitation of an ion to the $D_{5/2}(m = -5/2)$ level is accompanied by a decrease of the number of phonons by one. Due to the preceding doppler cooling stage the ion string is in the Lamb-Dicke limit, such that spontaneous emission events from the $D_{5/2}$ level back to the ground state $S_{1/2}$ will most probably happen without a change of the number phonons[4]. Therefore by repeating such a cycle of excitation on the red sideband of the $S_{1/2}(m = -1/2) \leftrightarrow D_{5/2}(m = -5/2)$ transition and subsequent spontaneous decay back into the ground state, the number of phonons can be steadily reduced until the vibrational ground state is reached.

However, due to the natural lifetime of the $D_{5/2}$-level of $\tau \approx 1$ s the cooling rate of this scheme is limited to 1 Hz, which is far to small for practical purposes. Heating processes, that are always present in experiments, will increase the mean phonon number and therefore a large enough cooling rate is necessary to overcome the heating processes[5].

The cooling rate can be increased by applying light at 854 nm, which will transfer a population of the $D_{5/2}$-level to the $P_{3/2}$-level from where spontaneous decay back into the ground state will occur quickly, since this level has only a lifetime of ≈ 7 ns. From the $P_{3/2}$-level the ion can decay with a certain probability into the $S_{1/2}(m = +1/2)$-level and therefore leave the cooling cycle. This probability is already minimized by choosing the transition $S_{1/2}(m = -1/2) \leftrightarrow D_{5/2}(m = -5/2)$ for cooling, such that due to the selection rules a

---

[4]Spontaneous emission events of the kind $|D, n\rangle \rightarrow |S, n+1\rangle$ are suppressed by a factor $\propto \eta^2$ in the Lamb-Dicke limit [87]

[5]In our experiment a heating rate of one phonon per 140 ms was measured [68].

decay back into the m=+1/2 level is most probable. On the average the ions end in the $S_{1/2}(m = +1/2)$ level every 80-160 cycles depending on the polarization setting of the 854 nm laser. Hence, the ions will rarely leave the cooling cycle, since far fewer cycles are necessary to cool the ion string from the initial mean phonon number of $\bar{n} = 15$ to the ground state. A possible population of the $S_{1/2}(m = +1/2)$ level is transferred back to the $S_{1/2}(m = -1/2)$ by applying short pulses of 397 nm σ^- polarized light during sideband cooling.

In Fig. 6.4 an experimental cycle including sideband cooling is shown. Sideband cooling starts immediately after Doppler cooling and is carried out for $\approx$14 ms. The efficiency of
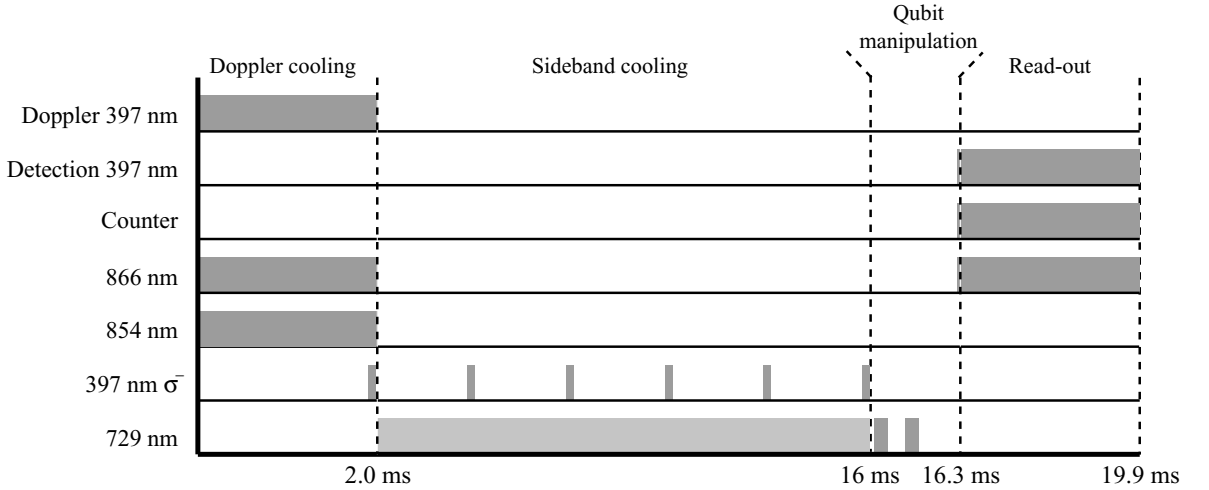

Figure 6.4.: Sequence of laser pulses of an experimental cycle including sideband cooling. After Doppler cooling light at 729 nm tuned to the red sideband of the $S_{1/2}(m = -1/2) \leftrightarrow D_{5/2}(m = -5/2)$ transition is applied. Additionally, short pulses of 397 nm σ^- polarized light are applied to transfer possible populations of the $S_{1/2}(m = +1/2)$ level back to to the $S_{1/2}(m = -1/2)$ level.

ground state sideband cooling can be determined by comparing the height of the red and blue sidebands of the cooled mode. The red sideband is expected to become gradually smaller for decreasing phonon numbers until it completely vanishes when the vibrational ground state is reached. Such measurements were carried out in [68] and found that the vibrational ground state could be reached with probability of 98 % or higher for crystals of one to three ions.

In Sec. 4.3 it was shown that the Rabi frequency of a sideband transition weakly depends on the population of all the other so-called *spectator modes*. A large mean phonon number $\bar{n}$ in those modes will be accompanied by a large variance of the actual phonon population, which scales with $\sim \sqrt{\bar{n}}$, from one experimental cycle to the next. The corresponding slight variation of the sideband Rabi frequency would deteriorate our experimental results. In our experiments this effect is expected to play a role in case of the axial spectator modes, which have a comparably large mean phonon population after Doppler cooling. Therefore, not only the axial mode which is chosen as "bus mode" is subjected to sideband cooling but also the next neighboring axial mode. The radial modes have a much lower mean phonon number of $\bar{n} = 4$ after Doppler cooling, which is due to the higher frequencies of these modes. These populations
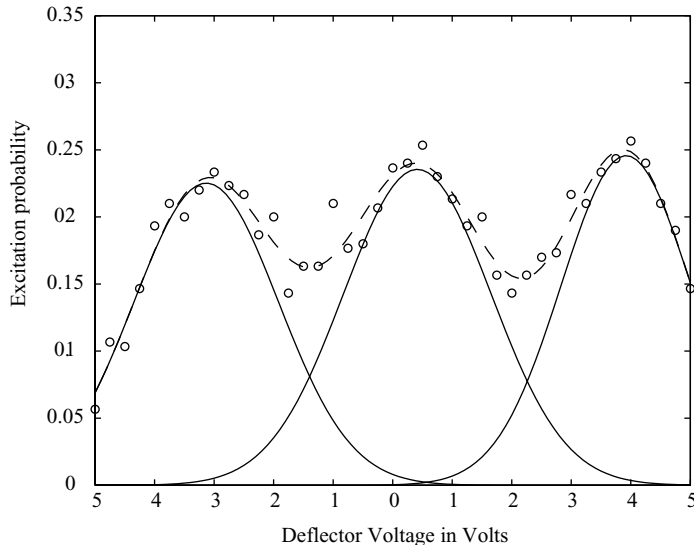
Figure 6.5.: Scan of the voltage applied to the electro-optical deflector, such that the position of the focus of the 729 nm laser beam is scanned across an crystal of three ions. The probability P_D of the ions to be excited to the $D_{5/2}$ shows three maxima, corresponding to the focus being centered on each one of the ions in turn. The excitation probability was fitted with a function describing three overlapping Gaussian profiles. The dashed line indicates the result of this fit, while the solid line shows the individual Gaussian profiles.

have a negligible effect on the sideband Rabi frequencies [68], such that no additional efforts to cool these modes have been undertaken so far.

6.3. Addressing of individual qubits

Addressing of a single ion within a crystal of several ions with 729 nm laser pulses and switching between ions in a string is achieved with the optical setup shown in Sec. 5.2.3. Properly adjusting this setup is indeed often the most time consuming task when preparing the experimental setup for more sophisticated experiments. The critical parameter used to quantify the performance of the addressing optics is the ratio of the Rabi frequency on the neighboring ions to the Rabi frequency on the addressed ion, the so-called *addressing error*. With our optical setup addressing errors of 2.5-5 % are feasible, if the setup is properly adjusted. Addressing errors larger than ≈ 5 % would already significantly affect the performance of pulse sequences applied to the ion string.

The optical setup is adjusted for optimal performance as follows: Using an experimental sequence like that shown in Fig. 6.1 which contains only a single 729 nm pulse the excitation probability is probed. The position of the second lens L2 in the telescope optics can be adjusted in all three dimensions. The lateral and horizontal position of this lens is adjusted until the excitation probability is maximized. Then an experimental sequence is chosen in

which a single 729 nm laser pulse of length $\theta = \pi/6$ excites the ions. The voltage applied to the electro-optical deflector is scanned and the excitation probability measured. A typical result of such a scan for a three ion crystal is shown in Fig. 6.5. Three peaks of the excitation probability can be seen, which correspond to the voltages, where the laser beam is centered on one of the three ions. These voltages will be denoted as $U_{\mathrm{def}}^{\mathrm{ion\#}}$ in the following. Later, the deflector voltage will be set to $U_{\mathrm{def}}^{\mathrm{ion\#}}$ when laser pulses should be applied to the respective ion. The pattern of peaks is adjusted, such that they are centered around U=0 V deflector voltage, by adjusting the horizontal position of lens L2.

In order to measure the addressing error Rabi oscillations for all $U_{\mathrm{defl}}^{\mathrm{ion\#}}$ are recorded. Typical results of such a measurement in the case of a three ion crystal are shown in Fig. 6.6. These pulse-length scans show fast Rabi oscillations, which are superimposed on a slower Rabi oscillation, stemming from the excitation of the next neighboring ions. The period of these Rabi oscillations can be fitted and the addressing error calculated. For the data shown in Fig. 6.6 the addressing error is determined to be on the order of 2-3 % for the outer ions number 1 and number 3. As can already be seen from Fig. 6.6 the center ion number 2 is stronger affected by imperfect addressing. Both of its neighboring ions are excited and contribute to the addressing error, which was determined to be 6%.

This cycle of adjusting the optical setup, determining the deflector voltages corresponding to the ion positions and then measuring the addressing error is repeated until the addressing error is sufficiently small. The following strategies turned out to be suitable in order to reduce the addressing error: First of all it should be ensured that the 729 nm laser beam is passing as well a possible through the center of all optical elements in order to reduce optical abberations. This especially applies to the electro-optical deflector, the telescope lenses and the microscope objective. The main handle for optimizing the performance is the second telescope lens L2, which is mounted on a three-axis translation stage. By adjusting the position of this lens along the axis given by the beam path, the position of the focus plane in the trap can be shifted. This plane should ideally coincide with the axis of the ion string.

The vertical position of lens L2 has turned out to be a critical parameter, since even the smallest misalignment of the vertical position of the laser beam with respect to the ions increases the addressing error noticeably[6]. Another measure, which was frequently successful in reducing the addressing error, was to displace the laser beam in the horizontal or vertical direction. This can be done by deliberately misaligning the laser beam with lens L2 and then realigning it with the dichroic mirror. The ions themselves can serve as points of reference in this procedure. For instance, suppose that a deflector voltage is chosen, such that the center ion is addressed. Using lens L2 the focus is shifted until a neighboring ion is addressed. Then the focus is shifted back to the center ion by adjusting the dichroic mirror.

During these adjustments the ions are usually excited with a pulse of length $\pi/2$ and the excitation probability is monitored. Centering the focus of the laser beam on one of the ions corresponds to maximizing the excitation probability or, more precisely, increasing the Rabi frequency. However, sometimes a more useful method is to set the pulse length to 2π or 4π. For perfect addressing the excitation probability would be zero for these pulse lengths.

---

[6]This large sensitivity of the addressing error to misalignment of the laser beam in the vertical direction is unfortunate given the fact that the vertical position of the whole ion trap slowly changes due to thermal expansion, whenever the applied RF-power is reduced in order to recrystalize the ions.
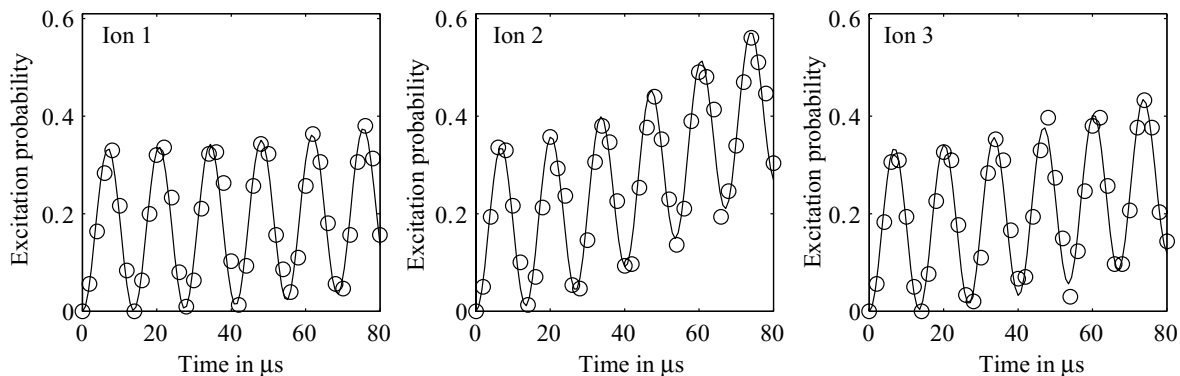
Figure 6.6.: Scan of the pulse length for the 729 nm laser beam being directed to one of the ions of a three ion crystal. The excitation probability, i.e the probability to find the ions in the $D_{5/2}$ state, was determined using the PMT. Rabi oscillations with a frequency of $\approx 2\pi \cdot 75$ kHz are observed. These Rabi oscillations are superimposed by a slower oscillation, due to excitation of the next neighbouring ions. By determining the Rabi frequency of these oscillations the addressing error was determined to be about 2-3 % for the outer ions 1 and 3 and 6 % for the center ion 2. The center ion is more affected by imperfect addressing, since both of its neighboring ions are excited.

However, due to excitation of the neighboring ions the excitation probability is non-zero, as can be seen in Fig. 6.6. Therefore, measuring the excitation probability at these pulse lengths allows to monitor a quantity, which is directly related to the addressing error. This method is for example useful for adjusting the vertical and horizontal position of the electro-optical deflector. The crystal through which the laser beam has to pass, has only a diameter of a few millimeters. If the laser beam is not passing through the center of this crystal or is even clipped by it, abberations and therefore an increased addressing error are the result. Instead of adjusting the laser beam, the electro-optical deflector's vertical and horizontal position can be changed by a translation stage. The optimal position causing the least aberrations can be determined by the method outlined above, i.e. minimizing the excitation probability for a pulse length of 2π.

6.4. Compensation of Light Shifts

In Sec. 4.6.2 the frequency shift of two atomic levels due to a non-resonant light field was discussed. In this section light shifts of the levels $S_{1/2}$ and $D_{5/2}$, which make up our qubit, will be treated. First the consequences of light shifts in context of quantum algorithms will be discussed. Then measurements of the light shift induced by an off-resonant laser pulse are presented. Finally a technique in order to compensate light shifts induced by laser pulses exciting the sideband transitions is introduced.

6.4.1. Negative effects of Light shifts on Quantum Algorithms

Quantum algorithms will consist of a sequence of laser pulses being resonant with the carrier transition or one of the sidebands of the $S_{1/2} \leftrightarrow D_{5/2}$ transition. The exact length and phase of these pulses has to be well defined in order to properly implement the desired unitary operation. In general, the action of quantum algorithms on a register of qubits can be seen as a many-particle quantum interference experiment. The outcome of such an interference experiment will critically depend on the relative phases of the interfering quantum states. Unwanted or even uncontrollable phase shifts would severely affect the performance of quantum algorithms.

We have to be solely concerned with light shifts induced by sideband transitions. A laser pulse resonant with the carrier transition will in itself not shift the carrier transition. Sideband transitions are however usually driven with high intensities in order to achieve decent Rabi frequencies despite of the low coupling constant. Non-resonant coupling to the nearby strong carrier transition is inevitable, which will shift the resonance frequency of the sideband transition. In addition, the change in resonance frequency of the $S_{1/2} - D_{5/2}$ transition will act like a rotation around the z-axis in the Bloch sphere picture, i.e. the relative phase of an superposition of $|S\rangle$ and $|D\rangle$ would be changed. In principle one could think of cancelling these effects by adjusting the frequency of the sideband pulses and the phase of the following laser pulses. But apart from complicating the proper implementation of an algorithm this approach is limited by the fact that the intensity of our 729 nm laser is fluctuating on the order of $\approx 5\%$. The resulting fluctuating light shift will affect experiments in two ways: First, the resonance frequency of the sideband transition will fluctuate, acting like an additional line broadening, which will harm our efforts to apply well defined sideband operations. And second, the phase shift induced on possible atomic superpositions will vary statistically, acting as an additional source of phase noise, which would limit our coherence time. Therefore, a more promising strategy is to cancel the occurring light shifts on the sideband transition.

6.4.2. Measurement of Light Shifts

Measuring a light shift caused by a non-resonant laser pulse is possible by making use of the phase shift induced on an atomic superposition. Such a phase shift can be determined by a Ramsey interference experiment [88]. In Fig. 6.7(a) the basic setup of a Ramsey experiment is shown. An initial $\pi/2$-carrier laser pulse applied to a single trapped ion is generating a $(|S\rangle + i|D\rangle)/\sqrt{2}$ superposition and after a certain waiting time a second $\pi/2$-pulse is applied. Provided, that no relative phase shift between the phase of the laser and the phase of the atomic superposition is induced, the second laser pulse will transfer the ion to the $|D\rangle$-state resulting in an excitation probability of one. In Fig. 6.7(b) a non-resonant laser pulse of length τ is applied within the two Ramsey pulses. This pulse will induce a phase shift $\delta\phi$, such that the second $\pi/2$ pulse will no longer transfer the ion to the $|D\rangle$-state. This can be clearly seen in the Bloch sphere pictures, bearing in mind that the phase shift induced by the Stark effect acts like a rotation around the z-axis and that the Ramsey carrier pulses are assumed to act like $\pi/2$-rotations around the x-axis. By varying the length τ of the non-resonant laser pulse and measuring the $D_{5/2}$ excitation probability after the second Ramsey pulse an oscillation is obtained, as can be seen in Fig. 6.7(c), whose frequency directly provides the light shift δ_{ac}.
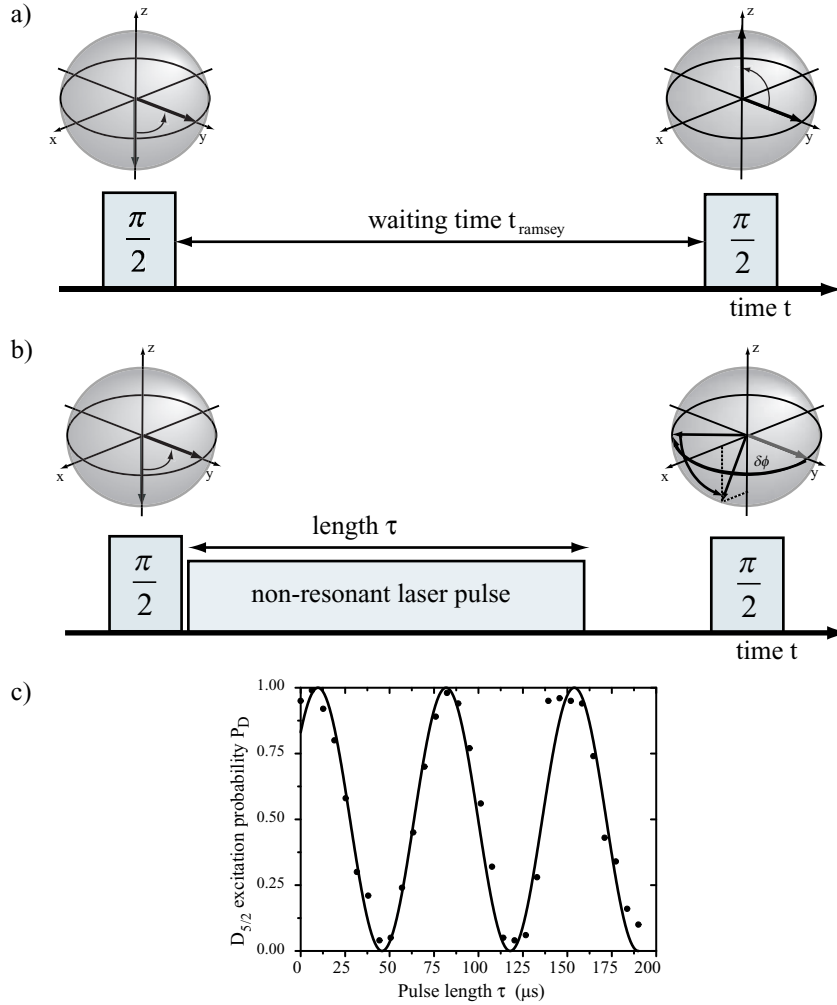
Figure 6.7.: a) Setup of a Ramsey interference experiment consisting of two $\pi/2$-carrier pulses applied to a single trapped ion separated by a waiting time τ_{ramsey}. With no additional phase-shift the second laser pulse will transfer the ion to the $D_{5/2}$-state. b) Ramsey experiment with a non-resonant laser pulse inducing a light shift δ_{ac} applied in between of the Ramsey pulses. The induced phase-shift $\delta\phi$ will change the outcome of the Ramsey experiment. The action of the pulse sequences in a) and b) is also depicted in the Bloch sphere picture. In b) the consequence of the additional phase-shift and the second Ramsey-pulse on the Bloch vector can be clearly seen. c) Measurement of the dependence of the $D_{5/2}$ excitation probability on the length of the non-resonant laser pulse. The frequency of the observed oscillation and therefore the ac-Stark shift is given by $\delta_{ac} = 2\pi \cdot 13.9(0.2)$ kHz.
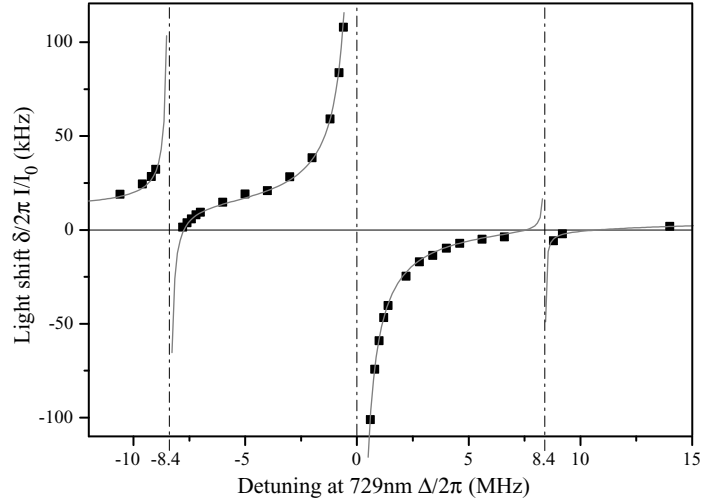
Figure 6.8.: Measured light shift induced by a non-resonant 729 nm laser pulse as a function of the detuning Δ of the light shift pulse. The measured data of the shift δ_{ac} is normalized according to the measured laser power $I(\Delta)/I(0)$, which varies by about 50 % over the whole tuning range of Δ. The divergencies are due to the carrier resonances of the Zeeman levels $(m = -1/2) \leftrightarrow (m' = -5/2, -1/2, +3/2)$. The lines indicated shows the expected theoretical behavior of the light shift [[89]]

In Fig. 6.8 such a measurement of the light shift for different frequencies of the Stark pulse are shown. There are two major contributions to the Stark-shift: The largest contribution is due to the coupling to the three Zeeman carrier transitions $(m = -1/2) \leftrightarrow (m' = -5/2, -1/2, +3/2)$. The second largest contribution is the non-resonant coupling to the dipole transitions $S_{1/2} \leftrightarrow P_{1/2}$ and $D_{5/2} \leftrightarrow P_{3/2}$, which are far off-resonant but add a measurable contribution due to their large line strength. A third kind of contributing transitions are sideband resonances of the $S_{1/2} \leftrightarrow D_{5/2}$ transition, which have a small coupling strength and therefore can be neglected. Taking into account the major contributions measured Stark-shift data can be well described, as the fitted curve in Fig. 6.8 shows[7].

6.4.3. Compensation of light shifts

In experiments we will most often use blue sideband transitions belonging to the center-of mass mode at a detuning $\Delta = +2\pi \cdot 1.2$ MHz or in few cases the breathing mode at a detuning of $\Delta = +2\pi \cdot 2.1$ MHz. In Fig. 6.8 it can be seen, that the light shifts at these detunings will be negative. In order to cancel out the light shift induced by laser pulses on the blue sideband a second light field is applied, which induces the exact opposite positive light shift. That this scheme actually works can be proven with the experimental sequence shown in 6.9(a), where again a Ramsey-interference experiment is used to detect any occurring phase shift induced by the pulses during the waiting time τ_{ramsey}. The blue sideband laser pulse is actually a few ten kHz detuned from resonance to avoid population transfer to the D-state, its induced

---

[7]For more details see references [68] and [89].

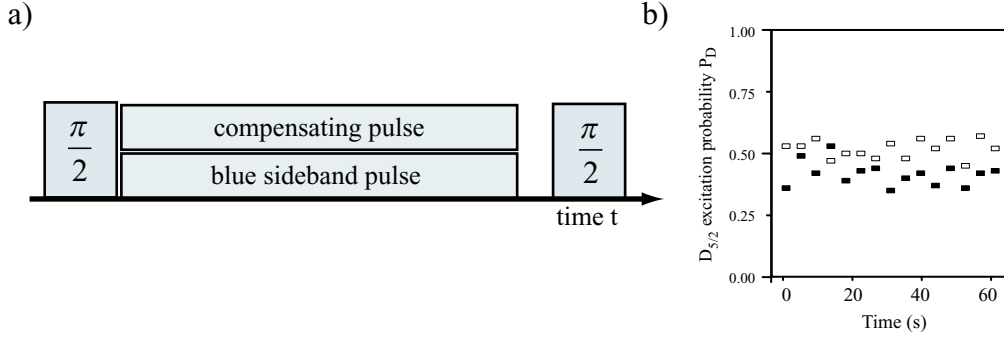a)   b)

Figure 6.9.: a) Sequence of an experiment to adjust the parameters of the compensating laser. A Ramsey experiment measures residual light shifts induced by the pulses during the Ramsey interrogation time. b) Results of alternatively taken experiments with no sideband and compensation pulse (solid dots) and experiments with those pulses switched on for $\tau = 200\mu$s (open dots). The relative phase of the Ramsey pulses is adjusted to $\pi/2$, such that P_D is close to 0.5. The residual light shift is estimated to be $\delta_{\mathrm{ac}} = 2\pi \cdot 0.25(3)$ kHz [89]

light shift will however remain practically identical. Simultaneously a non-resonant laser pulse of equal length is applied, whose frequency and intensity should be adjusted, such that the exact opposite light shift of the sideband pulse is induced. The proper parameters of the compensation pulse are found, if no longer an oscillation of the Ramsey signal is observed, when varying the length of the simultaneous sideband and compensation pulse. However, the accuracy with which the light shift can be nulled using this method is limited by the drift of the Ramsey pulses' frequency, which results in a drift of the relative phase of the Ramsey pulses, mimicking a residual light shift [89]. Hence, the parameters of the compensation laser were set by alternating Ramsey experiments without sideband and compensation pulses and experiments with those pulses switched on for a time $\tau = 200\mu$s, which should deliver the same result provided no residual light shift is present. This way light shifts due to imperfect compensation can be discriminated against the effect of a slow drift of the laser's frequency. In Fig. 6.9(b) data points of such alternating Ramsey experiments are shown.

The laser light driving the sideband transition and the simultaneously applied light for compensation of light shifts are obtained from the same 729 nm laser system, where the necessary bichromatic light field is generated by feeding two RF-signals with different frequencies and intensities to the acousto-optical modulator controlling the frequency of the laser light. This has the advantage that drifts or fluctuations will affect both light fields in the same way, such that the light shift compensation is unaffected. The frequency of the compensating light field has to be chosen, such that unwanted off-resonant excitations are avoided. In the results shown in 6.9(b) the frequency of the compensating laser light was set to $\Delta = 2\pi \cdot 800$ kHz detuned to the red from the $S_{1/2}(m = -1/2) \leftrightarrow D_{5/2}(m = -5/2)$ transition. However, in all the experiments presented in this thesis an even larger detuning of usually $\Delta = 30$ MHz was chosen. At such a large detuning the main contribution to the compensating light shift stems from coupling to the far detuned dipole transitions, which is only weakly depending on the

exact value of the detuning.

The method to find the proper parameters of the compensating laser described above was found to be too time consuming, since a parameter-set has to be checked for different pulse lengths to avoid adjusting the phase shift accidentally to a multiple of 2π rather than 0π. Therefore the following procedure for setting the compensating laser was adapted: Excitation spectra are taken in order to precisely determine the frequency of the blue sideband resonance. These spectra are taken using laser pulses, whose intensity are set 1-2 orders of magnitude smaller than the intensities for later qubit manipulations. Due to the small intensities light shifts can be neglected and thus the unshifted resonance frequency of the blue sideband is obtained. In another experiment a blue sideband pulse of length $\approx \pi/2$ is applied, set to the unshifted blue sideband frequency and set to the intensity chosen for later quantum manipulation. Simultaneously the compensating laser light is applied. Proper compensation of the light shift induced by the sideband pulse, will keep the blue sideband resonance at its unshifted frequency and will therefore maximize the excitation probability of the sideband pulse. Therefore, in order to find the right intensity of the compensating laser, its intensity is varied and the excitation probability P_D maximized.

6.5. Coherence of single qubits

Our experiments rely on our ability to store quantum information in superpositions of the $S_{1/2}$ ground state and the $D_{5/2}$ metastable state, which make up our qubits. Now the crucial question is: Assuming that we prepare a qubit in a superposition $|\Psi\rangle = \alpha|S\rangle + \beta|1\rangle$, after how much time are we still able to manipulate the stored quantum information in a well defined manner ? Or more technically speaking: After which time span the initial coherently prepared pure state will have decayed into an incoherent mixture, reflecting our ignorance about the qubit's exact state ? This time span is usually denoted as the *coherence time of a single qubit*. Even though, due to this definition it seems that the coherence time is an attribute of the qubit itself, one should bear in mind that it is a measure of the relative stability of the qubit and the tools with which the qubit is manipulated, i.e in our experiment our 729 nm laser system.

A fundamental physical limit of the coherence time is given by the lifetime of the metastable $D_{5/2}$ state. This lifetime was recently measured by A. Kreuter et al. to be 1162(22) ms [90]. This fundamental limit will however play no role for the single qubit coherence time in our experiments. The major source of decoherence rather are technical imperfections of our experimental setup, as there are:

- frequency noise of the laser light driving the qubit transition,

- fluctuations of the ambient magnetic field resulting in a fluctuating shift of the qubit's energy levels via the Zeeman effect.

These noise sources will cause fluctuations of the relative phase ϕ of a qubit superposition $|\alpha||S\rangle + |\beta|e^{i\phi}|D\rangle$. In the following a few experiments are presented, which investigate these sources of decoherence. An extensive discussion of decoherence sources in our experiment, including most of the experiments presented here, can be found in Ref. [91].
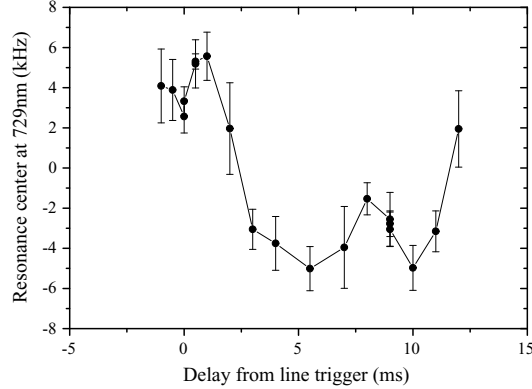
Figure 6.10.: Resonance frequency of the $S_{1/2}(m = -1/2) \leftrightarrow D_{5/2}(m = -5/2)$ transition depending on the delay between the exciting laser pulse and the trigger derived from the 50 Hz power line frequency. Due to 50 Hz fluctuations of the ambient magnetic field the resonance frequency is shifted. The vertical bars indicate the width of the observed resonances and not the error of its center frequency.

6.5.1. Noise components at 50 Hz

The noise spectrum of the ambient magnetic field is expected to have a large component at the power line frequency of 50 Hz, which is caused by transformers, pumps, motors etc. in the various electric devices present in the vicinity of our experimental setup. In order to reduce the influence of 50 Hz noise, experimental cycles are triggered synchronized with the 50 Hz frequency from the power line.

The variation of the magnetic field can be determined by shifting the trigger with respect to the line frequency and measuring the resonance frequency of the $S_{1/2}(m = -1/2) \leftrightarrow D_{5/2}(m = -5/2)$ transition. The resonance frequency of the $m = -1/2 \rightarrow -5/2$ Zeeman component was determined by recording excitation spectra, which were taken by measuring the D-state excitation probability after a 1 ms laser pulse at 729 nm. From the results shown in Fig. 6.10 a variation of the resonance frequency of $\simeq \pm 5$ kHz is inferred, which corresponds to a variation of the magnetic field of ≈ 1 mG. The width of the recorded resonances, indicated by the vertical bars in Fig. 6.10, also varies depending on the chosen delay indicating different magnitudes of higher frequency fluctuations of the magnetic field during the 1 ms long excitation pulse. It would be favorable to choose a delay, where the linewidth and therefore magnetic field fluctuations are minimal. However, it was found that the features of the results of a measurements like in Fig. 6.10 are not constant but change on a time scale of days or weeks.

6.5.2. Active Compensation of ambient magnetic-field fluctuations

A commercial active magnetic-field compensation system[8] was installed in order to improve the ambient magnetic field stability. This system is measuring the magnetic field with two

---

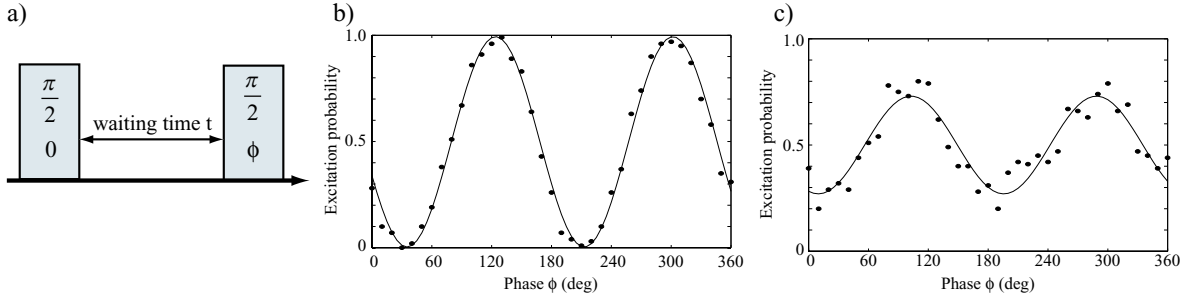[8]FCS-12 Field Cancelling System, Oxford Instruments

a)

Figure 6.11.: a) Pulse sequence of a Ramsey experiment. The second $\pi/2$-pulse is applied with phase ϕ. b) Excitation probability after Ramsey experiment depending on the phase ϕ. Interference fringes with nearly unity contrast are observed. c) Again Ramsey interference fringes for a longer waiting time t. Due to dephasing of the atomic superposition the contrast of the fringes is decreased. Data shown in b) and c) belong to Spinecho-Ramsey experiments shown Fig. 6.12 for t= 1ms and t= 3.5 ms, respectively.

flux-gate sensors, which are positioned in direct vicinity of the vacuum vessel. A compensating magnetic field is generated by three orthogonal coils. The system is specified to compensate magnetic field fluctuations in the frequency range of 0.5 Hz to 5 kHz. Indeed using an independent flux-gate sensor it was found that the $\simeq 1$ mG field fluctuations at 50 Hz are reduced by factor of $\simeq 20$. This reduction of 50 Hz noise was also proven with trapped Ca^+ ions, by recording the shift of the resonance frequency of a Raman transition dependent on the line trigger delay [91].

6.5.3. Ramsey-Spectroscopy

Due to the decoherence mechanisms present in our experimental setup a qubit prepared in a coherent superpositions will dephase into an incoherent mixture. This decay can be measured using a Ramsey-interference experiments, which were introduced in Sec. 6.4.2. The basic setup of an Ramsey experiment is again shown in Fig. 6.11(a). If the phase of the second Ramsey pulse ϕ is varied, which corresponds in the Bloch sphere picture to a variation of the chosen rotation axis in the equatorial plane, the D-state excitation probability will vary periodically, as can be seen in Fig. 6.11(b). Provided that after the waiting time the relative phase of the atomic superposition generated by the first Ramsey pulse is still well defined, the observed oscillation will show a contrast of one. However, if the atomic superposition is decayed into a mixed state after the waiting time t the contrast of the Ramsey fringes will be decreased, as can be seen in Fig. 6.11(c) where Ramsey fringes for a long waiting time are shown[9] The result of a series of Ramsey experiments for different waiting times t are shown in Fig. 6.12. For an increasing waiting time t the contrast is decreasing, indicating the loss of phase coherence of the atomic superposition. Data sets were taken with (open dots) and

---

[9]It is important to note, that we determine the excitation probability by repeating Ramsey experiments for one value of ϕ for 100 times.
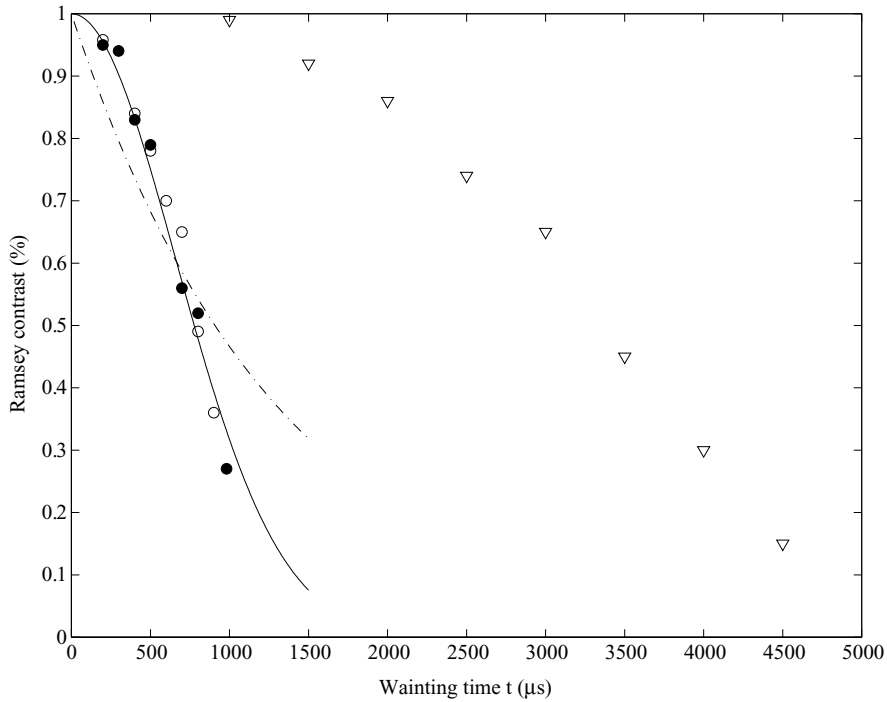
Figure 6.12.: Contrast of Ramsey interference fringes depending on the waiting time t. Results of Ramsey experiments with (open dots) and without magnetic-field stabilization (black dots). A fit with a Gaussian $\propto \exp(-(t/t_0)^2)$ yields a coherence time of $t_0 = 0.94(5)$ ms. The dashed line shows an optimal exponential fit $\propto exp(-t/t_0)$, which is the expected dependence for a white noise model. Furthermore, results of Ramsey experiments including a spin-echo pulse are shown (triangles). The spin-echo technique is eliminating the effect of slow drifts of the atomic phase. A coherence time of > 3.5 ms is observed.
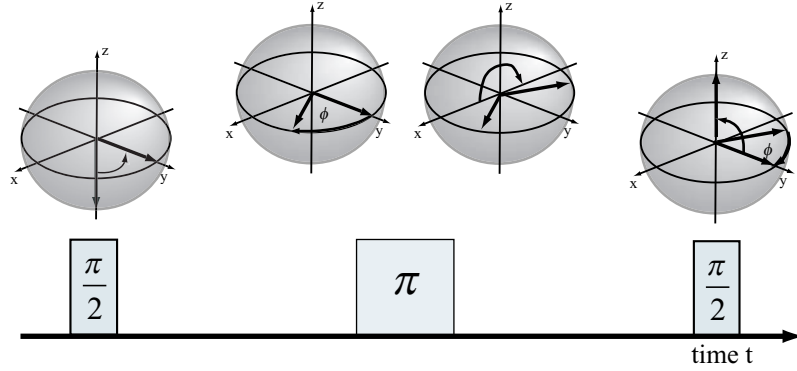
Figure 6.13.: Ramsey interference experiment including a π pulse in the center implementing a spin-echo. The action of the pulse sequence is illustrated using the bloch sphere picture, where a constant drift of the atomic phase is assumed.

without (black dots) the active magnetic-field stabilization. No influence of the magnetic-field stabilization on the coherence time can be observed, which is assumed to be due to the limited bandwidth of the magnetic-field stabilization device. Assuming a white noise model of the frequency fluctuations[10] a exponential decrease $\exp(-t/t_0)$ of the contrast would be expected [92]. However, the optimal exponential fit shown in 6.12 (dashed line) is only poorly modelling the data, while a Gaussian model $\propto \exp(-(t/t_0)^2)$ with $t_0 = 0.94(5)$ ms is fitting the data well (solid line). Compared to the fit to the white noise model, the observed noise shows an excess for frequencies ≤ 1.5 kHz.

6.5.4. Spin-echo technique

Spin-echoes are a spectroscopic technique invented in nuclear magnetic resonance experiments [93]. We adapt this technique in our experiments in order to cancel the dephasing of atomic superpositions and improve our coherence time. In Fig. 6.13 again the setup of a Ramsey interference experiment is shown. However, in this setup an additional carrier laser pulse of length pulse π is applied after half of the Ramsey waiting time t implementing the spin-echo. The action of this spin-echo pulse can be best understood by considering its action on the Bloch vector, shown in the Bloch sphere pictures in Fig. 6.13. Suppose the phase of the atomic superposition is drifting at a constant rate during the Ramsey experiment, which for example could be caused by a drift of the ambient magnetic field. After half of the Ramsey waiting time the Bloch vector will be rotated by an angle of ϕ in the equatorial plane. Now, the spin-echo pulse, whose phase is adjusted, such that we perform a π rotation around the $\bar{y}$-axis, will mirror the Bloch vector at the x-axis. Then in the second half of the Ramsey waiting time the phase drift will return the Bloch vector to its initial position. Thus, by introducing the spin-echo pulse in the center of the Ramsey experiment, it is possible to cancel a dephasing of the atomic superposition, which takes place on a time scale greater or equal than the length

---

[10]This noise model could be expected to be suitable, if our major noise source would be frequency fluctuations of a laser with an Lorentzian line shape.

of the Ramsey experiment.

A series of Ramsey experiments with different waiting times including a spin-echo pulse were carried out. The dependence of the Ramsey contrast on the waiting time is shown in Fig. 6.12 (triangles). A much improved coherence time of ≥ 3.5 ms is observed. Perfect Ramsey contrast is observed up to a waiting time of 1 ms, after which the contrast is starting to decrease. From this behavior it can be inferred, that a dephasing, which is constant up to a 1 ms, is cancelled by the applied spin-echo. This dephasing is most likely caused by a drift of the ambient magnetic field.

6. Experimental techniques and prerequisites

7. Deterministic preparation of Bell states

7.1. Introduction

Entangled states of two qubits, which are generally called Bell states, have been experimentally realized in several different physical systems. Entangled states of a pair of photons have been studied, where the preparation of the entangled pair relied on stochastic processes like spontaneous emission cascades or parametric down-conversion [8,9]. The first experiment in which two massive particles were prepared in an entangled state in a controlled way, was performed by Hagley et al. [94], who entangled Rydberg states of two Rubidium atoms, which interacted by interchanging a single photon via a microwave cavity. The first experiments in which the internal states of two ions confined in a Paul trap were entangled, were carried out in the group of D.J. Wineland, who prepared Bell states deterministically and investigated the lifetime of different Bell states [60,95].

In this chapter entangled states of two ion qubits are studied. First, the pulse sequences which prepare all four Bell-states are introduced. Next the generated Bell states are investigated by determining their density matrix using quantum state tomography. Finally, the time-evolution of the prepared entangled states is studied.

7.2. Pulse sequence for preparation of Bell states

We want to entangle the internal states of two ions trapped in a linear Paul trap. First of all we assume both ions to be initialized in state $|S\rangle$ and one of the ion string's common vibrational modes to be cooled to the ground state $|n=0\rangle$. Starting from $|SS, n=0\rangle$ all four Bell states can be generated with the following pulse sequences:

$$U_{\psi_\pm} = R_2^+(\pi, \pm\frac{\pi}{2}) \cdot R_2(\pi, \frac{\pi}{2}) \cdot R_1^+(\frac{\pi}{2}, -\frac{\pi}{2}), \tag{7.1}$$

$$U_{\phi_\pm} = R_2(\pi, 0) \cdot U_{\psi_\pm}. \tag{7.2}$$

This pulse sequence is also shown in Fig. 7.1 as a quantum circuit using the notation introduced in Sec. 2.5. For example, the pulse sequence U_{ψ_+} works as follows:

$$|SS, 0\rangle \xrightarrow{R_1^+(\frac{\pi}{2}, -\frac{\pi}{2})} \frac{1}{\sqrt{2}} (|SS, 0\rangle + |SD, 0\rangle)$$

$$\xrightarrow{R_2(\pi, \frac{\pi}{2})} \frac{1}{\sqrt{2}} (|DS, 0\rangle + |DD, 1\rangle)$$

$$\xrightarrow{R_2^+(\pi, \pm\frac{\pi}{2})} \frac{1}{\sqrt{2}} (|DS\rangle + |SD\rangle) \cdot |n=0\rangle. \tag{7.3}$$
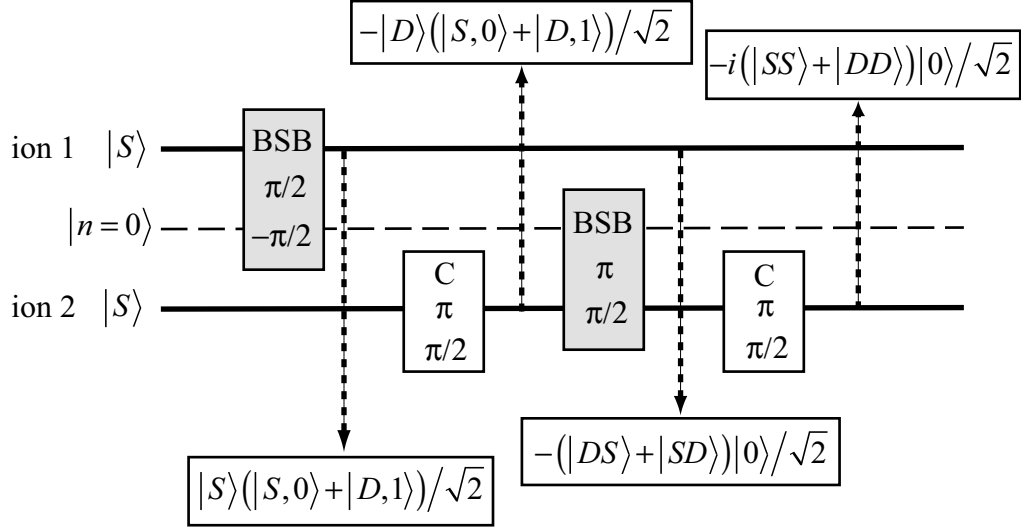
Figure 7.1.: Pulse sequence in order to prepare Bell states. The solid lines represent the quantum state of ions 1 and 2, while the dashed line represents the vibrational mode's state. The quantum state of the ion string is shown for all intermediate steps.

The initial blue sideband pulse $R_1^+(\pi, \pi/2)$ entangles the vibrational mode and the first ion's internal state. The following two pulses $R_2^+(\pi, \pi/2) \cdot R_2(\pi, \pi/2)$ map the vibrational state onto the internal state of the second ion. This pulse sequence nicely illustrates the role of the vibrational mode in ion trap experiments. It serves as a mean to mediate interactions between different qubits within the ion string. Furthermore, conditional operations become possible using sideband pulses, since a blue sideband pulse will couple the levels $|S, 0\rangle$, $|S, 1\rangle$, and $|D, 1\rangle$ to other levels but does not interact with the level $\{D, 0\}$. In the pulse sequence shown above the vibrational mode is only temporarily populated. Its state is transferred back to $|n = 0\rangle$ after completion of the pulse sequence, such that it is again separable from the ions' internal states.

Provided one has prepared a Bell state $\Psi_\pm$, this state can be transformed into a Bell state of the type $\Phi_\pm$ by applying a single carrier π-pulse on one of the ions:

$$\Psi_\pm = \frac{1}{\sqrt{2}} \left(|SD\rangle \pm |DS\rangle \right) \xrightarrow{R_2(\pi, 0)} \frac{1}{\sqrt{2}} \left(|SS\rangle \pm |DD\rangle \right) = \Phi_\pm. \tag{7.4}$$

7.3. Experimental results: Preparation of Bell-states

For the experimental realization of Bell states two ions were loaded into the trap. For the blue sideband operations we had to choose one of the available vibrational modes. Off-resonant excitation of the carrier transition should be decreased for a larger detuning, which allows to increase the Rabi frequency of the sideband transitions. Therefore the breathing mode was chosen, which is farther away from the carrier transition ($\omega_b = 2\pi \cdot 2.1$ MHz) compared to the center-of-mass mode ($\omega_{\mathrm{cm}} = 2\pi \cdot 1.2$ MHz). The breathing mode was prepared in its ground

state $|n = 0\rangle$ by sideband cooling for 6 ms. The ground state was reached with a probability of $\approx 99\%$. The Rabi frequency of the sideband transition belonging to the breathing mode slightly depends on the number of phonons in the center-of-mass mode (cf. 4.3), which are left after Doppler cooling. Therefore, in order to reduce this dependence, the center-of-mass mode was subjected to sideband cooling for 2 ms.

The Rabi frequency for the carrier transition was set to $\Omega_{\text{blue}} = (2\pi) \cdot 50$ kHz and $\Omega_{\text{carrier}} = (2\pi) \cdot 4.5$ kHz for the blue sideband transition. The value chosen for the sideband Rabi frequency was a compromise between trying to increase the Rabi frequency as much as possible and avoiding off-resonant carrier excitations. For the chosen Rabi frequencies, the length of the complete pulse sequence shown in Fig. 7.1 was approximately 200 μs.

After laser cooling and the initialization of the qubits all four pulse sequences introduced in the previous section were applied. Quantum state tomography was carried out in order to determine the density matrices of the prepared entangled states. The measured density matrices of the states generated by the pulse sequences designed to prepare the Bell states Ψ_+, Ψ_-, Φ_+ and Φ_-, are denoted as ρ_{Ψ_+}, ρ_{Ψ_-}, ρ_{Φ_+} and ρ_{Φ_-} respectively. As explained in Sec. 2.6 and in Appendix A.1 in order to obtain the density matrix of a two qubit system, nine expectation values of different combinations of the Pauli-operators have to be measured. Each expectation value was determined by repeating the experiment cycle for 200 times.

In Fig. 7.2 the results of the maximum likelihood estimation of the prepared states density matrices are shown. For each pulse sequence the real and imaginary part of the density matrices are plotted. To determine the extent to which the prepared states are identical to the respective ideal states the fidelity defined by $F = \langle \Psi_{id} | \rho | \Psi_{id} \rangle$ can be used [71]. For the density matrix ρ_{Ψ_+} shown in Fig. 7.2(a) the fidelity is $F_{\Psi_+} = \langle \Psi_+ | \rho_{\Psi_+} | \Psi_+ \rangle = 0.91(1)$. For the density matrices ρ_{Ψ_-}, ρ_{Φ_+} and ρ_{Φ_-} depicted in fig. 7.2(b-d) the fidelities are $F_{\Psi_-} = 0.90(1)$, $F_{\Phi_+} = 0.91(1)$ and $F_{\Phi_-} = 0.88(2)$. The quoted errors are due to quantum projection noise in the measurement of the expectation values necessary for the reconstruction of the density matrix. The errors of the fidelities of all other quantities derived from the density matrices were determined by Monte-Carlo simulations (cf. A.2).

The fidelities of the prepared states are all on the order of 90%. The dominant error, which reduces the fidelities are relative fluctuations of laser frequency and the atomic resonance frequency (cf. Sec. 6.5).

Having reconstructed the density matrices of the generated states, the entanglement measures introduced in Sec. 2.7 can be applied to further characterize the states' entanglement properties. As a first test, the eigenvalues of the partial transpose ρ^{PT} were investigated. Provided that ρ is an entangled state ρ^{PT} will have some negative eigenvalues. In case of $\rho_{\Psi_+}^{PT}$ the eigenvalues {-0.42(2), 0.40(2), 0.49(2), 0.53(3)} were obtained. Indeed one of the eigenvalues is negative proving that the state ρ_{Ψ_+} is entangled. The results are even close to what is expected for a maximally entangled state {-0.5, 0.5, 0.5, 0.5}. For the other prepared entangled states similar results were obtained.

The degree of entanglement of the prepared states was also quantified by using the entanglement of formation introduced in Sec. 2.7. Using the method given by Wootters in [75] the entanglement of formation was calculated to be $E_f(\rho_{\Psi_+}) = 0.79(4)$, $E_f(\rho_{\Psi_-}) = 0.75(5)$, $E_f(\rho_{\Phi_+}) = 0.76(4)$ and $E_f(\rho_{\Phi_-}) = 0.72(5)$.
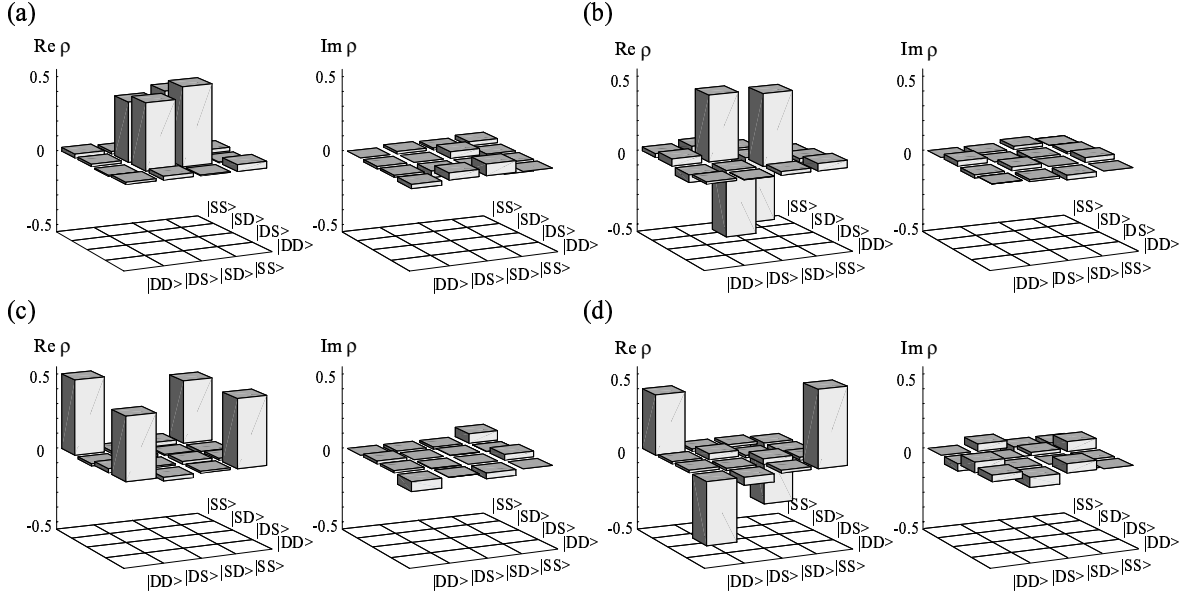
71

(a)

(b)

(c)

(d)

Figure 7.2.: Results of quantum state tomography of the four pulse sequences for preparing Bell-states. Real and imaginary parts of the density matrices a) ρ_{Ψ_+}, b) ρ_{Ψ_-}, c) ρ_{Φ_+} and d) ρ_{Φ_-}.

7.4. Experimental results: Time evolution

Since we are able to deterministically prepare entangled states of two localized qubits, it was possible to investigate the lifetime of these entangled states. The predominant sources of decoherence in our experiment, fluctuations of the laser and the atomic resonance frequency, cause fluctuations of the relative phase of atomic superpositions (cf. Sec. 6.5). These decoherence sources affect all trapped ion qubits in the same way, i.e. correlated phase fluctuations occur. By introducing a waiting time between the end of the state preparation and the quantum state tomography, the decay of the entangled states into a statistical mixture was monitored.

Bell states of the kind $\Psi_\pm$ are expected to be immune against correlated phase flucutations [95]. This invariance can be easily proven by substituting $|S\rangle \rightarrow \exp(i\beta)|S\rangle$ in $\Psi_\pm = 1/\sqrt{2}(|DS\rangle \pm |SD\rangle)$ for both ions. However, this reasoning is only valid as long as the energy difference of state $|D\rangle$ and $|S\rangle$ is the same for both ions. In presence of a magnetic field gradient the two ions experience a slightly different Zeeman shift of their electronic states, which leads to a linear evolution of the relative phase between the $|DS\rangle$ and $|SD\rangle$ components of the $\Psi_\pm$ states. Such a behavior was observed in our experiments and the acquired phase after a waiting time τ is plotted in Fig. 7.3. Here, the phase was determined by calculating the maximum overlap $F_m = \max_\beta(\langle\Psi_\beta|\rho_{\Psi_+}(\tau)|\Psi_\beta\rangle)$ between the measured density matrix $\rho_{\Psi_+}(\tau)$ and the states $\Psi_\beta = 1/\sqrt{2}(|SD\rangle + \exp(i\beta)|DS\rangle)$. A nearly linear change of the phase with time according to $\beta(\tau) = \omega_\beta\tau$ with $\omega_\beta = (2\pi)$ 170 Hz was observed. From the measured phase change this field gradient can be inferred to be $\partial B/\partial z = 0.6$ G/cm along the trap axis. This value was confirmed by later measuring the resonance frequencies of the two ions using
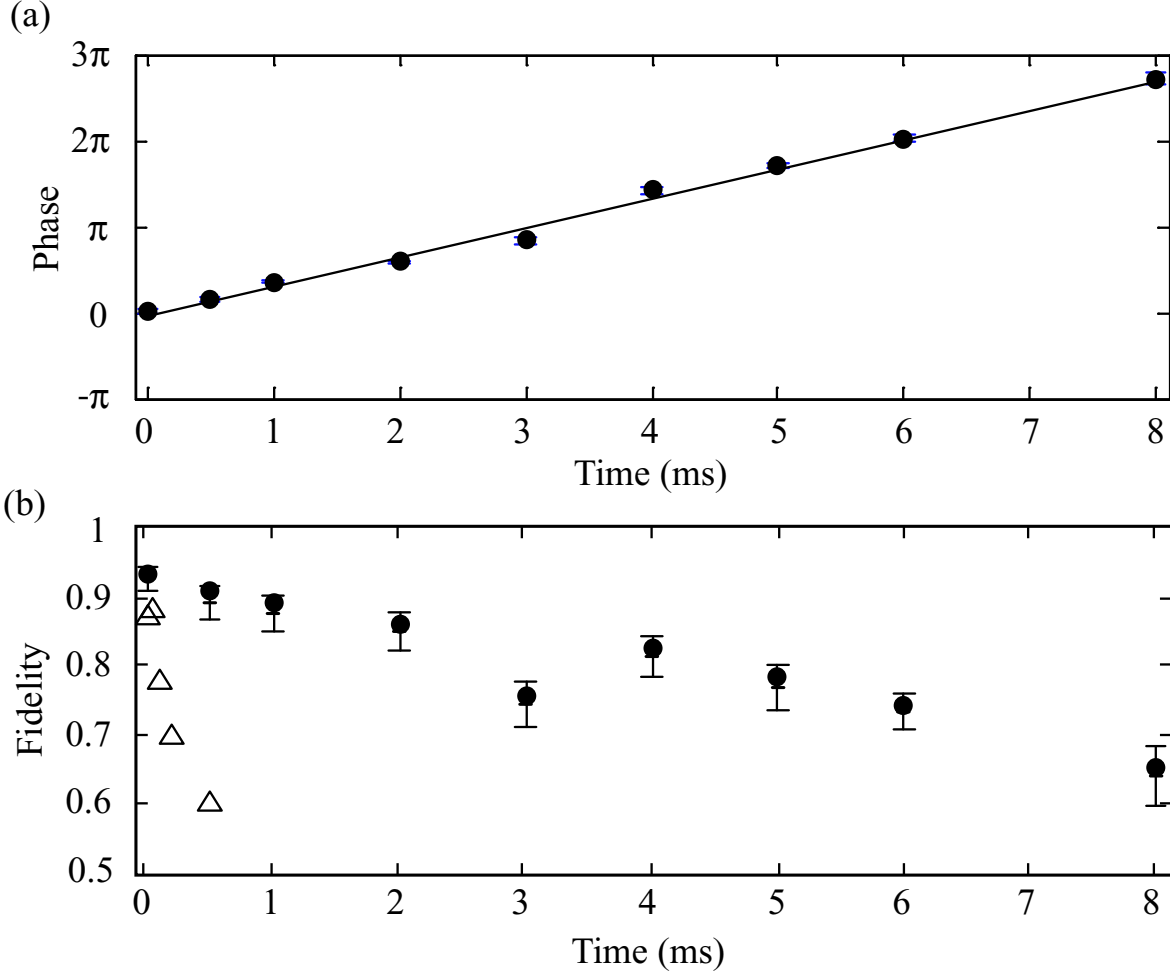
(a)

(b)

Figure 7.3.: Time evolution of the state $\Psi_+ = 1/\sqrt{2}(|SD\rangle + |DS\rangle)$. In a) the relative phase of the superposed states β_m, for which the overlap $F_m = \langle \Psi_\beta | \rho_{\Psi_+}(\tau) | \Psi_\beta \rangle$ is maximized, where $\Psi_\beta = 1/\sqrt{2}(|SD\rangle + \exp(i\beta)|DS\rangle)$. The phase changes linearly in time due to a magnetic field gradient. In b) the obtained values of F_m for $\Psi_+ = 1/\sqrt{2}(|SD\rangle + \exp(i\beta)|DS\rangle)$ (filled circles) and for the states $\Psi_+ = 1/\sqrt{2}(|SS\rangle + \exp(i\beta)|DD\rangle)$ (triangles). The error bars were determined using Monte-Carlo simulations, as described in A.4. The error bars are centered around the mean value of the fidelity of the simulated density matrices, which is indicated by small horizontal bars.
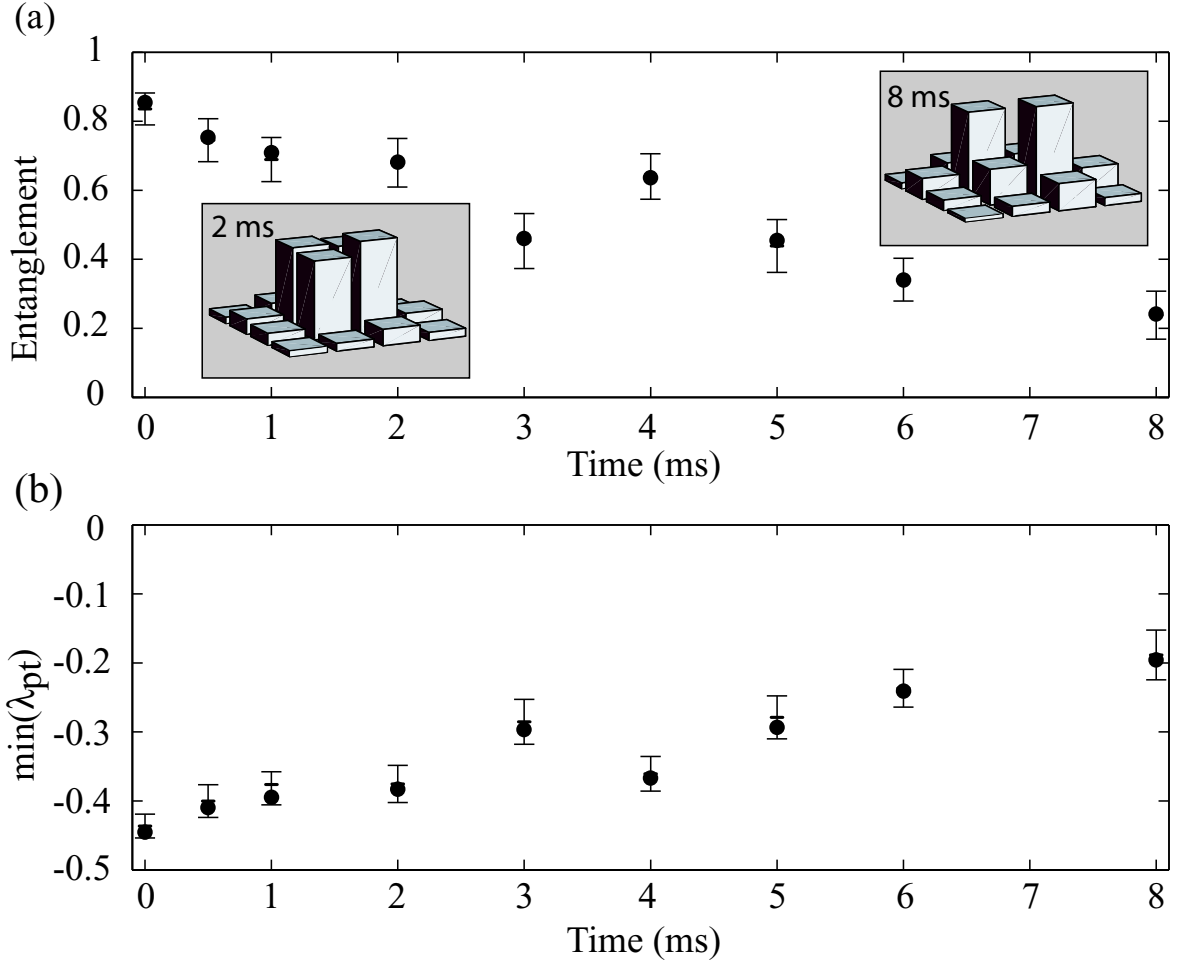
.

Figure 7.4.: Time evolution of entanglement measures of the state $\rho_{\Psi_+}(\tau)$. a) Dependence of the entanglement of formation on the waiting time. Two inset pictures show the absolute value of the corresponding density matrix $\rho_{\Psi_+}(\tau)$ for $\tau = 2$ ms and 8 ms. After 8 ms the non-diagonal elements of the density matrix have decayed. b) Smallest eigenvalue of the negative partial transpose of the density matrix $\rho_{\Psi_+}(\tau)$. The error bars were determined using Monte-Carlo simulations, as described in A.4. The error bars are centered around the mean value of the fidelity of the simulated density matrices, which is indicated by small horizontal bars.

a Ramsey-type experiment.

Due the dephasing of the superposed states, the generated Bell states decay into a statistical mixture, which results in a decrease of the fidelity $F_m = \max_\beta(\langle\Psi_\beta|\rho_{\Psi_+}(\tau)|\Psi_\beta\rangle)$ with increasing waiting times. In Fig. 7.3(b) the results for F_m are shown. For the $\Psi_\pm$ states the fidelity decreases to 75 % within 5 ms, while for states $\Phi_\pm$ this decay occurs within 200 μs. Thus, the intrinsic stability of the $\Psi_\pm$ states against collective dephasing is demonstrated. States of the kind $\Phi_\pm$, however, are found to be much more sensitive to decoherence. This behavior is expected since collective phase fluctuations transforming $|S\rangle$ into $\exp(i\beta)|1S\rangle$ for both ions will change the relative phase $|DD\rangle$ and $|SS\rangle$ by 2β. Additionally, the slow decay of the $\Psi_\pm$ states can also be seen in the entanglement of formation and the smallest eigenvalue of the partial transpose, which are plotted in Fig. 7.4.

Even though the lifetime of $\Psi_\pm$ is already longer than the coherence time of a superposition of $|0\rangle$ and $|1\rangle$ for a single qubit, the coherence time of Ψ_{pm} states should in principle be only limited by spontaneous decay of the $D_{5/2}$ level. The reason for the reduced lifetime was identified to be the 866 nm repumper laser. This laser was not switched off during the preparation and subsequent waiting time. Since it is coupled into the trap from two different directions an interference pattern is established, such that time-varying and spatially inhomogeneous Stark-shifts are induced on the qubit transitions.

After installing shutters for the 866 nm light and improving the homogeneity of the magnetic field much longer lifetimes of the $\Psi_\pm$ states could be observed. Plotted in Fig. 7.5 is the time evolution of the expectation value $\langle\sigma_x^{(1)}\otimes\sigma_x^{(2)}\rangle$ after a Ψ_- state was produced. This expectation value slowly oscillates at a frequency of $\omega = 2\pi \cdot 7.2(1)$ Hz, due to the remaining magnetic field gradient along the trap axis. The amplitude of this oscillation gives a lower bound for the fidelity of our entangled state. It can be seen that the amplitude is damped, indicating a slow decrease in fidelity over time. Spontaneous decay of the $D_{5/2}$ level would lead to an exponential decay with a decay time of $\tau = 1.16$ s [90]. From the data shown in Fig. 7.5 the decay time can be inferred to be $\tau = 1.05(0.15)$ s, which shows that the lifetime of $\Psi_\pm$ states is indeed only limited by the lifetime of the $D_{5/2}$ state.
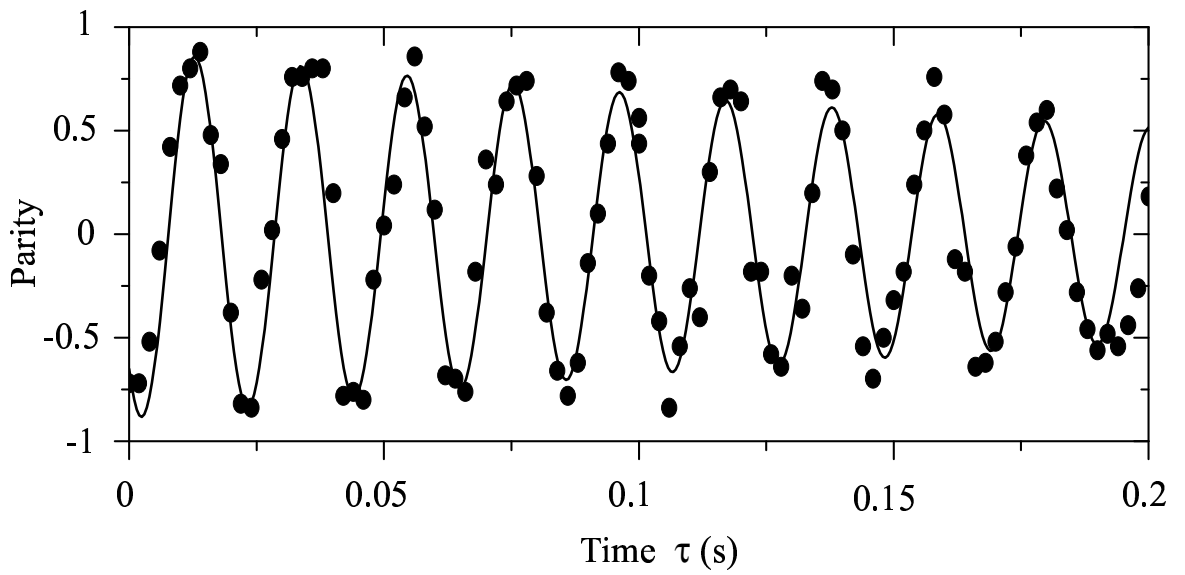
Figure 7.5.: Time evolution of the expectation value $\langle \sigma_x \otimes \sigma_x \rangle$ for a state $\rho_{\Psi_+}(\tau)$. The oscillation at $f = 7.2(1)$ Hz is caused by the residual magnetic field gradient. The observed damping indicates a loss of fidelity with increasing time and is caused by spontaneous emission from the metastable upper $D_{5/2}$ level.

8. The Two Ion CNOT Gate

8.1. Introduction

In Ch. 2 the fundamental operations necessary to build a quantum computer were introduced. As has been noted in Sec. 2.5 single qubit rotations and the controlled NOT operation (CNOT) between two arbitrary qubits form a universal set of gates, which are sufficient to implement an arbitrary unitary operation or algorithm. In the case of an ion trap quantum computer, using internal electronic states of the ions as qubits, it is straightforward to implement single qubit rotations, by addressing single ions within a linear chain of ions with laser pulses of suitable frequency, length and phase.

For the implementation of a controlled NOT gate between two trapped ions the first and most prominent proposal was made by Cirac and Zoller in 1995 [37]. They proposed to implement a controlled-NOT gate by first mapping the quantum state of one ionic qubit onto one of the common vibrational modes of the ion string and then performing a CNOT operation between this vibrational state and the electronic state of another qubit. Finally the vibrational state is mapped back onto the internal state of the first ion. The crucial idea in the Cirac-Zoller scheme is to use one of the common vibrational modes of the ions, which is often denoted as the "bus" mode, to mediate an interaction between two ions at different places within an ion string.

The central step of performing a CNOT gate between the vibrational state and an internal state of an ion was already realized by Monroe et. al in 1995 [59] using a single ion in a spherical Paul trap. In our experimental setup a CNOT gate between the vibrational state and an internal state of an ion was realized and served as a part of the implementation of the Deutsch-Josza algorithm with a single trapped ion [66].

Implementations of a two ion CNOT gate different from Cirac and Zoller's have been proposed by several authors [57, 58] but most have not yet been implemented. One example for an alternative implementation of a universal quantum gate equivalent to the CNOT gate has been demonstrated with a single trapped ion [96]. So far the only experimental implementation of a CNOT quantum gate between two trapped ions, apart from the work presented in this thesis, was realized by Leibfried et. al [62], who implemented a phase gate by a spin dependent optical dipole force.

8.2. Quantum circuit for the two ion CNOT gate

A graphical representation of the scheme proposed by Cirac and Zoller can be found in Fig. 8.1(a). As can be seen the vibrational mode used for mediating the interaction between the ions is assumed to be cooled to its ground state $|n = 0\rangle$.

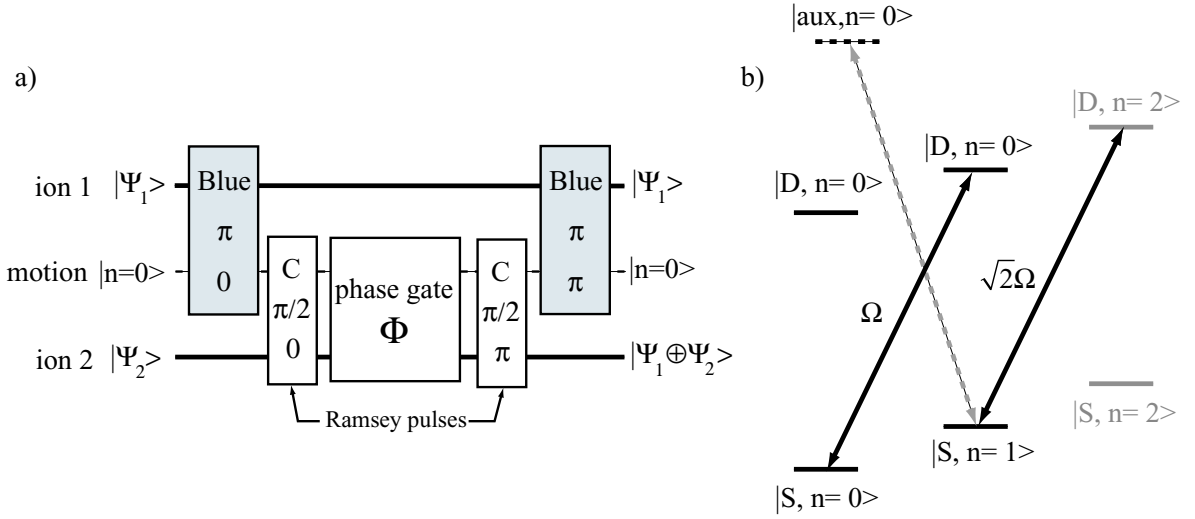The scheme starts by mapping the state of the first qubit onto the chosen vibrational mode.

Figure 8.1.: Illustration of two ion controlled NOT gate proposed by Cirac and Zoller. a) Quantum circuit for the CNOT gate. The line in the middle represents the vibrational mode, which serves as the intermediary "bus" qubit. After completion of the operation the second qubit is in the state $|\Psi_1 \oplus \Psi_2\rangle$ where $\oplus$ denotes the addition modulo 2. b) Computational basis states for our $S_{1/2} \leftrightarrow D_{5/2}$ transition and the possible blue sideband transitions with their respective Rabi frequencies. Additionally the transition through an auxiliary level $|\text{aux}\rangle$ is shown, which was proposed by Cirac and Zoller to implement the phase gate operation.

This can be done applying a blue sideband π-pulse on the first ion, which maps the $|0, n = 0\rangle$ state onto $|1, n = 1\rangle$ while the $|1, n = 0\rangle$ state is unaffected, as can be seen from 8.1(b).

The next steps are to perform a CNOT operation between the vibrational mode and the second ion and then to map the vibrational mode's state back to the internal state of ion 1 by another π pulse on the blue sideband. The CNOT operation is decomposed as in Eq. 2.13 into two $\pi/2$ carrier pulses, which can be thought of as Ramsey pulses, and a phase gate. To implement the step of performing a phase gate between the vibrational mode and the second qubit's internal state Cirac and Zoller proposed a 2π sideband pulse on the second ion coupling the $|S, n = 1\rangle$ to an additional excited state $|\text{aux}\rangle$. In our experiment this additional level could be another one of the available Zeeman levels of the $D_{5/2}$ state. A red sideband 2π-pulse on the $|S, n = 1\rangle \leftrightarrow |\text{aux}, n = 0\rangle$ transition results in a transformation $|S, n = 1\rangle \rightarrow -|S, n = 1\rangle$, while all the other states $|D, n = 0\rangle, |S, n = 0\rangle$ and $|D, n = 1\rangle$ are unaffected. However, as stated in Sec. 4.4.3 the $S_{1/2}(m = -1/2) \leftrightarrow D_{5/2}(m = -1/2)$ we use to implement the qubit is already the Zeeman transition least affected by magnetic field fluctuations via the Zeeman effect. All other Zeeman transitions would be much more affected, causing a much larger susceptibility to decoherence because of the fluctuating magnetic field during the full 2π-rotation on the vibrational sideband.

What if one could perform a sideband 2π-rotation without employing an additional level? As can be seen in Fig. 8.1(b) a blue sideband laser pulse would couple to the $|S, n = 0\rangle$, $|D, n = 1\rangle$ and $|D, n = 1\rangle$ levels but not to the $|D, n = 0\rangle$ level, containing the conditional dynamics
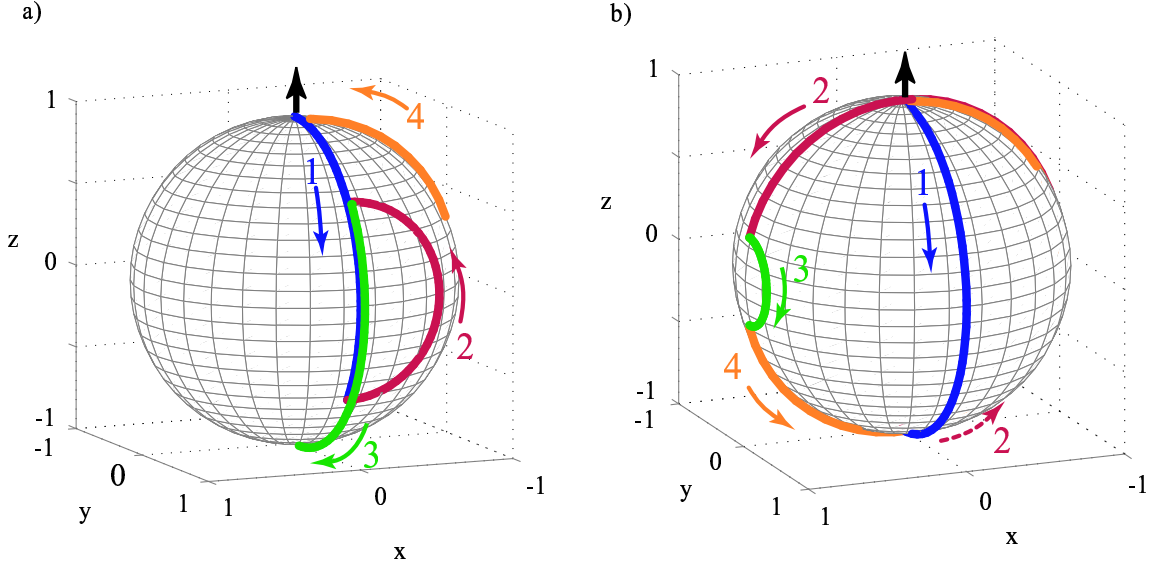
Figure 8.2.: Behavior of the Bloch vector for the composite phase gate U_Φ. a) Trajectory for the transition $|S, n = 0\rangle \leftrightarrow |D, n = 1\rangle$. Initially the state is assumed to be $|S, n = 0\rangle$ represented by the black arrow pointing up. The first pulse $R^+(\pi/\sqrt{2}, 0)$ rotates the Bloch vector around the x-axis by an angle $\pi/\sqrt{2}$. The second pulse $R^+(\pi, \pi/2)$ corresponds to a π-rotation around the y-axis, mirroring the Bloch vector about the x-y-plane. Then the third pulse, which is identical to the first one, rotates the Bloch vector around the x-axis, such that it points downwards, corresponding to the state $|D, n = 1\rangle$. Finally, the fourth pulse (like the second pulse) is a π-rotation around the y-axis, returning the Bloch vector to its initial state. During the whole pulse sequence a phase factor of -1 is acquired, i.e. the transformation $|S, n = 0\rangle \rightarrow -|S, n = 0\rangle$ and $|D, n = 1\rangle \rightarrow -|D, n = 1\rangle$. b) Action of the same pulse sequence on the $|S, n = 1\rangle \leftrightarrow |D, n = 0\rangle$ is shown. Due to the higher Rabi frequency for this transition the pulse sequence reads: $U_\Phi' = R^+(\pi, 0) \cdot R^+(\sqrt{2}\pi, \pi/2) \cdot R^+(\pi, 0) \cdot R^+(\sqrt{2}\pi, \pi/2)$. Again, the whole pulse sequence returns the Bloch vector into its initial position, while acquiring a phase factor of -1, thus acting like 2π-rotation.

necessary to implement a phase gate. However, as stated in Eq. 4.15 the Rabi frequency of blue sideband transitions has a square root dependency on the number of phonons present. Therefore a blue sideband laser pulse representing a 2π rotation on the $|S, n = 0\rangle \leftrightarrow |D, n = 1\rangle$ would represent a $2\sqrt{2}\pi$ rotation on the $|S, n = 1\rangle \leftrightarrow |D, n = 2\rangle$ transition, resulting in a part of the population left in the $|D, n = 2\rangle$ state, leaving the *computational subspace* of the states $\{|D, n = 0\rangle, |D, n = 1\rangle, |S, n = 0\rangle, |S, n = 1\rangle\}$.

A solution for this problem using the *composite pulse technique* borrowed from nuclear magnetic resonance spectroscopy was proposed by Childs and Chuang [79]. They proposed to design a pulse sequence such that sideband transitions of the kind $|n = 0\rangle \leftrightarrow |n = 1\rangle$ would undergo a effective 2π rotation while transitions of the kind $|n = 1\rangle \leftrightarrow |n = 2\rangle$ would perform a 4π rotation. Such a *composite pulse sequence* would, for example, be:

$$\Phi = R^+\left(\frac{\pi}{\sqrt{2}}, \frac{\pi}{2}\right) \cdot R^+\left(\pi, 0\right) \cdot R^+\left(\frac{\pi}{\sqrt{2}}, \frac{\pi}{2}\right) \cdot R^+\left(\pi, 0\right), \tag{8.1}$$

where the angles are given for the $|1, n = 0\rangle \leftrightarrow |0, n = 1\rangle$ transition. A representation of the corresponding behavior of the Bloch vector for $|n = 0\rangle \leftrightarrow |n = 1\rangle$ and $|n = 1\rangle \leftrightarrow |n = 2\rangle$ transitions is shown in Figs. 8.2(a) and (b) respectively. In the computational subspace $\{|0, n = 0\rangle, |0, n = 1\rangle, |1, n = 0\rangle, |1, n = 1\rangle\}$ the unitary transformation corresponding to this pulse sequence is given by:

$$\Phi = \begin{pmatrix} 1 & 0 & 0 & 0 \\ 0 & -1 & 0 & 0 \\ 0 & 0 & -1 & 0 \\ 0 & 0 & 0 & -1 \end{pmatrix}$$

which is, apart from a global phase factor of -1, the phase gate introduced in Sec. 2.3. The complete pulse sequence to implement a CNOT between two trapped ions is then:

$$U_{\text{CNOT}}^{12} = R_2^+\left(\pi, 0\right) \cdot R_1\left(\frac{\pi}{2}, 0\right) \cdot \Phi_2 \cdot R_1\left(\frac{\pi}{2}, \pi\right) \cdot R_2^+\left(\pi, 0\right)$$

$$= \begin{pmatrix} 0 & 0 & -i & 0 \\ 0 & -1 & 0 & 0 \\ i & 0 & 0 & 0 \\ 0 & 0 & 0 & -1 \end{pmatrix} \tag{8.2}$$

Here, the symbol Φ_2 denotes the phase gate pulse sequence in Eq. 8.1 applied to ion 2. The unitary evolution of this CNOT differs from the ideal CNOT introduced in Sec. 2.3. Our CNOT is first of all a zero-controlled NOT gate, which flips the state of the target qubit if the control ion is in state $|D\rangle = |0_L\rangle$. Additionally the target is not only flipped but also its phase is changed. Nonetheless, our CNOT operation U_{CNOT} is fully equivalent to the ideal CNOT and could be transformed into it using only single qubit operations[1].
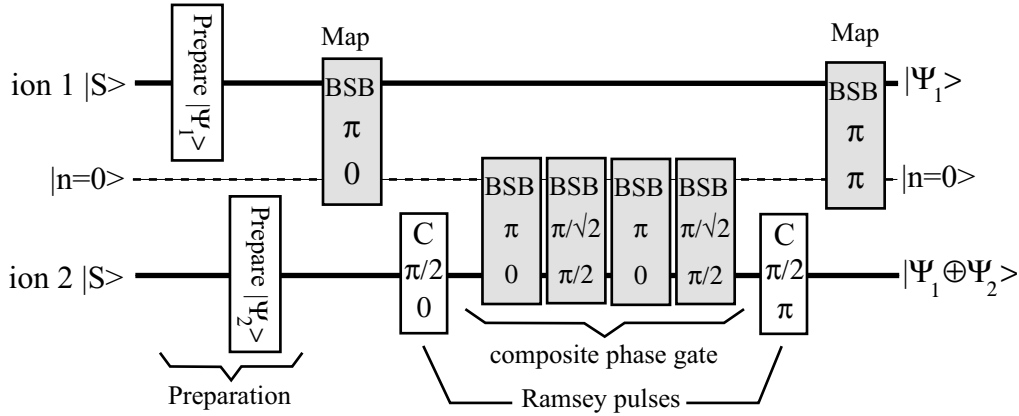
Figure 8.3.: Pulse sequence for the realization of the Cirac-Zoller CNOT gate. The two solid lines represent the internal states of the two ions, the dashed line indicates the state of the vibrational mode used to implement the controlled operation between the internal states of the two ions.

8.3. Experimental Results

The Cirac-Zoller-CNOT gate was demonstrated using a two ion crystal. For the same reasons as in the experiments about Bell states, the vibrational mode, chosen to serve as our "bus" mode, was the breathing mode at a frequency of $\omega_b = 2\pi \cdot 2.1$ MHz from the carrier transition. For the application of the Cirac-Zoller scheme it is necessary to prepare the bus mode in its ground state. Therefore, the breathing mode was prepared in $|n = 0\rangle$ using sideband cooling.

The pulse sequence, carried out after the initial laser cooling stage, is shown in Fig. 8.3. Here, the first ion is the control qubit and the second ion the target qubit, corresponding to the bra-ket notation $|\text{target}, \text{control}\rangle$. Both ions were initially prepared in their $|S\rangle = |1_L\rangle$ ground state and then the desired input states for the gate sequence were generated by appropriate carrier pulses. The period of one Rabi oscillation on the blue sideband transition was set to $T_{\text{blue}}^{2\pi} = 190\mu s$ and the period for carrier transitions set to $T_{\text{blue}}^{2\pi} = 26\mu s$. Therefore, the complete CNOT pulse sequence takes a total time of about 500 μs.

8.3.1. State evolution during Cirac-Zoller-CNOT gate

For both ions the temporal evolution of the probability to find the ions in the $D_{5/2}$ state was measured during the CNOT pulse sequence. This was done by truncating the pulse sequence as a function of time and measuring the $D_{5/2}$ state probability for each ion. The results are shown in Fig. 8.4 together with the theoretically expected behavior, which is indicated by solid lines. The theoretical behavior was calculated assuming only the measured Rabi frequencies for the sideband and carrier transition and the addressing error. No additional parameters

---

[1]The necessary transformation is $[i \cdot R_1(\pi, 0) \cdot R_1(\frac{\pi}{2}, \frac{3}{2}\pi) \cdot R_1(\frac{\pi}{2}, 0) \cdot U_{C'} \cdot R_1(\frac{\pi}{2}, \pi) \cdot R_1(\frac{\pi}{2}, \frac{\pi}{2})]$.

were used to fit these curves to the data points.

Instead of observing only the $D_{5/2}$ population of each ion alone, more information was revealed by measuring the probabilities to find the qubits in one of their joint basis states $\{|DD\rangle, |DS\rangle, |SD\rangle, |SS\rangle\}$. The measured time evolution of these states during the CNOT pulse sequence is shown in Fig. 8.5, alongside with the theoretically expected behavior. From these results the measured probabilities of finding the qubits in the different output states for a given input states were inferred, such that the following truth table was constructed:

	$|DD\rangle$	$|DS\rangle$	$|SD\rangle$	$|SS\rangle$
$|DD\rangle$	0.22(4)	0.09(3)	0.78(3)	0.08(2)
$|DS\rangle$	0.02(1)	0.70(5)	0.07(3)	0.14(3)
$|SD\rangle$	0.73(5)	0.07(2)	0.14(4)	0.05(2)
$|SS\rangle$	0.04(2)	0.15(3)	0.01(1)	0.74(3)

Here every column corresponds to the measured probabilities of the different basis states after completion of the CNOT pulse sequence for a given input basis state. Ideally this table should reproduce the absolute values of the entries of the unitary operation in Eq. 8.2. For a given input state we were able to transfer 70 - 80 % of the population into the correct output state given by Eq. 8.2.

8.3.2. Preparation of entangled states

In Sec. 2.4.2 a quantum circuit consisting of a Hadamard operation and a controlled-NOT was shown to map the Bell states onto the computational basis states of two qubits. This procedure also works the other way around, i.e. Bell states can be prepared by starting from the computational basis states, preparing one of the qubits in a superposition and then applying a controlled NOT operations.

To prove that our CNOT pulse sequence is indeed capable of generating entangled states, the first ion, which acts as the control qubit, was prepared in a superposition state by a $\pi/2$ carrier pulse. Then this input state was subjected to the CNOT gate. The result of this experiment is expected to be a state of the kind $1/\sqrt{2} \cdot (|DD\rangle + e^{i\alpha}|SS\rangle)$. Indeed the probabilities to find the ion string in the states $|DD\rangle$ and $|SS\rangle$ after completion of the CNOT gate were measured to be:

$$P_{DD} = 0.45(3)$$
$$P_{SS} = 0.42(3). \tag{8.3}$$

However, these populations alone do not prove that the prepared state is entangled. Additionally one has to show that the ions are in a coherent superposition of $|DD\rangle$ and $|SS\rangle$, by measuring the "coherences" or off-diagonal elements of the prepared state's density matrix. For this purpose we used a method employed in [61]. To both ions $\pi/2$-carrier pulses with phase ϕ are applied after the CNOT sequence. Then the dependence of the parity P on the phase ϕ is observed, where the parity is defined as:

$$P = P_{DD} + P_{SS} - (P_{SD} + P_{DS}). \tag{8.4}$$

For an entangled state an oscillation of the parity with $\cos(2\phi)$ is expected, whereas a non-entangled state is expected to vary with $\cos(\phi)$ only. In Fig. 8.7 the measured behavior of
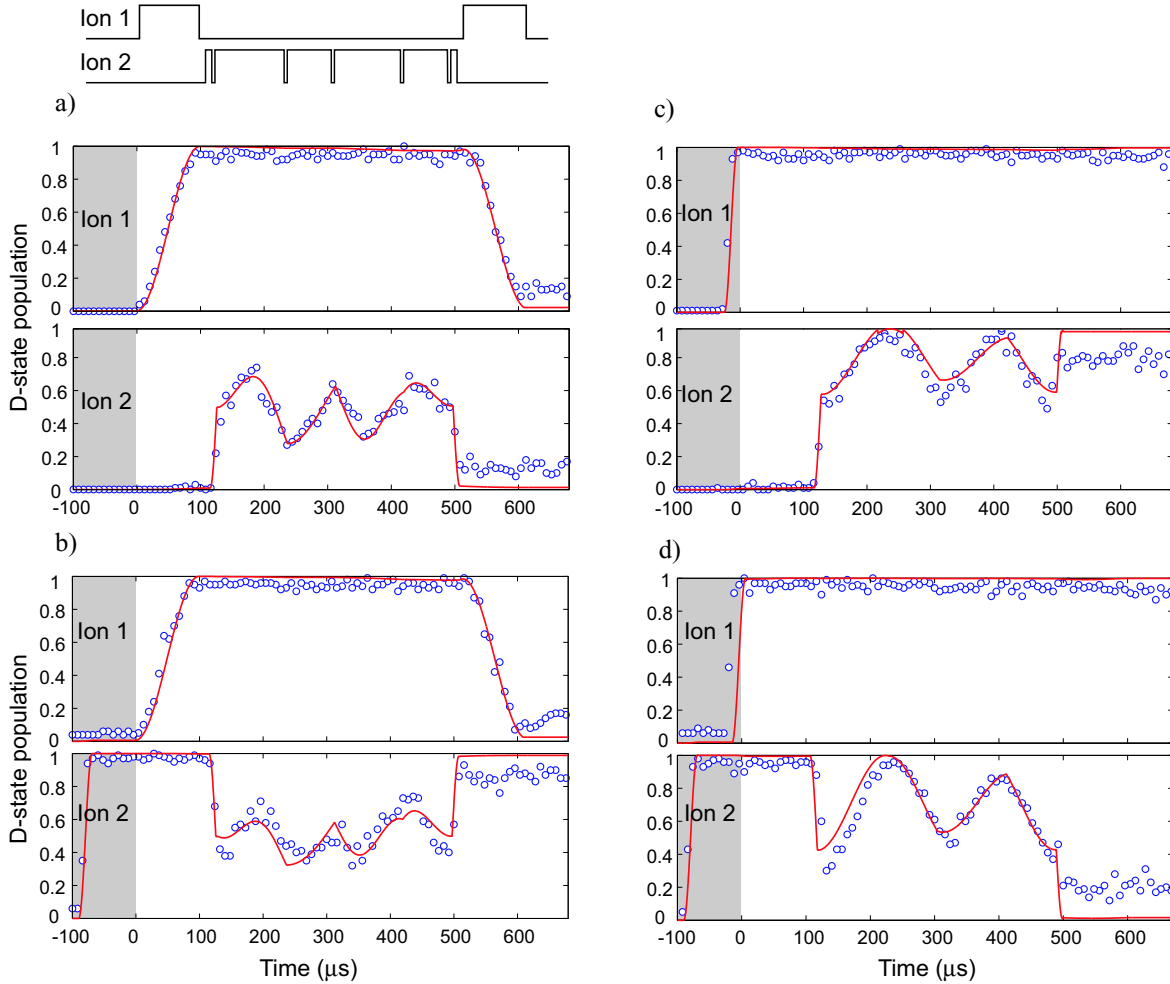
Figure 8.4.: State evolution of both qubits under the action of the CNOT gate for four different input states. The pulse sequence is truncated as function of time and the probability to find the ions in the $D_{5/2}$ state is measured. The solid lines show the theoretically expected behavior. The CNOT pulse sequence starts at $t = 0$ ms. The grey shaded area indicates the stage of input state preparation. The input state was $|SS\rangle$ in a), $|DS\rangle$ in b), $|SD\rangle$ in c) and $|DD\rangle$ in d).
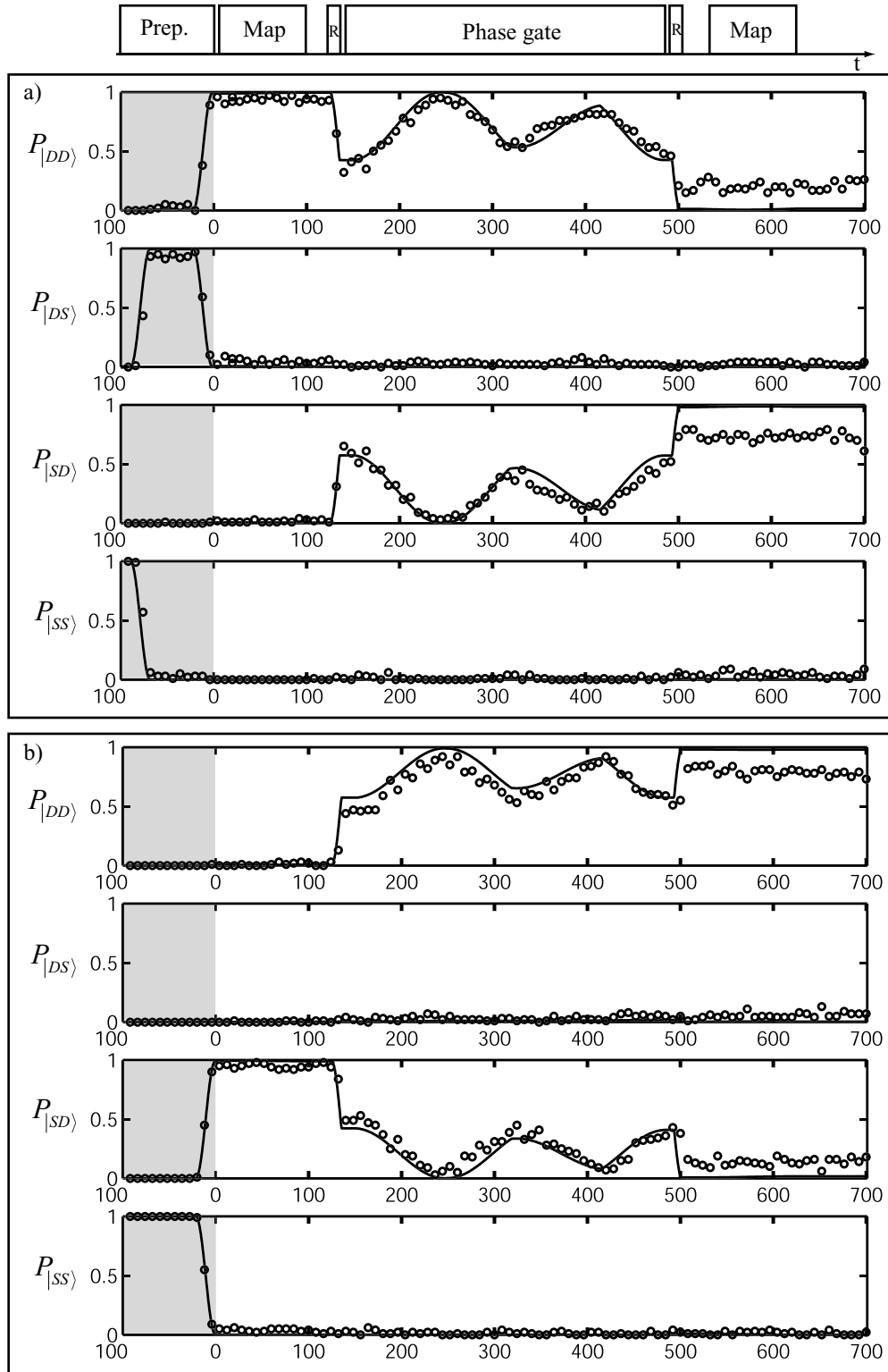
Figure 8.5.: Time evolution of the probabilities to find the ions in the basis states $\{|DD\rangle, |DS\rangle, |SD\rangle, |SS\rangle\}$. The ions were initially prepared in the $|DD\rangle$ state for a) and in $|SD\rangle$ for b). The solid line indicates the theoretically expected behavior. The grey shaded area again represents the period for input state preparation.
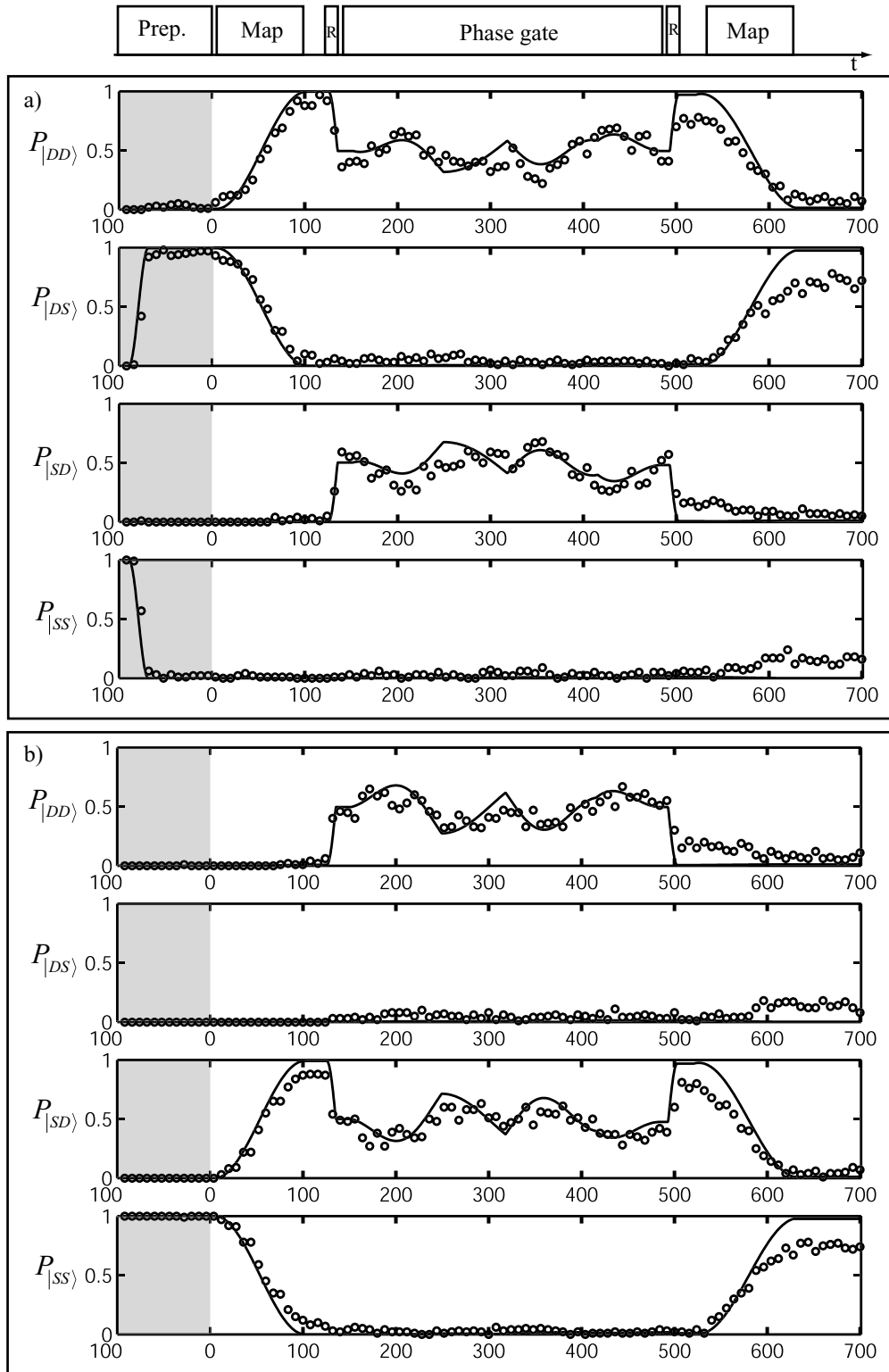
Figure 8.6.: Time evolution of the probabilities to find the ions in the basis states $\{|DD\rangle, |DS\rangle, |SD\rangle, |SS\rangle\}$. The ions were initially prepared in the $|DS\rangle$ state for a) and in $|SS\rangle$ for b). The solid line indicates the theoretically exepected behavior. The grey shaded area again represents the period for input state preparation.
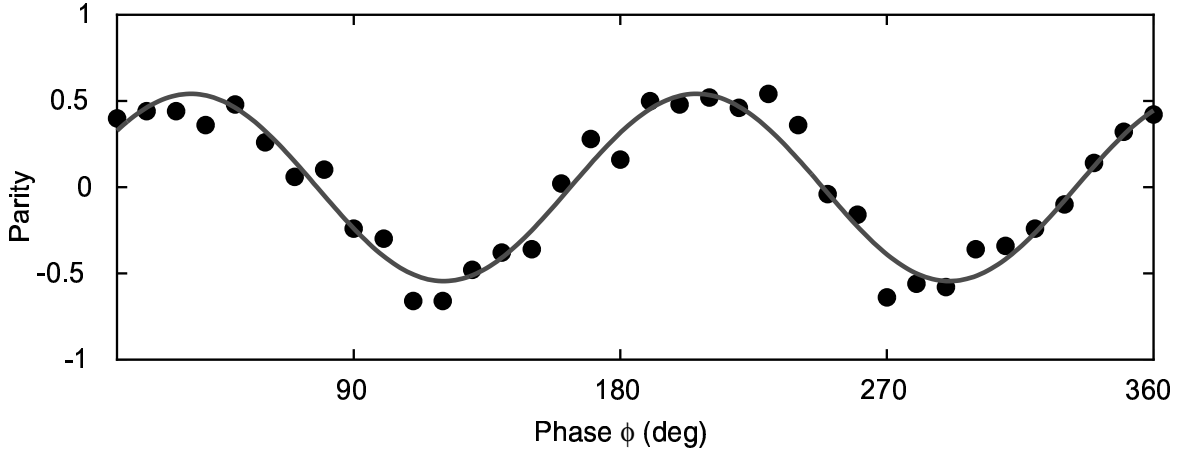
Figure 8.7.: Analysis of an entangled state of the kind $1/\sqrt{2} \cdot (|DD\rangle + e^{i\alpha}|SS\rangle)$ prepared by using the CNOT pulse sequence. After preparation of this state $\pi/2$-carrier pulses with variable phase ϕ are applied two both ions. The measured dependence of the parity $P = P_{DD} + P_{SS} - (P_{SD} + P_{DS})$ on the the phase ϕ is shown. Note that the parity varies with $\cos(2\phi)$ as expected for a an entangled bipartite state.

the parity is shown. The observed oscillation has a period of π, proving entanglement of the prepared state. Furthermore, by measuring the amplitude ρ_{coh} of this oscillation it is possible to infer a lower bound for the fidelity

$$F = \langle\Psi|\rho|\Psi\rangle = \frac{1}{2}\left(P_{DD} + P_{SS} + \rho_{coh}\right),\tag{8.5}$$

where $\Psi = 1/\sqrt{2}(|DD\rangle + e^{-i\alpha}|SS\rangle$ is a maximally entangled state and ρ_{exp} denotes the density matrix of the experimentally prepared state. From the results shown in Fig. 8.7 the amplitude can be determined to be $\rho_{coh} = 0.54(3)$, such that using the results in Eq. 8.3 a fidelity of $F = 0.71(3)$ is obtained. Given the prepared input state, we would expect the phase to be $\alpha = \pi$. However, from the parity oscillation the phase is inferred to be $\alpha = 0.41(7)$, indicating that the CNOT gate is not perfectly reproducing the phases of the ideal evolution given in Eq. 8.2. This was possibly due to either a detuning of the 729 nm laser from the atomic resonance or imperfect compensation of the light shift.

In addition, after quantum state tomography was implemented, it was possible to fully determine the density matrix of an entangled state generated by using the CNOT pulse sequence. In Fig. 8.3.2 the real and imaginary part of the density matrix are shown. The fidelity $F = \langle\Psi|\rho|\Psi\rangle$ with the state $\Psi = 1/\sqrt{2}(|DD\rangle + |SS\rangle)$ was determined to be $F = 80(2)\%$. Therefore, in this experiment a much larger fidelity compared to the experiment described previously was achieved, which is due to the fact that both experiments are separated by about a year during which the experimental setup was improved. In particular, the computer control of the experiment was improved, such that it is easier to keep experimental parameters at their optimal value.
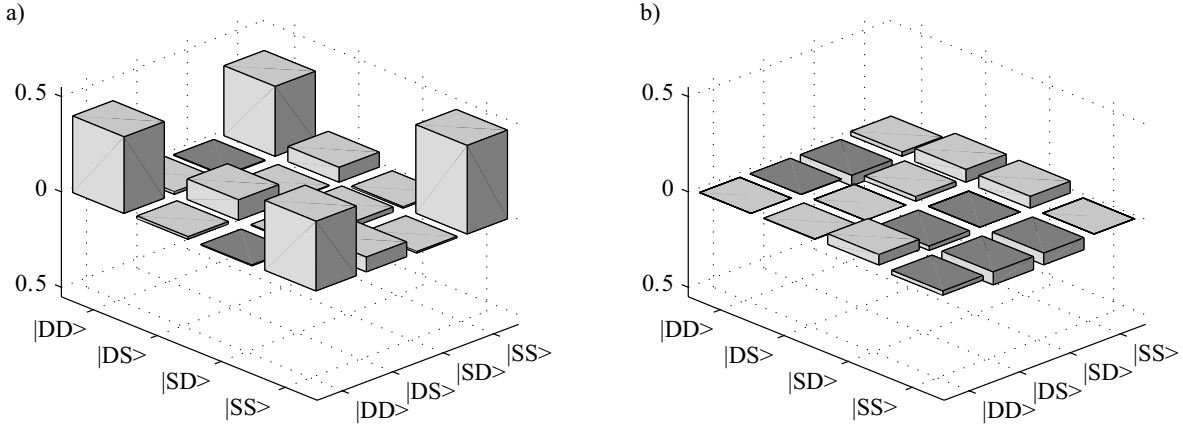
Figure 8.8.: a) Real and b) imaginary part of the density matrix of a Bell state prepared by using our CNOT operation.

8.3.3. Error analysis

The results presented in the previous sections show that we can achieve fidelities on the order of 70 - 80 % for the Cirac-Zoller controlled NOT gate operation[2]. The performance of the CNOT operation is thereby limited by the imperfections of our experimental apparatus.

A major limitation is the performance of the laser system, which is used to manipulate the qubit register. This laser has a limited frequency stability of about 100 Hz on short time scales, causing fluctuations of the laser light's phase with respect to the phase of atomic superpositions. At the same time the laser's frequency is slowly drifting with about 1 Hz/s, resulting in a detuning from the atomic resonance, which can be compensated by measuring the resonance frequency every few minutes and resetting the laser frequency.

The influence of the laser's imperfect frequency stability could be minimized by increasing the Rabi frequency on the blue sideband transition, such that the whole gate operation would take less time. But unfortunately this measure would at the same time increase another error source, namely the off resonant excitation of the carrier transition.

Furthermore, minor error sources are the imperfect laser cooling, leaving residual thermal excitation of the bus mode and all other vibrational modes, fluctuations of the laser intensity and the imperfect addressing of the ions, due to the finite width of the focussed laser beam. To estimate how much the individual error sources contributed to the observed loss in fidelity, for every error source a simulation of our CNOT pulse sequence was carried out for the input states $\{|DD\rangle, |DS\rangle, |SD\rangle, |SS\rangle\}$ and the loss in population of the expected output states recorded. The results of these simulations are summarized in the following table:

---

[2]Here of course the fidelity was inferred by only looking at the final populations after the gate operation, ignoring that the exact phases of the final states are also of importance, when assessing the performance of the gate operation. A better measure, including also information about the output states' phase, would be the *process fidelity*, which can be calculated from the results of a *quantum process tomography* [71].

8. The Two Ion CNOT Gate

Error source	Magnitude	Contribution
Laser frequency noise (phase coherence)	$\sim$100 Hz (FWHM)	11 %
Laser intensity fluctuations	$\sim$3% peak to peak	$\sim$ 1 %
Laser detuning error	$\sim$200 Hz	$\sim$1 %
Residual thermal excitation	$\langle n \rangle_{bus} < 0.02$	2%
	$\langle n \rangle_{other} < 6$	0.4%
Addressing error	5 % in Rabi frequency (at	2 %
	neighbouring ion)	
Off resonant excitation	for $t_{gate} = 600\mu$s	4 %
Total contribution of all error sources	$\Pi_i(1 - \epsilon_i)$	$\sim$ 20 %

Therefore assuming the known imperfections of our experimental apparatus a loss in fidelity of about 20 % can be explained. Therefore the major error source is the frequency noise of our laser system which contributes an error on the order of ten percent. This contribution could be decreased by improving the frequency stability of the 729 nm laser system. However, in order to achieve laser linewidths far below 100 Hz a much more complex setup of the locking scheme would be necessary.

An error source not included in these simulations were fluctuations of the ambient magnetic field which shift the atomic levels via the Zeeman effect, acting therefore in the same way as frequency fluctuations of the laser light.

9. Entangled states of three ions

9.1. Introduction

The results shown in Ch. 7 demonstrated our capability to deterministically prepare and investigate entangled states of two ions. The same techniques can be applied to ion strings consisting of three ions in order to generate tripartite entangled states. In the case of two qubits Bell states are the only kind of maximally entangled states. However, three qubits can be entangled in different ways. It has been shown by Dür et al. that two nonequivalent classes of tripartite entangled states exist [97], which is the class of GHZ-states represented by:

$$|\text{GHZ}\rangle = \frac{1}{\sqrt{2}} \left(|000\rangle + |111\rangle \right) \tag{9.1}$$

and the class of W-states, which is represented by:

$$|W\rangle = \frac{1}{\sqrt{3}} \left(|001\rangle + |010\rangle + |001\rangle \right). \tag{9.2}$$

Both classes are distinguished by the fact that if only local operations and classical communication[1] (LOCC) between the respective subsystems are used, an entangled state belonging to one class cannot be transformed into a state belonging to the other class.

So far, W- and GHZ-states have been successfully created by using polarization entangled photons [98, 99]. The experiments with GHZ-states were motivated by the fact that GHZ-states exhibit such strong quantum correlations, such that an elegant test of the nonlocality of quantum mechanics is possible [7]. Furthermore, nuclear spins of molecules were prepared in a GHZ-state by nuclear-magnetic resonance techniques (NMR) [100].

9.2. Quantum circuits for the preparation of GHZ- and W-states

9.2.1. Preparation of GHZ-states

In order to prepare three ion qubits in a GHZ-state, the ion string is initially prepared in the $|\text{SSS}\rangle$ state and one of its vibrational modes, which serves as the "bus" mode, is cooled to the ground state $|n = 0\rangle$. Starting from this state, the pulse sequence to prepare the ions in a

---

[1]Classical communication means that the kind of local operations or the result of a measurement in one subsystem can be communicated to the parties owning the other subsystems. Nonlocal operations like a CNOT- or CZ-operation are however not allowed.
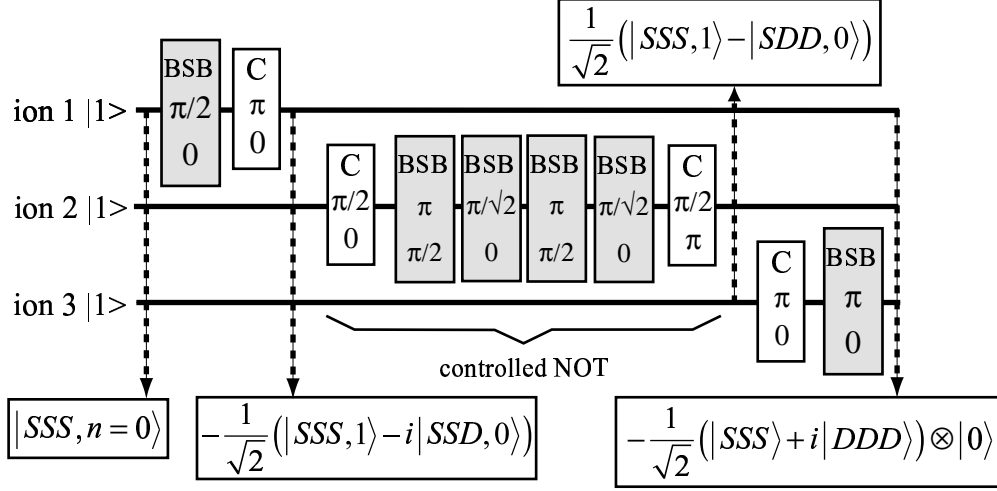
Figure 9.1.: Pulse sequence for the preparation of an ion string of three ions in the GHZ-state $|\Psi\rangle = 1/\sqrt{2}(|SSS\rangle - |DDD\rangle)$. For certain times the intermediate state of the qubits is shown.

GHZ state reads:

$$
\begin{aligned}
U_{\text{GHZ}} =& R_1^+ \left(\pi, 0\right) R_1 \left(\pi, 0\right) \\
& \cdot R_2 \left(\frac{\pi}{2}, \pi\right) R_2^+ \left(\frac{\pi}{\sqrt{2}}, 0\right) R_2^+ \left(\pi, \frac{\pi}{2}\right) R_3^+ \left(\frac{\pi}{\sqrt{2}}, 0\right) R_2^+ \left(\pi, \frac{\pi}{2}\right) R_2 \left(\frac{\pi}{2}, 0\right) \\
& \cdot R_1 \left(\pi, 0\right) R_1^+ \left(\frac{\pi}{2}, 0\right) \\
=& \left[R_1^+ \left(\pi, 0\right) R_1 \left(\pi, 0\right) \right] \cdot U_{\text{CNOT}}^{12} \cdot \left[R_1 \left(\pi, 0\right) R_1^+ \left(\frac{\pi}{2}, 0\right) \right]
\end{aligned}
\tag{9.3}
$$

This pulse sequence, which is depicted in Fig. 9.1, contains ten pulses. The initial $\pi/2$-sideband pulse entangles ion 1 and the vibrational mode, creating the state $(|SS\rangle \otimes (|S, 0\rangle + i|D, 1\rangle))/\sqrt{2}$. The following six pulses on ion 2 represent the Ramsey pulses and controlled phase gate, which are part of the controlled NOT pulse sequence, introduced in the previous chapter. The vibrational mode is in a superposition of the states $|n = 0\rangle$ and $|n = 1\rangle$ and therefore the controlled-NOT sequence on ion 2 entangles the second qubit with the vibrational mode and ion 1, resulting in the state $(|D\rangle \otimes (|SS, 1\rangle - |DD, 0\rangle))/\sqrt{2}$. Up to this point the state of ion 3 is still separable. The final two pulses on ion 3 transfer the entanglement from the vibrational mode to ion 3, such that the GHZ state $-((|SSS\rangle + i|DDD\rangle)/\sqrt{2} \otimes |n = 0\rangle))$ is obtained. The vibrational mode returns to its ground state and is again separable from the ions' internal states.

9.2.2. Preparation of W-states

As in the case of the preparation of the GHZ-state, the ion string is assumed to be initially prepared in the $|SSS, 0\rangle$ state. The pulse sequence to prepare three ionic qubits in a W state
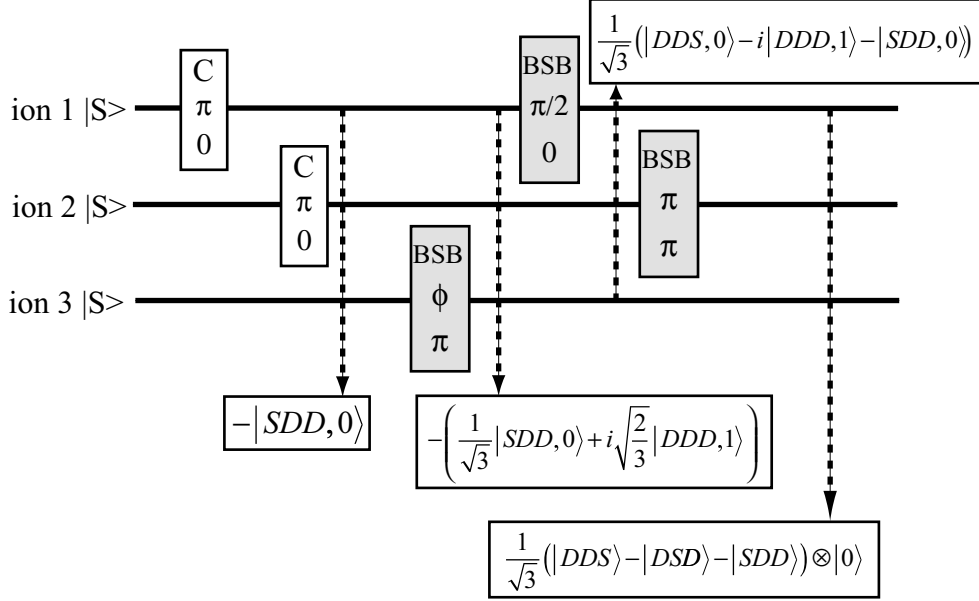
Figure 9.2.: Pulse sequence for the preparation of an ion string of three ions in the W-state $\Psi\rangle = 1/\sqrt{3}(|\text{DDS}\rangle - |\text{DSD}\rangle - |\text{SDD}\rangle)$. For certain times the intermediary state of the qubits is shown.

is as follows:

$$U_W = R_2^+ \left(\pi, \pi\right) R_1^+ \left(\frac{\pi}{2}, 0\right) R_3^+ \left(2 \arccos(1/\sqrt{3}), \pi\right) R_2 \left(\pi, 0\right) R_3 \left(\pi, 0\right). \tag{9.4}$$

This pulse sequence, also shown in Fig. 9.2, contains only five pulses and takes less time than the pulse sequence for GHZ-states. The first two carrier pulses on ions 1 and 2 prepare the ion string in the state $-|SDD, 0\rangle$. The subsequent blue sideband pulse of length $2\arccos(1/\sqrt{3})$ transfers the ion string to the state $-(1/\sqrt{3}|SDD, 00\rangle + i\sqrt{2/3}|DDD, 1\rangle)$. The final blue sideband pulses on ions 1 and 2 leave the ion string in the W state $1/\sqrt{3}(|DDS\rangle - |DSD\rangle - |DDS\rangle)$, which is equivalent to the W-state shown in Eq. 9.2.

9.3. Experimental results: Preparation of GHZ- and W-states

In order to generate GHZ- and W-states the string of three ions was prepared in the same way as in previous experiments with Bell states and the controlled-NOT gate. A three-ion crystal has three axial vibrational modes, i.e. the center-of-mass mode, the breathing mode and the "Egyptian" mode (cf. Sec. 3.3). Following the line of reasoning explained in the previous chapters it would be favorable to use the mode with highest frequency as "bus" mode, i.e. the Egyptian mode, to avoid off-resonant excitation of the carrier when driving sideband transitions. However, it turned out, that better results where achieved, when using the center-of-mass vibrational mode at a frequency of $\omega_{\text{com}} = 2\pi \cdot 1.2$ MHz from the carrier[2].

---

[2]Further measurements showed that the coherence time of a superposition of vibrational states is much lower for the Egyptian and the breathing mode compared to the center-of-mass mode. This behavior is not
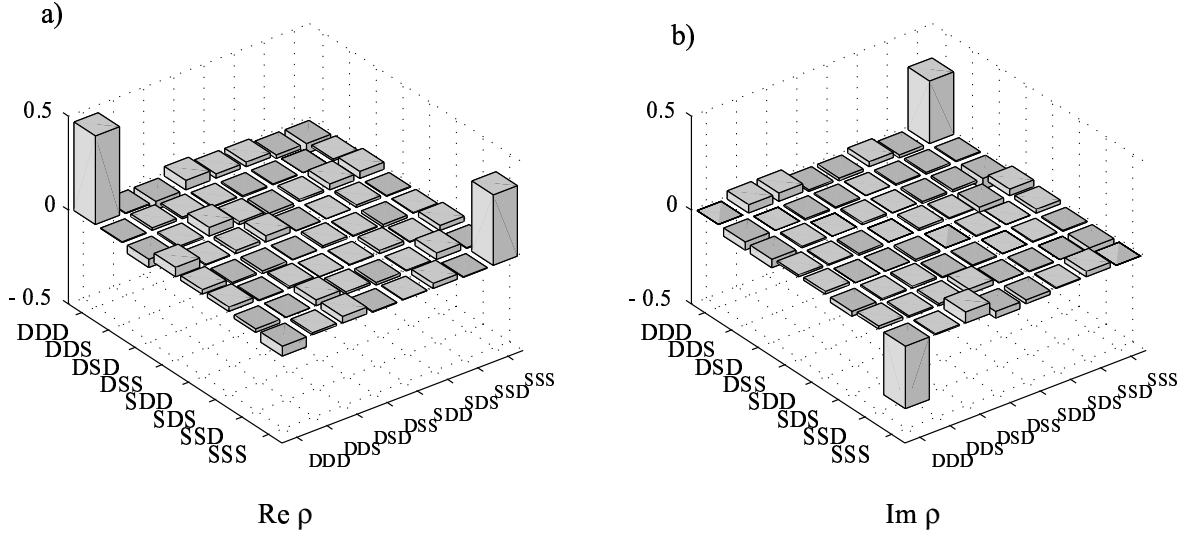
a)

b)

Re ρ   Im ρ

Figure 9.3.: Density matrix of a state produced by the pulse sequence U_{GHZ} (cf. 9.3) obtained by quantum state tomography. The state expected to be generated by this pulse sequence is $\psi_{\text{ideal}} = -(|SSS\rangle + i|DDD\rangle)/\sqrt{2}$. The measured density matrix shows the corresponding characteristics, including imaginary off-diagonal elements caused by the relative phase of $\pi/2$ between the superposed states.

Therefore this mode was chosen for all experiments presented in this chapter. The center-of-mass mode was cooled to its ground state via Doppler cooling followed by sideband cooling. After laser cooling each ions was initialized in its $|S\rangle$ ground-state. The pulse sequences shown in the previous section were applied. The Rabi frequency for carrier transitions was adjusted to $\Omega_{\text{carrier}} = 2\pi \cdot 50$ kHz and the Rabi frequency of the blue sideband set to $\Omega_{\text{blue}} = 2\pi \cdot 4$ kHz. The length of the complete GHZ-state pulse sequence amounted to about 650 μs whereas the W-state pulse sequence took only about 300 μs.

In order to gain complete information about the outcome of the pulse sequences, quantum state tomography was used to obtain the density matrices of the generated states ρ_{exp}. In Fig. 9.3 the real and imaginary part of a density matrix ρ_{exp} of a state generated by our GHZ pulse sequence is shown. The overlap or fidelity $F = \langle\psi_{\text{ideal}}|\rho_{exp}|\psi_{\text{ideal}}\rangle$, where $|\Psi_{\text{ideal}}\rangle = -1/\sqrt{2}(|DDD\rangle + i|SSS\rangle)$ is the ideally expected state, was calculated. For the density matrix shown in Fig. 9.3 the fidelity was calculated to be $F = 76(2)\%$[3].

In Fig. 9.4 the density matrix of a state produced by our W-state pulse sequence is shown. The fidelity with respect to the ideal state $\Psi_{\text{ideal}} = (|SDD\rangle - |DSD\rangle - |DDS\rangle)/\sqrt{3}$ was calculated to be $F = 83(3)\%$.

---

expected and is still investigated.

[3] Here, the statistical uncertainty is caused by quantum projection noise due to the finite size of the sets of data taken for the quantum state tomography. The statistical error was calculated using Monte-Carlo simulations (cf. A.2)
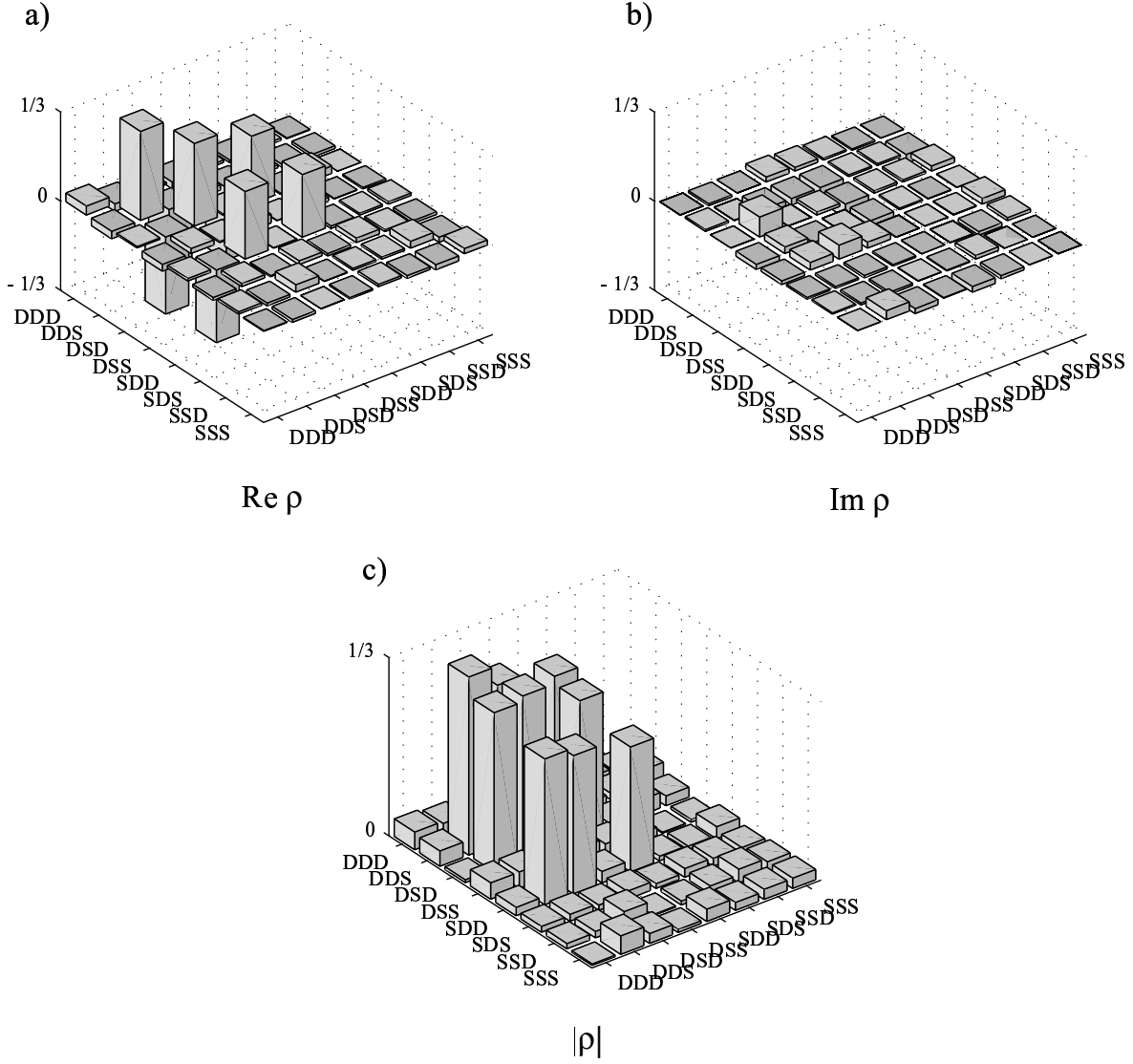
Figure 9.4.: Measured density matrix of a W-state generated by the pulse sequence in Eq. . This density matrix fits well to the expected output state $\psi_{ideal} = 1/\sqrt{3}(|SDD\rangle - |DSD\rangle - |DDS\rangle)$, the calculated overlap is F=83(3)%. Off-diagonal matrix elements belonging to coherent superpositions of the $|DDS\rangle$ state with $|DSD\rangle$ and $|SSD\rangle$ are as expected negative. The real and imaginary part of the density matrix are shown in a) and b), respectively. Since two of the off-diagonal elements belonging to coherent superpositions are not visible in a) the absolut value of the density matrix is shown in c).

9.4. Experimental results: Lifetime of GHZ- and W-states

Just as in the experiments in Sec. 7.4 with Bell states, the fact that we are able to prepare tripartite entangled states enabled us to investigate the lifetime of these states.

In order to monitor the time evolution of the entangled states, a waiting time τ was inserted before the pulses for the quantum state tomography were applied. This kind of measurement was done with two kinds of GHZ-states, namely $|\text{GHZ1}\rangle = (|\text{SSS}\rangle + i|\text{DDD}\rangle)\sqrt{2}$ and $|\text{GHZ2}\rangle = (|\text{SDD}\rangle + |\text{DSS}\rangle)/\sqrt{3}$, and the W-states shown in the previous section. All three states are expected to have different lifetimes or inherent stability against correlated phase fluctuations. W-states are invariant against this kind of noise, which can be easily proven by substituting $|S\rangle \rightarrow e^{-\alpha/2}|S\rangle$ and $|D\rangle \rightarrow e^{+\alpha/2}|D\rangle$ in $|W\rangle = (|\text{DSS}\rangle - |\text{SDS}\rangle - |\text{SSD}\rangle)\sqrt{3}$ for all ions. The same substitution in the GHZ-state $|\text{GHZ1}\rangle = (|\text{SSS}\rangle + i|\text{DDD}\rangle)\sqrt{2}$ will change the relative phase of the superposed states by 3α. Therefore these GHZ-states are expected to be highly sensitive to dephasing. However, the other kind of GHZ states $|\text{GHZ2}\rangle = (|SDD\rangle + |DSS\rangle)/\sqrt{2}$ are expected to be roughly three times more stable, since the dephasing on two of the three qubits will cancel.

The fidelity $F(\tau) = \langle\text{GHZ}|\rho(\tau)|\text{GHZ}\rangle$ is shown in Fig. 9.5a). Additionally, in Fig. 9.5b) the normalized height of the non-diagonal elements of the density matrix are shown, which indicate coherent superpositions of $|\text{SSS}\rangle$ and $|\text{DDD}\rangle$ or $|\text{SDD}\rangle$ and $|\text{DSS}\rangle$ in case of the GHZ-state $|\text{GHZ2}$. The height of these off-diagonal elements and therefore the fidelity as well, decreases with increasing waiting time, indicating that the entangled states decay into a statistical mixture. A Gaussian $\sim \exp(-\tau^2/\tau_0^2)$ was fitted to the height of the non-diagonal elements of the density matrix. In case of the $|\text{GHZ1}\rangle$-states the decay time was determined to be $\tau_0 = 0.9(3)$ ms, while for the $|\text{GHZ2}\rangle$-states the decay time obtained was $\tau_0 = 2.3(4)$ ms. The two lifetimes differ by a factor of 2-3 which is expected.

The results for W-states $|W\rangle = (|SSD\rangle - |SDS\rangle - |DSS\rangle)/\sqrt{3}$ are shown in Fig. 9.6. Again the fidelity $F(\tau)$ and and the mean of the absolute value of the six off-diagonal element, which correspond to coherent superpositions within the W-state (see Fig. 9.4) are shown. In order to show the difference between the lifetime of GHZ- and W-states, the results from Fig. 9.5 for the $|\text{GHZ2}\rangle$-states are shown again. The waiting time was increased to 40 ms, during which the loss of fidelity for the W-states was only about 20 %, whereas the GHZ-states already decay into a statistical mixture in less than 3 ms. This demonstrates the inherent stability of the W-states against correlated dephasing. A proper fit of a Gaussian to the data is not possible, since data points at even larger waiting times would be necessary in order to do so.

9.5. Partial measurement of GHZ- and W-states

9.5.1. General remarks

Being able to generate both types of tripartite entangled states, it is intriguing to investigate the effect of a measurement of one of the involved qubits on the entangled states. The two classes of tripartite entangled states are expected to behave differently if one of the qubits is subjected to a projective measurement in the $\{|S\rangle, |D\rangle\}$ basis. Suppose a measurement is
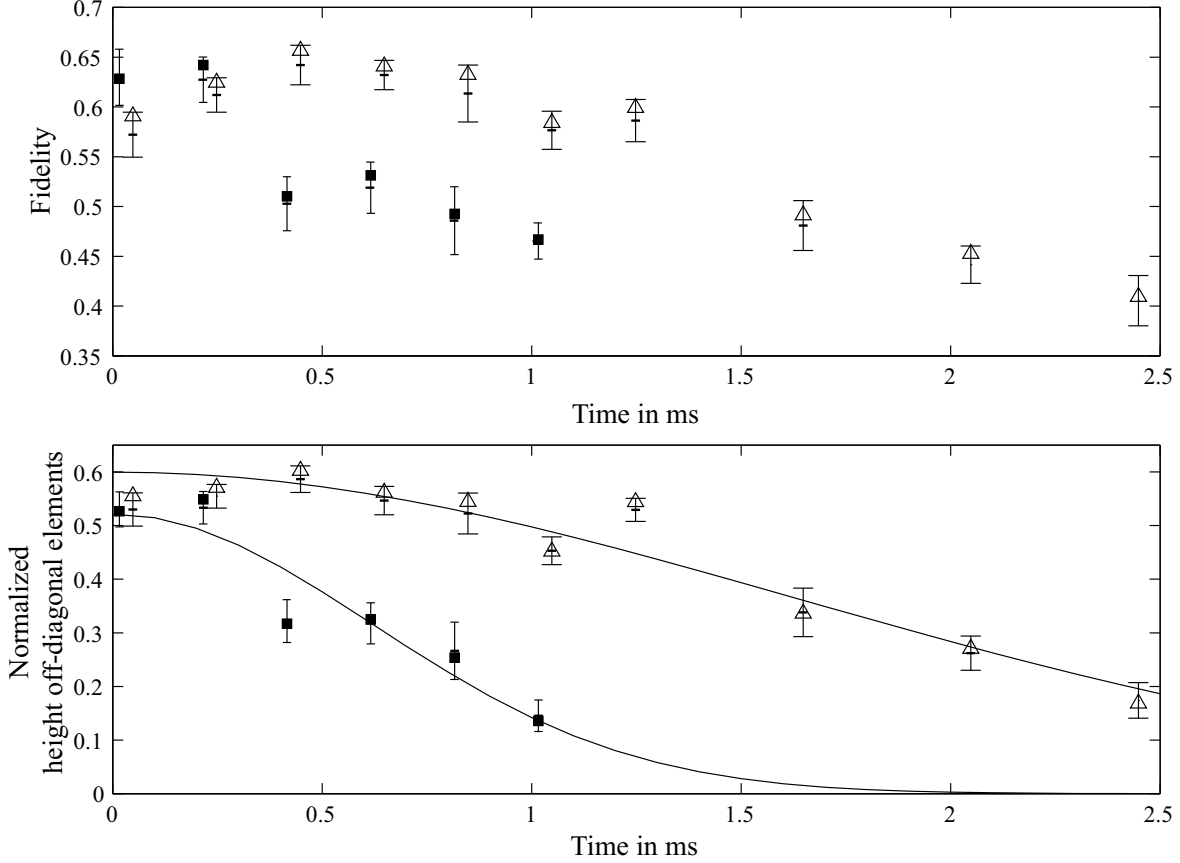
Figure 9.5.: Time evolution of the GHZ-states $(|\text{GHZ1}\rangle = |SSS\rangle + i|DDD\rangle)/\sqrt{2}$ (squares) and $|\text{GHZ2}\rangle = (|SDD\rangle + |DSS\rangle)/\sqrt{2}$ (triangles). In a) the fidelity $F(\tau) = \langle\text{GHZ}|\rho(\tau)|\text{GHZ}\rangle$ is shown, where $\rho(\tau)$ is the measured density matrix after a waiting time τ. b) Mean of the absolute value of the off-diagonal elements of the density matrix $\rho(\tau)$. The measured values are normalized to the ideal value of $1/2$. The solid curves show fits of the data with a Gaussian $\sim e^{-(\tau/\tau_0)^2}$. For the GHZ-states $|\text{GHZ1}\rangle$ the decay time was determined to be $\tau_0 = 0.9(3)$ ms and for the GHZ-state $|\text{GHZ2}\rangle$ the decay time $\tau_0 = 2.3(4)$ ms was obtained. In both figures the given error bars are the quantum projection noise, which is due to the finite number of experiments (n=5400) taken for every point of data. The error bars were determined using Monte-Carlo simulations as described in A.4. The error bars are centered around the mean value of the fidelity of the simulated density matrices, which is indicated by small horizontal bars.
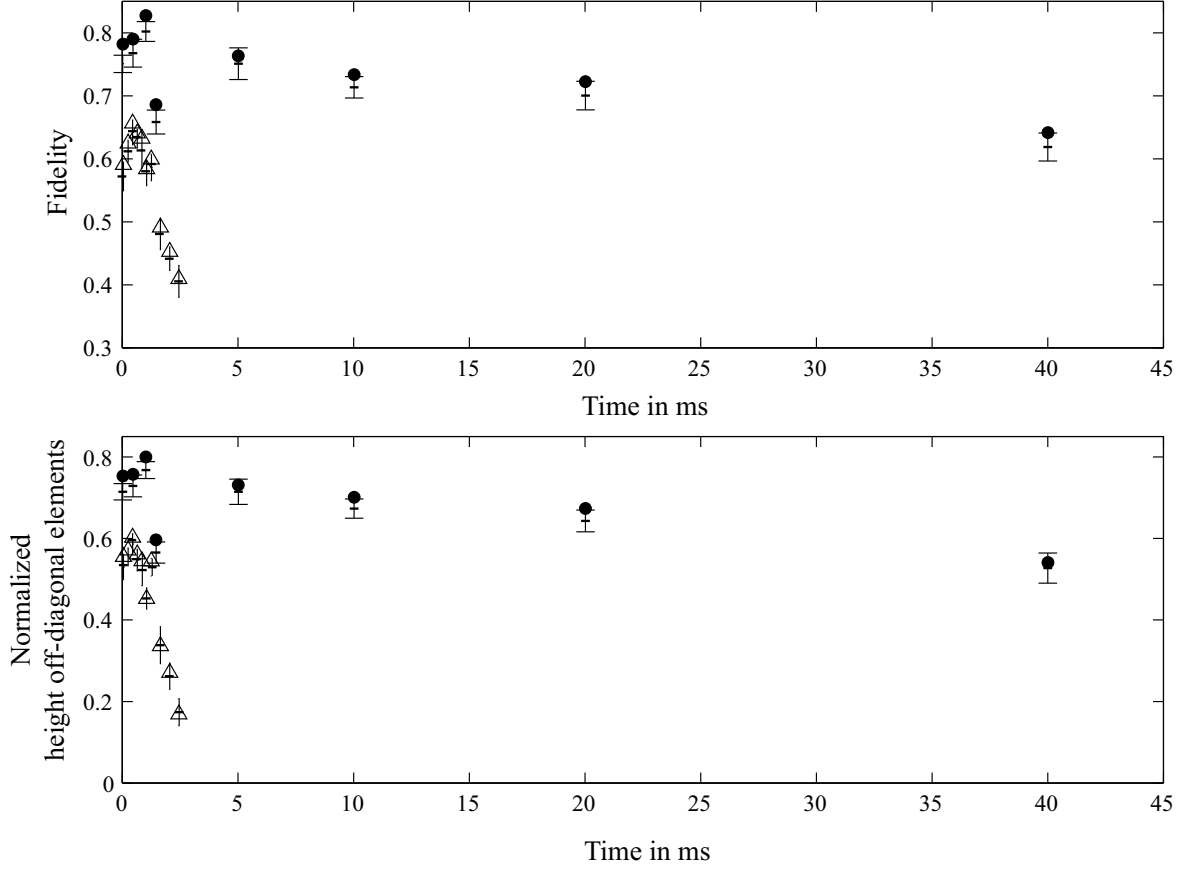
Figure 9.6.: Time evolution of W-states. In a) the fidelity $F(\tau) = \langle W|\rho(\tau)|W \rangle$ is shown. b) Mean of the absolute value of the six off-diagonal elements $|DDS\rangle\langle DSD|$, $|DDS\rangle\langle SDD|$ and $|DSD\rangle\langle SDD|$ and the corresponding hermitian conjugated elements. In order to compare the lifetimes of GHZ- and W-states the lifetime data for $|GHZ2\rangle$ is shown again. The values are normalized to the ideal values, i.e. 1/2 for the GHZ-states and 1/3 for the W-states. The error bars represent the statistical error due to quantum projection noise, whose magnitude is determined by the number of experiments (n=5400) taken for every data point. The error bars were determined using Monte-Carlo simulations as described in A.4. The error bars are centered around the mean value of the fidelity of the simulated density matrices, which is indicated by small horizontal bars.

performed on the first qubit, then the following behavior is expected:

$$\rho_{\text{GHZ}} = |\text{GHZ}\rangle\langle\text{GHZ}| \xrightarrow{\text{measure qubit 1}} \frac{1}{2}\left(|DDD\rangle\langle DDD| + |SSS\rangle\langle SSS|\right)$$

$$\rho_{\text{W}} = |\text{W}\rangle\langle\text{W}| \xrightarrow{\text{measure qubit 1}} \frac{2}{3}|\psi\rangle\langle\psi| + \frac{1}{3}|DDS\rangle\langle DDS|$$

$$\text{where} \quad \psi = (|SD\rangle + |DS\rangle)|0\rangle. \tag{9.5}$$

Here, the states $|\text{GHZ}\rangle$ and W$\rangle$ are those defined in Eq. 9.1 and 9.2. In both cases the quantum state after measurement is described by a mixed state. In case of the GHZ-state the qubits will be found with equal probability in $|DDD\rangle$ or $|SSS\rangle$. The resulting mixed state is no longer entangled. For the W-state the situation is different: The qubits are left in a mixed state, but with a probability of 2/3 the state $(|SD\rangle + |DS\rangle)|0\rangle$ is obtained in which two of the qubits are still entangled.

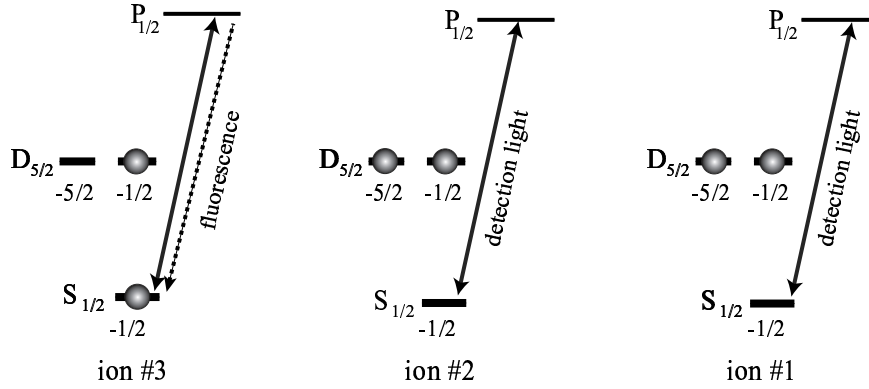### 9.5.2. Partial read-out of ion strings

Figure 9.7.: Scheme for partial measurement of an ion string. The populations of the $S_{1/2}(m = -1/2)$ states of ions 1 and 2 are coherently mapped to the $D_{5/2}(m = -5/2)$ states. Potential superpositions of $S_{1/2}(m = -1/2)$ and $D_{5/2}(m = -1/2)$ are now superpositions of $D_{5/2}(m = -5/2)$ and $D_{5/2}(m = -1/2)$. If light at 397 nm is applied, only ion 3 is measured and projected onto either the $S_{1/2}$- or $D_{5/2}$-state. The quantum states of ion 1 and 2 are unaffected by the 397 nm light.

In order to implement an experiment as described in the previous paragraph the ability to perform a measurement on one of the qubits while preserving the quantum state of the others is a prerequisite. In the case of our ion trap implementation measurements are done by scattering light at 397 nm at the $S_{1/2} \leftrightarrow D_{5/2}$ transition. Since in principle only one scattering event is sufficient to destroy possible coherent superpositions of qubits and since in our experimental setup the whole ion string is illuminated by the laser beam at 397 nm, it is necessary to protect qubits from the influence of the 397 nm light. Here, the fact that the 397 nm light couples only to the S-ground state but not to the D-state can be used to our advantage. By exciting the transition $S_{1/2}(m = -1/2) \leftrightarrow D_{5/2}(m = -5/2)$ with a pulse of length $\pi\Omega$,

superpositions of the $S_{1/2} - D_{5/2}(m = -1/2)$ type are transformed into superpositions of the type $D_{5/2}(m = -5/2) - D_{5/2}(m = -1/2)$. In this way quantum information is temporarily stored in the D sub-levels, which are not affected by the 397 nm laser light. This is depicted in Fig. 9.7, where the quantum information in ion 1 and 2 is "hidden" in the $D' - D$ sub-levels, where D' and D denote the $D_{5/2}(m = -1/2)$ and $D_{5/2}(m = -5/2)$ states respectively, while the quantum state of ion 3 is measured by scattering 397 nm light. After completion of this measurement, superpositions in the $D' - D$ sub-levels can be transformed back to $S - D$-superpositions by another pulse on the $S_{1/2}(m = -1/2) \leftrightarrow D_{5/2}(m = -5/2)$ of length $\pi\Omega$. The required time for writing the quantum information back and forth from $S - D$ to $D' - D$ is usually only a few tens of microseconds, since only carrier transitions are involved.

A problem arises from the fact that the shift of the levels relative to each other due to the Zeeman effect is six times larger for the $D' - D$ levels than for the $S - D$ levels. Therefore, magnetic field fluctuations will affect the coherence of $D' - D$ superpositions far more than $S - D$ superpositions. However, the effect of magnetic field fluctuations on a time scale greater than or equal the length of one experimental cycle (20-40 ms) can be cancelled by employing the spin-echo technique (cf. Sec. 6.5.4).
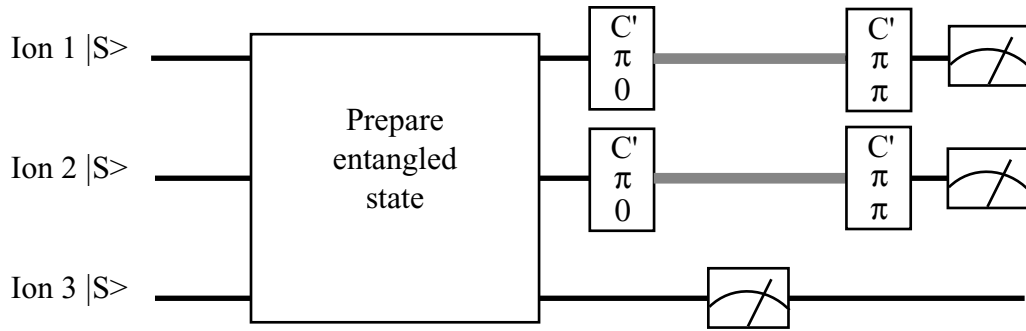
9.5.3. Experimental results

Figure 9.8.: Pulse sequence in order to investigate the effect of a measurement of one ion on an entangled states of three ions. First the three ions are entangled using the pulse sequences shown in Fig. 9.1 and 9.2. While ion 3 is projected by a measurement, the quantum states of ions 1 and 2 are stored in a superposition of the levels D' and D, indicated by grey lines. The transfer from S to D' is done by pulses on the carrier transition $S_{1/2} \leftrightarrow D_{5/2}(m = -5/2)$. In the diagram these carrier pulses are indicated by C'.

In order to investigate the effect of a measurement on GHZ- and W-states and to demonstrate the technique introduced in the previous section, the following experiment was carried out (cf. Fig. 9.8): First three ion qubits were prepared in GHZ- or W-states using the pulse sequences introduced in Sec. 9.2. Then laser pulses were applied to qubits 1 and 2 to transfer their quantum state from the $S - D$ to the $D' - D$ manifold. A measurement of qubit 3 was carried out by scattering light at 397 nm. Finally, the quantum state of qubits 1 and 2 was transferred back to the $S - D$-manifold and the quantum state of the three qubits was

determined by quantum state tomography. In Fig. 9.9 the measured density matrices of a
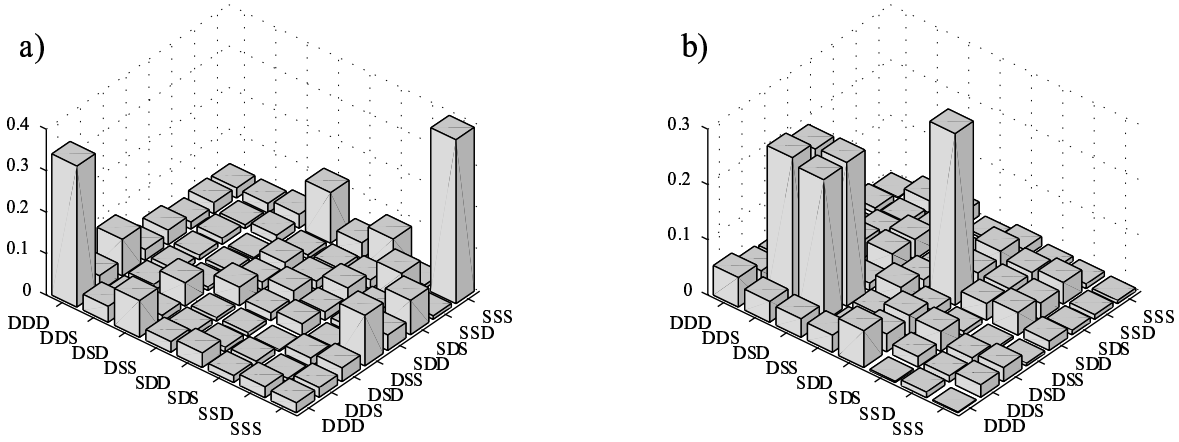

Figure 9.9.: Measured density matrices of three entangled qubits after qubit was projected by a measurement. In a) the density matrix for a GHZ-state and in b) that for a W-state are shown. Off-diagonal elements corresponding to coherent superpositions of qubit 3 with the other qubits disappear in both cases. In the case of the GHZ-state all off-diagonal elements vanish, whereas in the case of the W-state off-diagonal elements corresponding to superpositions of ion 1 and ion 2 are preserved.

GHZ-state in (a) and a W-state (b) after ion 3 was subjected to a measurement are shown. In the case of the GHZ-state a comparison with the density matrix without a measurement on ion 3 in Fig. 9.3 shows that the off-diagonal elements $|SSS\rangle\langle DDD|$ and $|DDD\rangle\langle SSS|$ vanished. This is expected, since the ion string is no longer in a coherent superposition of $|SSS\rangle$ and $|DDD\rangle$ after the measurement but a mixture of these states. For the W-state the result is different. All off-diagonal elements corresponding to superpositions where ion 3 is involved have vanished. However, the non-diagonal elements belonging to superpositions of ions 1 and 2 are still present after the measurement, leaving those ions with a probability of 2/3 of being in a Bell state $(|SD\rangle + |DS\rangle)/\sqrt{2}$.

If information is available about the state into which state ion 3 was projected, the state of the other two ions is completely determined. To prove this, the time during which light at 397 nm was scattered by ion 3 was increased to 500 μs, such that by collecting the fluorescence light of the ion with our PMT, it was possible to determine the state into which ion 3 was projected. In Fig. 9.10(a) a histogram of the photon counts measured with the PMT is shown. Here the peak centered around 10 counts per 500 μs corresponds to events where ion 3 was projected into the $|D\rangle$ state while the peak centered around 40 counts per 500 μs corresponds to events where it was projected into the $|S\rangle$ state. The threshold which discriminates between the two cases was set to 20 counts. Ion 3 is observed in state $|D\rangle$ in 65(2) % of the cases complying with the expected probability of 2/3. Using the information about the state of ion 3 the experimental results were sorted and for both cases the resulting reduced density matrix of ions 1 and 2 was reconstructed. For the cases where ion 3 was found in $|S\rangle$ the density matrix in Fig. 9.10(b) is obtained, which shows that ions 1 and 2 are projected into the $|DD\rangle$

state. The density matrix of ions 1 and 2 for the case where ion 3 was projected into the $|D\rangle$ state is shown in Fig. 9.10(c). As expected ion 1 and 2 are projected into a Bell state, whose fidelity was calculated to be 75%.
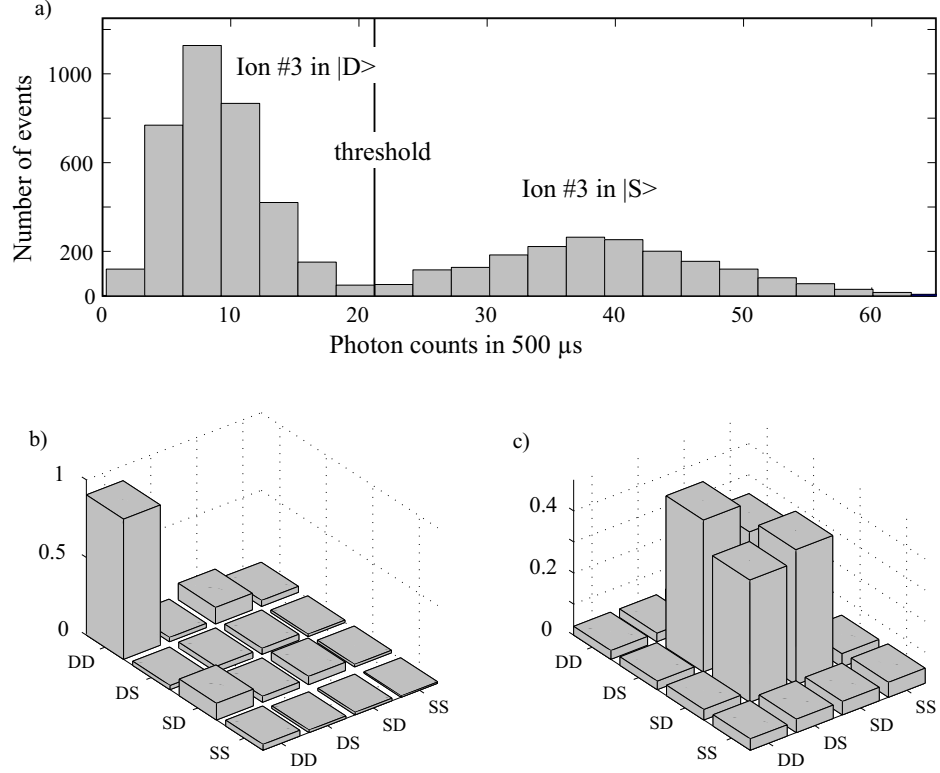

Figure 9.10.: a) Histogram of the photons counted with the PMT during 500 μs of measuring ion 3. The peaks centered around 10 and 40 counts per 500 μs correspond to events where ion 3 was projected into state $|D\rangle$ or $|S\rangle$, respectively. The subsets of data belonging to either one of the two cases - ion 3 in $|S\rangle$ or $|D\rangle$ - were used to reconstruct the reduced density matrix containing only the information about the states of ions 1 and 2. b) Reduced density matrix for the case that ion 3 was found in $|S\rangle$. c) Reduced density matrix for the cases where ion 3 was projected into $|D\rangle$.

The ability to perform a measurement on a part of a register of qubits and use the obtained result to choose an appropriate operation for the rest of the qubits is an important part of quantum algorithms like error-correction, quantum teleportation and entanglement swapping. In order to demonstrate this ability the following experiment was carried out: A GHZ-state of the kind $|\psi\rangle = 1/\sqrt{2}(|DSD\rangle + i|DSS\rangle)$ was prepared[4]. The third ion was then rotated by

---

[4]This kind of GHZ-state can be generated by using the pulse sequence $U = R_1(\pi, 0)R_1^+(\pi, 0) \cdot U_{\text{CNOT}}^{32} \cdot R_3^+(\pi/2, 0)$.

a carrier pulse $R_3(\pi/2, \pi)$, such that the following state was obtained:

$$|\psi\rangle = -\frac{1}{2}\left(|D\rangle\left(|DS\rangle + |SD\rangle\right) + i|S\rangle\left(|DS\rangle - |SD\rangle\right)\right). \qquad (9.6)$$

A measurement of ion 3 was carried out, while the quantum states of ions 1 and 2 were stored in the $D' - D$ levels. Ion 3 is projected with equal probability into the $|D\rangle$ or $|S\rangle$ state, whereas ion 1 and 2 are projected into the $(|DS\rangle + |SD\rangle)/\sqrt{2}$ state or $(|DS\rangle - |SD\rangle)/\sqrt{2}$, respectively. The measured density matrix corresponding to this state is shown in Fig. 9.11(a). We intended to transform this state into the pure state $|S\rangle \otimes (|DS\rangle - |SD\rangle)$. Therefore, whenever the state of ion 3 was found to be $|D\rangle$, the states of ions 1 and 2 were mapped by the pulse sequence $U = R_1(\pi, \pi/2)R_1(\pi, 0)$ from $(|DS\rangle + |DS\rangle)/\sqrt{2}$ to $(|DS\rangle - |DS\rangle)/\sqrt{2}$ and ion 3 was transferred from $|D\rangle$ to $|S\rangle$ by a pulse $R_3(\pi, 0)$, such that we obtain the desired pure state. In Fig. 9.11(b) the density matrix measured after applying these reconstruction operations is shown.

This experiment demonstrates our ability to measure a part of an register of qubits and to apply operations to the other qubits, depending on the result of this measurement. This technique is a fundamental building block in more complex experiments as quantum teleportation and error correction. The experimental implementation of quantum teleportation will be discussed in the following chapter. It has to be pointed out that our ability to apply operations after a measurement is so far restricted to carrier pulses. During the measurement the ion string is heated up to the Doppler limit by the 397 nm photons scattered by the ions. The state of the vibrational COM mode will thus be a thermal state with a mean phonon population of $\langle n \rangle = 20$. Under these conditions carrier pulses of high accuracy are still feasible, since the Rabi frequency of carrier transitions depends only weakly on the phonon number. However, operations like a controlled-NOT or a phase gate, which require the vibrational mode to be in the ground state, cannot be executed. It would be necessary to cool down the relevant vibrational mode to the ground state once more.
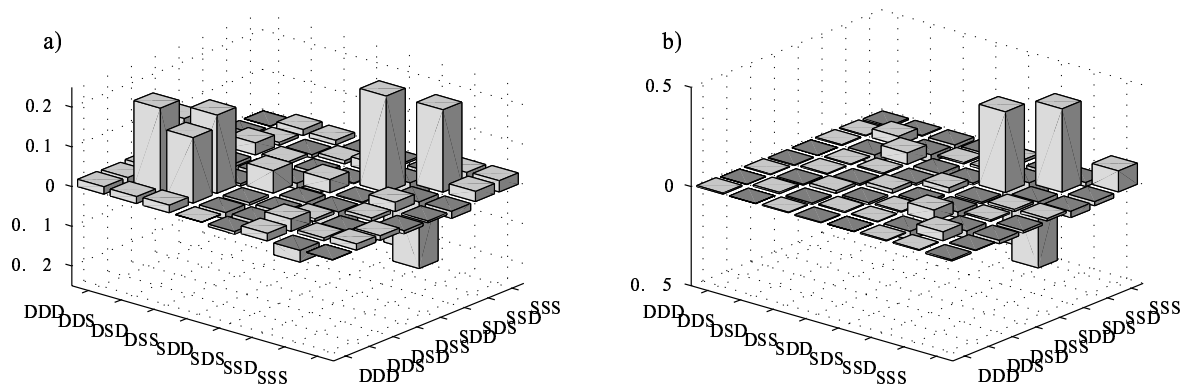
Figure 9.11.: Density matrices illustrating a measurement of ion 3, which depends on the result of the measurement followed by a subsequent rotation of ions 1 and 2. a) Real part of the density matrix of a GHZ state, after measurement of ion 3 in a rotated basis. As can be seen from the density matrix the ion string is left in a mixed state. Ions 1 and 2 are found in two different Bell states, depending on whether ion 3 was found in the $|S\rangle$ or $|D\rangle$ state. In the latter case carrier pulses are applied to ions 1 and 3. This way the ion string is prepared in a pure Bell state again, whose density matrix - only the real part is shown - can be seen in b). Please note the different scaling of the y-axis in a) and b).

10. Quantum Teleportation

10.1. Introduction

Suppose a person called Alice is in possession of a quantum state or qubit $|\psi\rangle$ unknown to her which she wants to transfer to another person called Bob. However, Alice and Bob have no quantum channel available through which they can directly transfer the quantum state[1]. Alice might be tempted to try to gain information about $|\psi\rangle$ by subjecting it to a measurement and transfer the obtained information to Bob via a classical communication channel. But this approach would not succeed, since Alice would only obtain one bit of information by measuring the quantum state in her possession. However, it would require measurements on an infinite ensemble of copies of the quantum state $|\psi\rangle$, producing an infinite amount of classical information in order to gain complete information about $|\psi\rangle$.

In 1993 Bennett et al. proposed a scheme which allows Alice and Bob to faithfully transfer quantum information [12]. They called this scheme *teleportation*. The major steps of this scheme are depicted in Fig. 10.1. Bennett et al. assumed that Alice and Bob each have one particle of an entangled pair of particles, which is the necessary quantum resource Alice and Bob need to transfer a quantum state. Alice performs a measurement of the unknown quantum state and her part of the entangled pair of particles in the Bell basis (cf. Sec. 2.4.2). Due to the nonlocal properties of the entangled state, Bob's part of the entangled pair will be projected into a state which turns out to be the original state $|\psi\rangle$ modulo an additional rotation. If Alice conveys the results of her Bell-measurement to Bob via a classical communication channel, Bob has the necessary information to apply the suitable operation, which recovers the original quantum state.

The first experimental demonstration of teleportation was realized by Bouwmeester et al. in 1997 [14]. They used a pair of polarization-entangled photons created by parametric down-conversion and another photon to carry the initial quantum state encoded in the photon's polarization. However, this first experiment lacked a complete Bell-measurement: Only one of four Bell states could be detected. In further experiments this limitation was overcome by using more complex optical setups. Boschi et al. for instance implemented teleportation by generating a path-entangled pair of photons, which at the same time carried the input state for teleportation encoded in their polarization. Their setup allowed them to implement a complete Bell-measurement [15]. Another approach was pursued by Kim et al. who also used polarization-entangled photons but implemented a Bell-measurement using nonlinear optical elements. This allowed them to discriminate between all four possible Bell states but decreased the rate at which teleportation events were detected significantly [101]. Although all four Bell

---

[1] A quantum channel would be a quantum system which Alice and Bob use to exchange quantum information. An example of such a channel could be the polarization of a photon onto which the unknown quantum state could be swapped and sent to Bob, who would then swap the quantum information onto one of his qubits
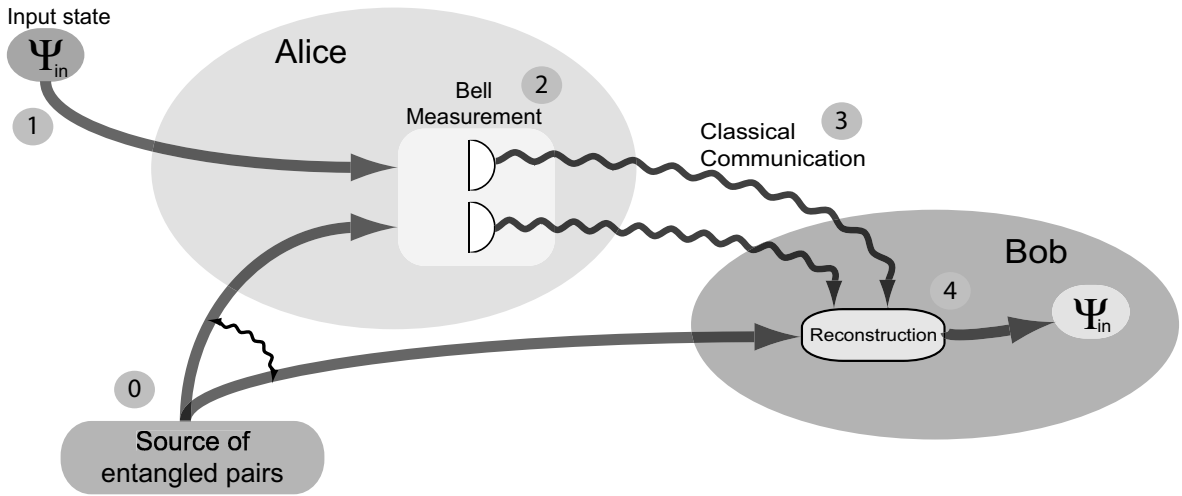
Figure 10.1.: Bennet et al.'s proposal to teleport an unknown quantum state [12]. An unknown quantum state is to be transferred from Alice to Bob. Alice and Bob share one part of a maximally entangled pair of particles. Alice carries out a projective measurement in the Bell basis, whose results she communicates to Bob via a classical channel. Depending on this information, Bob selects the suitable operation to reconstruct the input state in his part of the entangled pair.

states could be detected, the final step of reconstructing the input state by an operation conditioned by the result of the Bell-measurement, was omitted in these experiments. Successful teleportation events had to be established by selecting the data after completion of the experiment, searching for the subset of data where the outcome of the Bell-measurement and a preset reconstruction operation did match, i.e. teleportation was performed post-selectively.

Teleportation was also demonstrated for other physical systems. Teleportation of the quantum state of a continous system, was realized by Furusawa et al. who teleported an optical coherent state [16]. In another experiment teleportation was simulated using liquid-state nuclear magnetic resonance [17]. A teleportation experiment similar to the one presented in this chapter was realized by Barrett et al. , who used three $^9\text{Be}^+$ ions in a segmented ion trap to implement the teleportation algorithm [102].

10.2. Teleporting an Unknown Quantum State

In this section the teleportation scheme shown in Fig. 10.1 is investigated step-by-step. First we assume the source of entangled pairs provides the Bell state:

$$|\Psi_+\rangle_{\text{AB}} = \frac{1}{\sqrt{2}} \left(|0\rangle_{\text{A}}|1\rangle_{\text{B}} + |1\rangle_{\text{A}}|0\rangle_{\text{B}} \right), \qquad (10.1)$$

where the subscripts indicate whether the qubit belongs to Alice's or Bob's subsystem. Suppose the unknown quantum state is given by $|\psi_{\text{in}}\rangle_{\text{A}} = (\alpha|0\rangle + \beta|1\rangle)/\sqrt{2}$. The complete

quantum state of all three qubits in the system is given by:

$$|\Psi\rangle_{AB} = \frac{1}{2} \left(\alpha|0\rangle_B|00\rangle_A + \beta|1\rangle_B|10\rangle_A + \alpha|1\rangle_B|01\rangle_A + \beta|1\rangle_B|10\rangle_A \right). \qquad (10.2)$$

The basis states $\{|00\rangle, |01\rangle, |10\rangle, |11\rangle\}$ can be expressed using the Bell states (cf. Eq. 2.18), such that Eq. 10.2 becomes:

$$|\Psi\rangle_{AB} = \frac{1}{\sqrt{8}} [\, (\alpha|1\rangle + \beta|0\rangle)_B \, |\Phi_+\rangle_A + (\alpha|1\rangle - \beta|0\rangle)_B \, |\Phi_-\rangle_A$$
$$+ (\alpha|0\rangle + \beta|1\rangle)_B \, |\Psi_+\rangle_A + (-\alpha|0\rangle + \beta|1\rangle)_B \, |\Psi_-\rangle_A],$$

and by using the Pauli operators X and Z we finally obtain:

$$= \frac{1}{\sqrt{8}} [X|\psi_{\text{in}}\rangle_B \otimes |\Phi_+\rangle_A + XZ|\psi_{\text{in}}\rangle_B \otimes |\Phi_-\rangle_A |\psi_{\text{in}}\rangle_B \otimes |\Psi_+\rangle_A - Z|\psi_{\text{in}}\rangle_B \otimes |\Psi\rangle_A]. \qquad (10.3)$$

A projective measurement of Alice in the Bell-basis projects the qubit in Bob's possession with equal probability into the states $X|\psi_{\text{in}}\rangle$, $XZ|\psi_{\text{in}}\rangle$, $|\psi_{\text{in}}\rangle$ and $Z|\psi_{\text{in}}\rangle$. It is noteable, that at this point neither Alice nor Bob own enough information to recover the input state. Both possess only random information. Only if Alice communicates the result of her Bell-measurement to Bob, does he know which operation to apply in order to reconstruct $|\psi_{\text{in}}\rangle$. Therefore the information transfer in teleportation is not taking place instantaneously at the moment of Alice's measurement, which would violate one of the cornerstones of the theory of relativity, i.e. that no signal can travel faster than the speed of light. The information transfer is not complete until Alice and Bob have finished their classical communication, which is limited by the speed of light.

10.3. Quantum state transfer without entanglement vs. teleportation

In the previous section the protocol of teleportation was outlined. Provided Alice and Bob share a maximally entangled pair of particles and a classical communication channel it was shown, that they can transfer a quantum state, without loss of information. The question to be investigated in this section will be: In terms of fidelity, how well can Alice and Bob transfer a quantum state without a maximally entangled pair at hand, using only the classical channel? The answer to this question gives a mean fidelity $\mathcal{F}_{\text{lim}}$, averaged over the distrubution of possible input states. This mean fidelity is important in the context of experimental realizations of teleportation. Due to inevitable experimental imperfections, the overlap of Alice's input state $|\psi_{\text{in}}\rangle$ and Bob's reconstructed state ρ^{out}, i.e. the fidelity $F_{\text{exp}} = \langle\psi^{\text{in}}|\rho^{\text{out}}|\psi^{\text{in}}\rangle$, is expected to be less than one. However, it is necessary to achieve a fidelity above the threshold $\mathcal{F}_{\text{lim}}$ to prove that the obtained result can only be explained by the action of teleportation and not by any other strategy Alice and Bob might have used. The question raised above has been adressed by various authors (c.f. [103–105]). Here, mainly the results will be discussed. Technical details about how the thresholds can be calculated are explained in Appendix A.3.

Strategy 1 (Teleportation protocol with mixed state): Suppose Alice and Bob share a totally mixed state given by $\rho_{\text{mix}} = 0.5 \cdot I$, where I denotes the identity, instead of a

maximally entangled state. Even if they apply the teleportation protocol, Bob's output state will only be a mixed state $\rho_{\text{out}} = 0.5 \cdot I$, i.e. no information about the input state is transferred. The mean fidelity achievable with this strategy is given by:

$$\mathcal{F}_{\text{lim}}(\text{Strategy 1}) = \frac{1}{2}. \tag{10.4}$$

The same result is achieved if Alice and Bob have no classical communication channel available. In this case all Bob can do is to prepare his qubit in randomly chosen states, resulting in a mean fidelity of $\mathcal{F}_{\text{exp}} = 0.5$.

Strategy 2 (Measure and transfer one bit of information): In this approach Alice and Bob only use the available classical communication channel. Alice measures the unknown input state ψ^{in} along the z-axis, obtains one of the eigenvalues +1 or -1 and projects ψ^{in} into $|0\rangle$ or $|1\rangle$, respectively. She communicates her measurement result to Bob, who prepares his qubit accordingly in $|0\rangle$ or $|1\rangle$, respectively. The mean fidelity $\mathcal{F}_{\text{lim}}$ achievable with this approach depends on the probability distribution of the input states ψ^{in}.

First, consider the case where all possible input states are equally probable. In this case the mean fidelity is given by:

$$\mathcal{F}_{\text{lim}}(\text{Strategy 2.1}) = \frac{2}{3}. \tag{10.5}$$

In an experimental realization generate it is preferable to work with a finite set of input states instead of an ensemble of completely random input states. Such a set of four input states[2] could be for instance:

$$|\psi_1^{\text{in}}\rangle = |1\rangle, \quad |\psi_2^{\text{in}}\rangle = |0\rangle, \quad |\psi_3^{\text{in}}\rangle = \frac{1}{\sqrt{2}}(|0\rangle - i|1\rangle), \quad |\psi_4^{\text{in}}\rangle = \frac{1}{\sqrt{2}}(|0\rangle - |1\rangle). \tag{10.6}$$

In this case Alice's and Bob's strategy result in a mean fidelity of :

$$\mathcal{F}_{\text{lim}}(\text{Strategy 2.2}) = \frac{3}{4}. \tag{10.7}$$

Thus, by choosing a set of input states covering only a quarter of the Bloch sphere, the mean fidelity achievable by Alice and Bob using only a classical channel is increased compared to the case with an equal distribution of input states. However, if two more states are added to the set:

$$|\psi_5^{\text{in}}\rangle = \frac{1}{\sqrt{2}}(|0\rangle + i|1\rangle), \quad |\psi_6^{\text{in}}\rangle = \frac{1}{\sqrt{2}}(|0\rangle + |1\rangle), \tag{10.8}$$

such that all directions on the Bloch sphere are covered, the mean fidelity using stategy 2 becomes:

$$\mathcal{F}_{\text{lim}}(\text{Strategy 2.3}) = \frac{2}{3}. \tag{10.9}$$

Therefore, in order to exclude strategy 2 and prove teleportation in an experiment, the demands in terms of fidelity are less if six instead of only four input states are chosen.
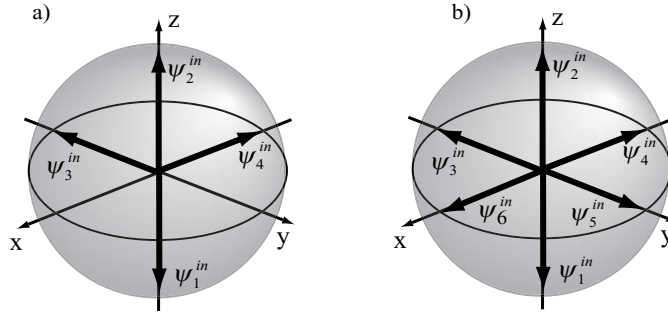
Figure 10.2.: Sets of input states for teleportation. a) Set of four input states given by: $\psi_1^{\text{in}} = |1\rangle$, $\psi_2^{\text{in}} = |0\rangle$, $\psi_3^{\text{in}} = (|0\rangle - i|1\rangle)/\sqrt{2}$ and $\psi_4^{\text{in}} = (|0\rangle - |1\rangle)/\sqrt{2}$. The corresponding Bloch vectors cover only a quarter of the Bloch sphere. b) Set of input states with two additional states $\psi_5^{\text{in}} = (|0\rangle + i|1\rangle)/\sqrt{2}$ and $\psi_6^{\text{in}} = (|0\rangle + |1\rangle)/\sqrt{2}$, giving a set of six input states.

10.4. Adapting Teleportation for the ion trap quantum processor

The crucial ingredients of a teleportation experiment were shown in Fig. 10.1: Generation of an entangled pair of particles, a complete Bell-measurement and reconstruction operations chosen according to the results of the Bell-measurement. In our ion trap experiment we intended to teleport the quantum information stored in one ion qubit to another ion qubit. The quantum circuit accomplishing this task is shown in Fig. 10.3. A three ion crystal was used, where ion 1 carried the input quantum state and ion 2 and 3 served as entangled pair. After completion of the quantum circuit the state of ion 3 was expected to be identical to the input state.

Initially all ions were prepared in their $|S\rangle$ ground state and the center-of-mass mode in its vibrational ground state $|n = 0\rangle$. The quantum circuit started with preparing ions 2 and 3 in a Bell state $(|SD\rangle + |DS\rangle)/\sqrt{2}$ employing the techniques outlined in Ch. 7.

Ion 1 was prepared in the input state by applying the operation U_χ. Next we wanted to subject ions 1 and 2 to a measurement in the Bell basis. The procedure given in Sec. 2.4.2 was used to map the Bell-basis onto the computational basis states, which we can discriminate by a measurement. In Fig. 10.3 the corresponding quantum circuit consisting of a controlled-NOT and a Hadamard operation has been adapted to the ion trap. Hadamard operations were substituted by suitable $\pi/2$-carrier pulses, the controlled-NOT operation was decomposed in $\pi/2$-rotations and a phase gate. The phase gate was implemented as presented in Chapter 8. One of the $\pi/2$-rotations belonging to the CNOT was omitted. Therefore, it was actually the state $R(\pi/2)|\chi\rangle$ that was teleported. The omitted $\pi/2$-pulse was later added to the reconstruction operations applied to ion 3 [3].

---

[2]Choosing at least four non-collinear input states might seem sufficient, since it would allow one to completely characterize the quantum process [71].

[3]Strictly speaking the quantum circuit acting on ion 1 and 2 is not rotating the Bell states completely onto the computational basis. Therefore, Eq. 10.3 would have to be rewritten to take into account our different
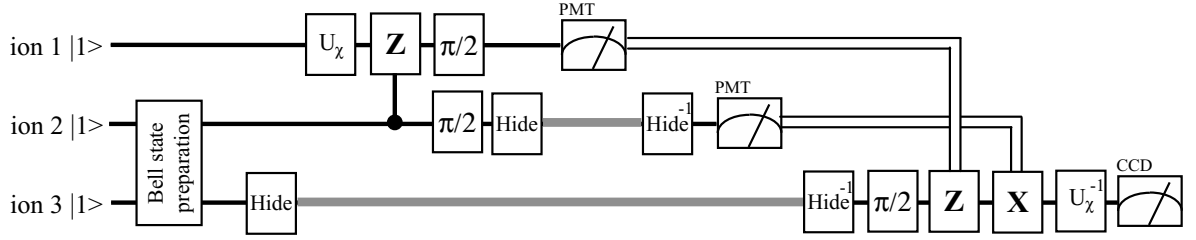
Figure 10.3.: Quantum circuit for teleportation with three ionic qubits. Quantum information is teleported from ion 1 to ion 3. Initially ion 2 and 3 are prepared in a Bell state. Ion 1 is prepared in the input state $|\chi\rangle = U_\chi|S\rangle$. Ion 1 and 2 are subjected to a measurement in the Bell-basis. During the subsequent read-out of both ions the other ions are protected from 397 nm light by mapping their quantum state to the $D' - D$ manifold. The hidden ions are indicated by grey lines in the figure. Resonance fluorescence is detected by the PMT and accordingly π-rotations around the x- and/or z-axis are applied to ion 3 in order to reconstruct the input state.

Ions 1 and 2 were subsequently read out by illuminating each ion with 397 nm laser light for 250 - 300 μs and recording the ion's fluorescence light with the PMT. The signal from the PMT is immediately evaluated by counter electronics, which compared the number of counts during a measurement period with a given threshold in order to decide whether an ion was fluorescing or not (cf. Appendix A.5). After both ions have been read out, information about the computational basis state $\{|00\rangle, |01\rangle, |10\rangle, |11\rangle\}$ into which the two ions were projected is available to the experimental control electronics. Depending on this information, a logical network chose which operations were to be applied to ion 3 in order to reconstruct the input state.

While measuring one of the ions the quantum information stored in the other two ions had to be protected from the 397 nm light. Therefore, the quantum state of these ions was mapped to the $D' - D$ subspace, a technique introduced in Sec. 9.5.2. The quantum state of ion 3 was mapped to the $D' - D$ manifold immediately after the teleportation experiment started. During the subsequent measurements on either ion 1 or 2, the other ion of the pair was mapped into the $D' - D$ subspace. This was even done for ion 1 after it had been measured and was no longer storing critical quantum information. This mapping of a possible population of the S-state to the D'-level guaranteed proper state discrimination, when measuring ion 2.

While quantum information is stored in the $D' - D$-subspace, it is much more affected by magnetic field fluctuations, due to the larger difference in g-factors of the D'- and D-level. In order to cancel a phase shift induced by a drift of the magnetic field, which is constant on the time scale of the experiment, we applied the spin-echo technique. A spin-echo pulse $R_1(\pi, 0)$ was applied to ion 1 and a $R_3(\pi, \pi/2)$ to ion 3 after the phase gate. After ion 1 and ion 2 had been read out a waiting time was introduced to let ion 3 rephase.

After the waiting time, the reconstruction pulses were applied to ion 3. First the $\pi/2$-rotation, which was omitted in the Bell-analysis, was carried out to rotate ion 3 into the

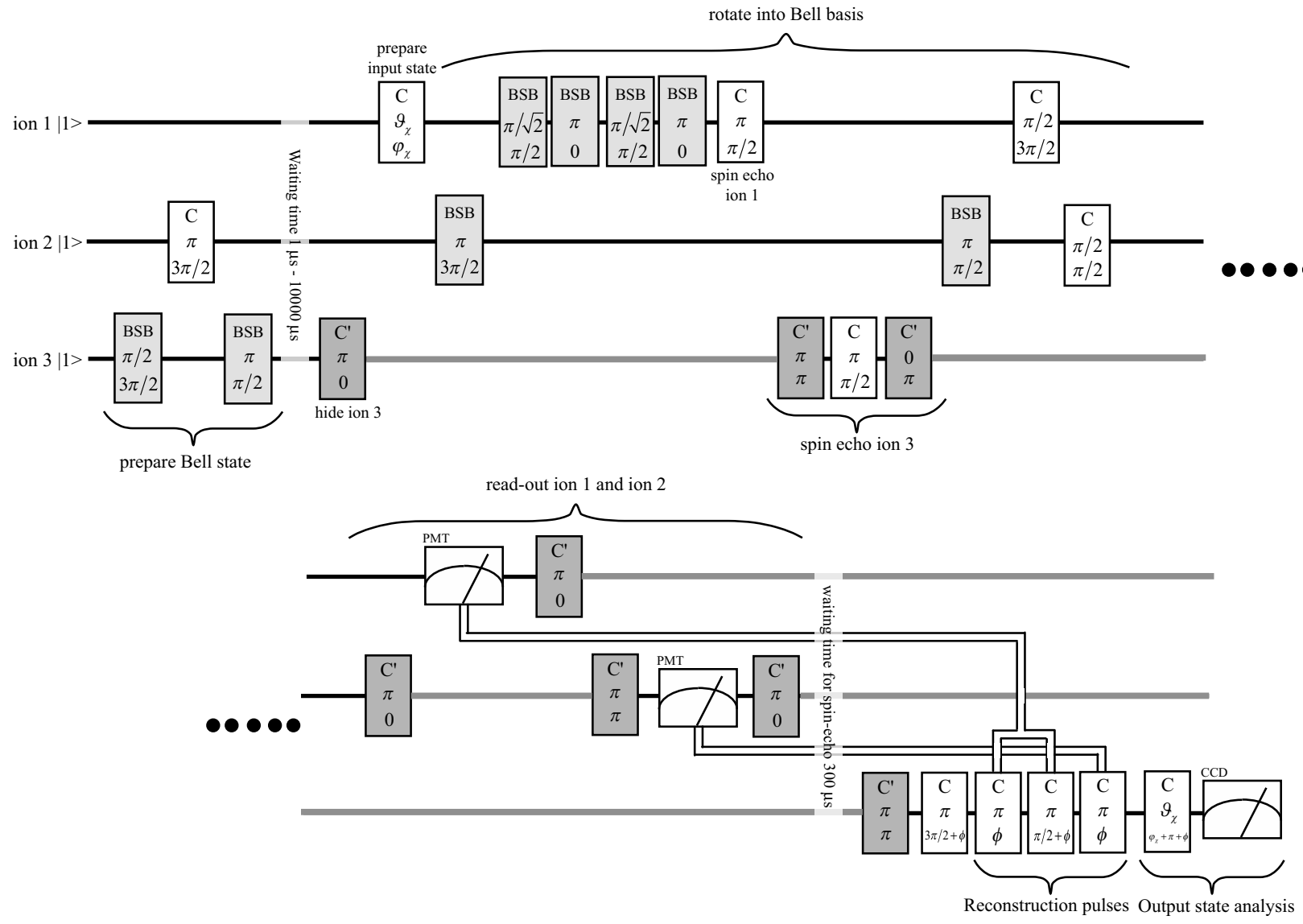measurement setting. Details can be found in Appendix A.4.

Figure 10.4.: Complete pulse sequence of the teleportation algorithm, containing a total of 30 experimental steps.

proper basis. If ion 1 was measured to be in the $|D\rangle = |0_L\rangle$ state, a Z-operation, decomposed in a X- and a Y-operation, was applied while no operation if it was measured to be in $|S\rangle = |1_L\rangle$. If ion 2 was found to be in $|0_L\rangle$ an X-operation was carried out and no operation in the case $|1_L\rangle$ was measured. In this way, for all four possible cases the proper reconstruction operations were applied.

The reconstruction pulses were applied with a variable phase ϕ, which had to be determined experimentally. This additional phase ϕ, which will be denoted as *reconstruction phase* in the following, turned out to be necessary to compensate for a systematic error of the atomic phase prior to the reconstruction pulses. This systematic error was most probably caused by the spin-echo on ion 3, *which added an additional phase shift.* Another possible reason was the imperfect action of the phase gate in the Bell-analysis, due to improper light shift compensation for example, which would have also introduced an additional phase shift of the atomic superpositions.

Finally, the state of ion 3 was analyzed. If the teleportation algorithm was successful, ion 3 was expected to be in input state $|\chi\rangle$, which initially entered the teleportation algorithm. In order to measure the fidelity $F_{\text{tele}} = |\langle\chi|\psi_{\text{out}}\rangle|$ two approaches were pursued:

1. The quantum state of ion 3 after teleportation was estimated by quantum state tomography, which allowed one to calculate the fidelity $F_{\text{tele}} = \langle\psi_i^{\text{in}}|\rho_{\text{out}}^{\text{exp.}}|\psi_i^{\text{in}}\rangle$, where $\rho_{\text{out}}^{\text{exp.}}$ is the density matrix of ion 3 measured after completion of the teleportation algorithm.

2. The operation U_χ^{-1} was applied to ion 3 after teleportation. If ion 3 was in the input state, this operation would have transferred ion 3 back to the $|S\rangle$-state. Therefore the fidelity F_{tele} was directly given by the $|S\rangle$-state population of ion 3, i.e. $F_{\text{tele}} = \langle|\psi_i^{\text{in}}|U_\chi^{-1}\rho_{\text{out}}|\psi_i^{\text{in}}\rangle = P_S$.

In both cases ion 3 was measured by using the CCD-Camera as the detection device.

All laser pulses and detection steps together made up a total of 30 experimental steps necessary in order to implement teleportation. A scheme containing all these steps is shown in Fig. 10.4.

10.5. Experimental results

Teleportation was implemented with a crystal of three ions using the pulse sequence shown in Fig. 10.4. The experimental parameters were adjusted as follows: The Rabi frequencies for the carrier transitions were $\Omega_{-1/2\leftrightarrow-1/2} = 2\pi \cdot 68$ kHz for the $(m = -1/2 \leftrightarrow m' = -1/2)$-transition and $\Omega_{-1/2\leftrightarrow-5/2} = 2\pi \cdot 20$ kHz for the $(m = -1/2 \leftrightarrow m' = -5/2)$-transition used for mapping to the $D - D'$-sublevels. The center-of-mass mode was chosen as the "bus mode" and the Rabi frequency was set to $\Omega_{\text{blue}} = 2\pi \cdot 4$ kHz. The addressing optics was adjusted, such that an addressing error of 3-4% was obtained for all ions.

In order to read out the state of ion 1 and ion 2, each ion was illuminated with laser light at 397 nm for 300 μs. Histograms of the number of fluorescence photons counted with the PMT are shown in Fig. 10.8(a) A threshold of three counts was chosen to discriminate between the events where an ion was or was not fluorescing, which corresponds to the ion being projected into $|1_L\rangle$ or $|0_L\rangle$, respectively. The electronics which evaluated the signal from the PMT during the read-out of ion 1 and ion 2 was set to this threshold.
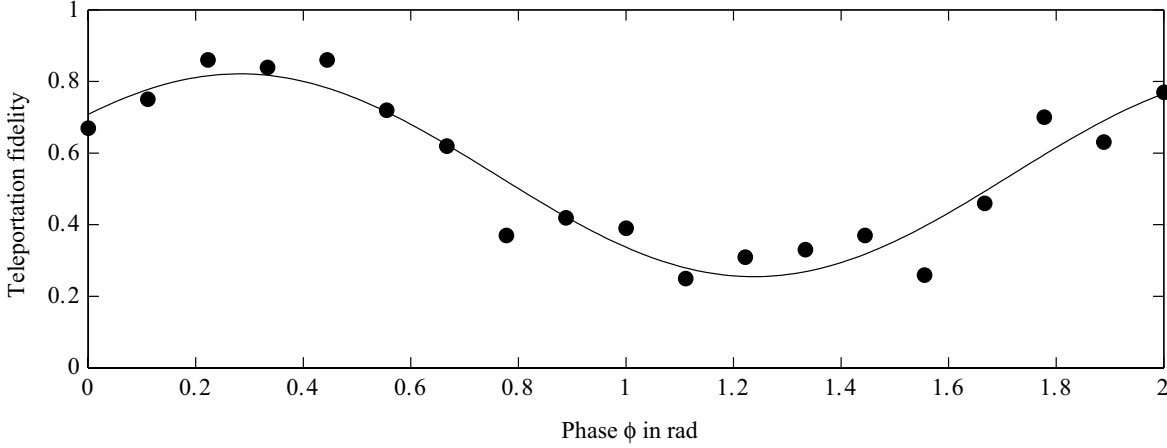
Figure 10.5.: Dependence of the teleportation fidelity F_{tele} on the the reconstruction phase ϕ. The state $|S\rangle = |1_L\rangle$ was used as input state for teleportation. The teleportation fidelity was maximal for $\phi = 0.3\pi$.

In order to cancel a phase shift of the information stored in ion 3 induced by magnetic field fluctuations a spin-echo was implemented. The waiting time prior to the reconstruction operations had to be adjusted in order to properly let the phase of the quantum state phase recover. Various waiting times were tried and finally the waiting time was set to 70μs.

The reconstruction phase ϕ, which compensates for a systematic shift of the phase in the previous experimental steps, was adjusted as follows: The teleportation algorithm was carried out with $|\psi_1^{\text{in}}\rangle = |S\rangle$ as input state. The reconstruction phase ϕ was varied and the teleportation fidelity F_{tele} monitored by applying the operation U_χ^{-1} and measuring the S-state population of ion 3 after completion of the teleportation algorithm. The result of this measurement is shown in Fig. 10.5. A sinusoidal dependence of the teleportation fidelity on the reconstruction phase was observed. Instead of the theoretically expected phase of $\phi = 0\pi$, the teleportation fidelity was found to be maximal for $\phi = 0.3\pi$. This value was used for all teleportation experiments presented here. It is important to point out that the reconstruction phase *did not depend on the input state*, but instead was determined once for one input state and later used for all other input states as well.

The teleportation algorithm was tested with the six input states $|\psi_1^{\text{in}}\rangle - |\psi_6^{\text{in}}\rangle$ discussed in Sec. 10.3. First, the teleportation fidelity F_{tele} was determined by applying the operation U_χ^{-1} to ion 3 and measuring the S-state population P_S. For all six input states P_S was determined by repeating the teleportation experiment 800 times, which yielded:
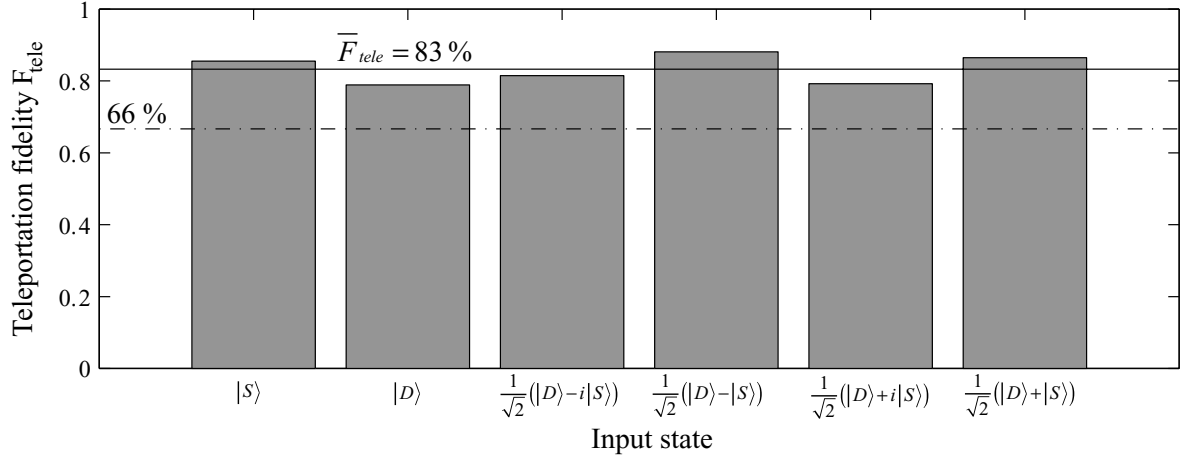
Figure 10.6.: Teleportation fidelity for our six input states. The teleportation fidelity was determined by applying the operation U_χ^{-1} to ion 3 and measuring the S-state population P_S. A mean fidelity of 83(1)% (solid line) was obtained, which is clearly above the limit of 66% (dashed line) for quantum state transfer without teleportation.

i	$|\psi_i^{\mathrm{in}}\rangle$	$F_{\mathrm{tele}} = \langle\psi_i^{\mathrm{in}}|U_\chi^{-1}\rho_{\mathrm{out}}|\psi_i^{\mathrm{in}}\rangle = P_S$
1	$|S\rangle$	86(1)%
2	$|D\rangle$	79(1)%
3	$(|D\rangle - i|S\rangle)/\sqrt{2}$	82(1)%
4	$(|D\rangle - |S\rangle)/\sqrt{2}$	88(1)%
5	$(|D\rangle + i|S\rangle)/\sqrt{2}$	79(1)%
6	$(|D\rangle + |S\rangle)/\sqrt{2}$	87(1)%
Mean Fidelity $\bar{F}_{\mathrm{tele}}$		83(1)%

The errors given are the uncertainty due to quantum projection noise. The fidelities are also shown in Fig. 10.6. The mean fidelity of $\bar{F}_{\mathrm{tele}} = 83(1)$% is well above the threshold of $\mathcal{F}_{\mathrm{lim}}$(Strategy 2.3) = 66 %, such that the obtained results can only be explained by the action of quantum teleportation.

Furthermore, the outcome of the teleportation experiment was analyzed using quantum state tomography of ion 3 after completion of the teleportation algorithm. In Fig. 10.7(a)-(d) real and imaginary part of the obtained density matrices $\rho_{\mathrm{exp},i}$ are shown. The fidelities $\langle\psi_i^{\mathrm{in}}|\rho_{\mathrm{exp},i}|\psi_i^{\mathrm{in}}\rangle$ were calculated to be:

i	$|\psi_i^{\text{in}}\rangle$	$F_{\text{tele}} = \langle\psi_i^{\text{in}}|\rho_{\text{out,i}}^{\text{exp}}|\psi_i^{\text{in}}\rangle$
1	$|S\rangle$	80(2)%
2	$|D\rangle$	76(3)%
3	$(|D\rangle - i|S\rangle)/\sqrt{2}$	77(3)%
4	$(|D\rangle - |S\rangle)/\sqrt{2}$	87(2)%
5	$(|D\rangle + i|S\rangle)/\sqrt{2}$	81(2)%
6	$(|D\rangle + |S\rangle)/\sqrt{2}$	89(2)%
Mean Fidelity $\bar{F}_{\text{tele}}$		82(1)%

Here the errors are again due to quantum projection noise and were obtained by a Monte-Carlo simulation (cf. A.2). The obtained mean fidelity of $\bar{F}_{\text{tele}} = 82(1)\%$ agrees well with the fidelity found with the other approach. The fidelities obtained for each single state all lie in the range of $76 - 89\%$. However, the results don't agree perfectly with the results shown in Fig. 10.6, which is due to systematic errors such as drifts of experimental parameters.

In Sec. 10.2 it has been discussed that neither Alice nor Bob alone have enough information to gain knowledge about the input state. In order to prove this statement the data taken was further analyzed. In Fig. 10.8(b) the relative frequency of four possible outcomes of the Bell-analysis is shown. All four outcomes occurred with almost equal probability of 0.25. In Fig. 10.8(c) the probabilities for the outcomes of the Bell-analysis are examined more closely. The probabilities are shown depending on the different input states. As can be seen, no correlation between the input state and the outcome of the Bell-analysis can be found, which proves that Alice can gain no information about the input state through her Bell-measurement.

In order to prove that Bob alone does not have enough information to recover the input state, the teleportation experiment was carried out, but the reconstruction operations were omitted. The teleportation fidelity for four input states is shown in Fig. 10.8(d). As expected for all four input states the teleportation fidelity without reconstruction operations was only 50%. Thus, as long as Bob has no information about which is the proper reconstruction operation, he only possesses a mixed state.

In Bennett et al.'s original proposal the entangled pair is seen as a resource, which after its preparation, is split up between Alice and Bob and then stored by them until the need for teleportation arises. In order to demonstrate that this is possible with our experimental setup, the Bell state was prepared and a waiting time before the start of the actual teleportation experiment introduced. For waiting times of up to 10 ms no decrease in the teleportation fidelity was observed, which is five times the time necessary for the teleportation experiment. Longer waiting times would have been feasible, if the 729 nm laser had been addressed away from the ions, such that no residual 729 nm light could disturb the entangled state.

In principle, the target ion could have been separated from the other two ions after preparation of the entangled state, since for all further operations on the target ion no common vibrational mode of the target ion and the other ions was necessary. It was not possible to demonstrate this in the current experimental setup. However, separating single ions from crystal could be realized in segmented microtrap designs [106] and was actually demonstrated in teleportation experiment implemented by Barrett et al. [102].
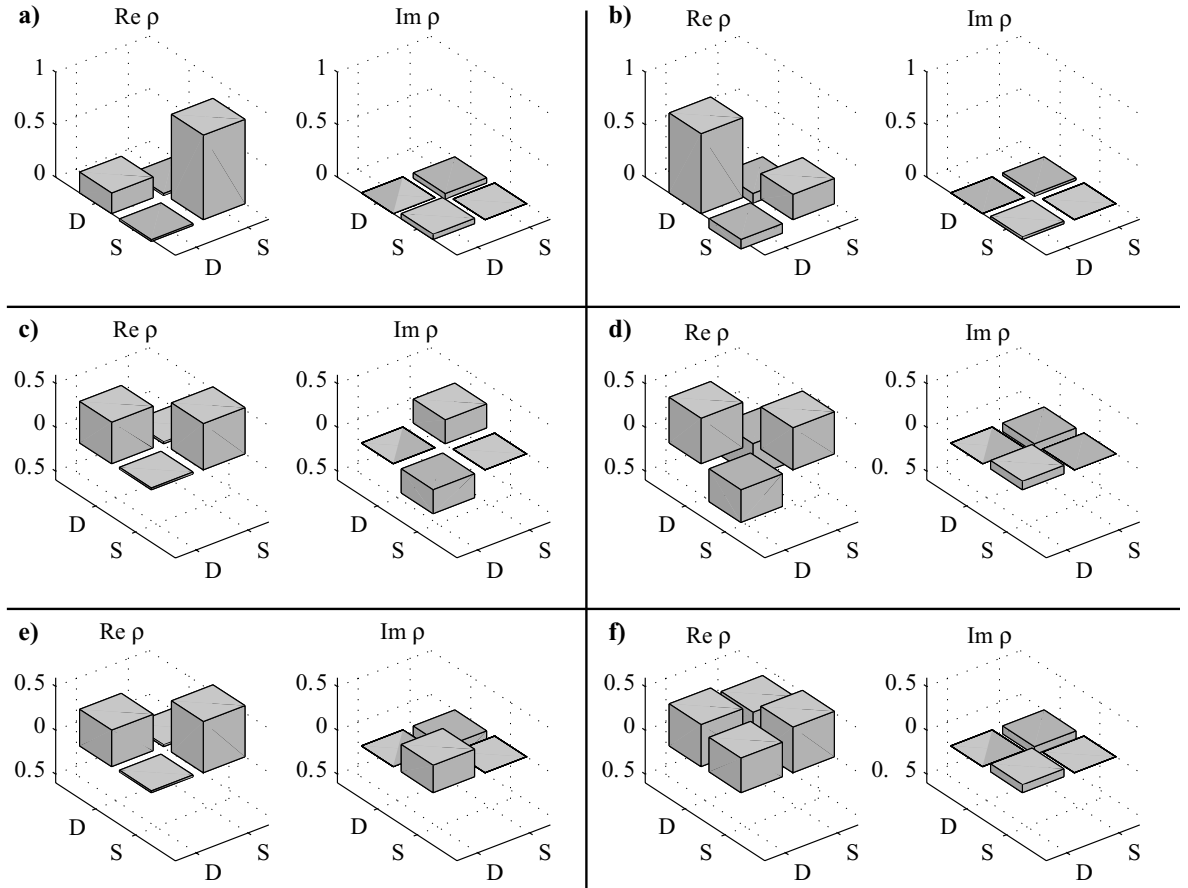
Figure 10.7.: Real and imaginary part of the density matrices of the target ion 3 after completion of the teleportation experiment. The respective input states were a) $|\psi_1^{\text{in}}\rangle = |S\rangle$, b) $|\psi_2^{\text{in}}\rangle = |D\rangle$, c) $|\psi_3^{\text{in}}\rangle = (|D\rangle - i|S\rangle)/\sqrt{2}$, d) $|\psi_4^{\text{in}}\rangle = (|D\rangle - |S\rangle)/\sqrt{2}$, e) $|\p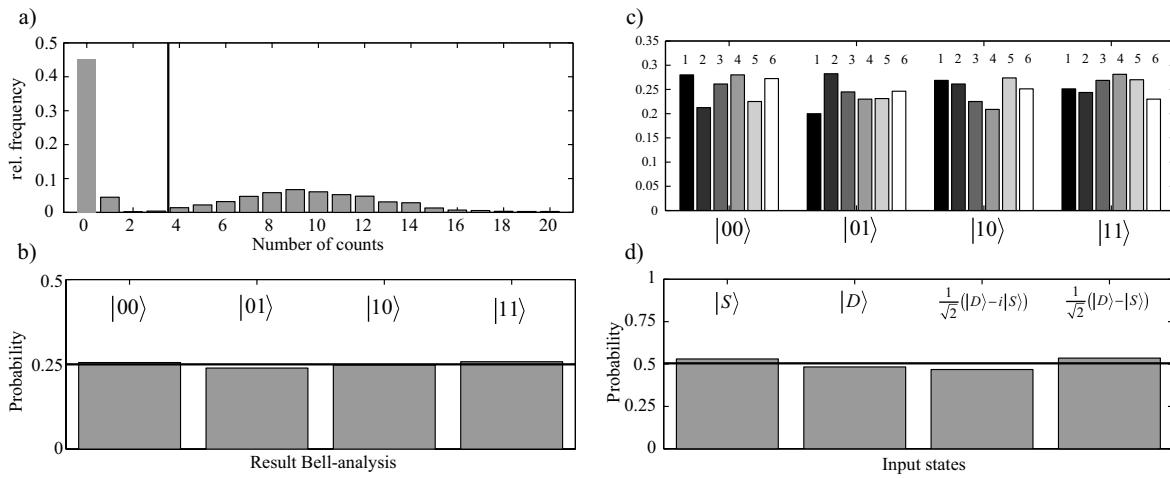si_5^{\text{in}}\rangle = (|D\rangle + i|S\rangle)/\sqrt{2}$ and f) $|\psi_6^{\text{in}}\rangle = (|D\rangle + |S\rangle)/\sqrt{2}$.

Figure 10.8.: Statistics of the Bell-analysis. a) Histogram of the number of photons counted by the PMT during a measurement time of $300\mu s$. b) Probabilities of the four outcomes of the Bell-analysis in a data set of 4800 teleportation experiments. In c) the same statistics is split up for all six input states ($i = 1 - 6$ cf. Fig. 10.6). d) Teleportation fidelity for four input states if no reconstruction operations are applied.

10. Quantum Teleportation

11. Summary and Outlook

In this thesis the ability to prepare and manipulate entangled states of atomic qubits in an ion trap quantum processor were investigated. It was clearly demonstrated that entangled states of two and three ions can be prepared with the available experimental setup. It was found that some of the prepared entangled states are remarkably stable against decoherence, displaying coherence times which exceed those of a single qubit by orders of magnitude.

With two ion qubits all four Bell states were generated with fidelities on the order of 90%. The lifetime of these entangled states was investigated and it was found that the Bell states Ψ_+ and Ψ_- are particular stable, their lifetime being limited only by the lifetime of the $D_{5/2}$ level. These states are intrinsically stable against the main source of decoherence in our experiment, namely phase fluctuations of the atomic superpositions which affect all qubits in the same way. These correlated phase fluctuations are caused by fluctuations of the laser light manipulating the qubits and fluctuations of the magnetic field, changing the atomic resonance frequency via the Zeeman effect.

Furthermore, a detailed analysis of the implementation of the Cirac-Zoller CNOT quantum gate was carried out. This quantum gate is an important cornerstone for implementing an ion trap quantum computer and allowed us to generate GHZ-states and the complete Bell-measurement within the teleportation experiment. The CNOT gate pulse sequence was investigated for all possible input states and it was found that with 70-80% probability the correct output state is obtained. An analysis of the various error sources using simulations of the CNOT gate showed that the frequency noise of the laser light at 729 nm is the main error source.

With three ion qubits both types of tripartite entangled states, GHZ- and W-states, were generated. For GHZ-states a fidelity of 76% was achieved while W-states could be prepared with a fidelity of even 83%. The respective lifetime of both types of entangled states were investigated. W-states were expected to be intrinsically stable against correlated phase fluctuations, while GHZ-states should be particularly sensitive to this kind of fluctuation. Exactly this behavior was observed experimentally. Furthermore, the effect of a measurement of a single qubit on these entangled states was studied. This required to prevent the other qubits from being projected by the applied 397 nm light, which was accomplished by mapping the population of the S-state, which couples to the 397 nm light, to an additional Zeeman sublevel of the $D_{5/2}$-state. It was observed that GHZ- and W-states are affected differently by such a measurement in the computational basis . For GHZ-states it was observed that a measurement destroys all entanglement and leaves the qubit register in a mixed state. In contrast, it was found that W-states retain bipartite entanglement after the measurement. The experimental setup was improved, such that the result of a measurement of one or two qubits could be immediately evaluated to choose subsequent operations on the qubit register. This technique was first demonstrated with a measurement of single qubit in a GHZ-state in a rotated basis. The subsequently applied operations, which were chosen according to the

outcome of the measurement, allowed us to transfer the created mixed state of two different Bell states into a pure Bell state of the two unmeasured qubits.

Finally, the demonstrated experimental techniques with two and three ions allowed the complete implementation of the teleportation scheme proposed by Bennett et al. [12]. The pair of entangled particles necessary for this scheme was generated on demand and kept as resource for a variable waiting time of up to ten times the time necessary for the actual teleportation experiment. Furthermore, our ability to perform a CNOT-operation allowed us to implement a complete Bell measurement. Our capability to perform single qubit operations conditioned by the outcome of a previous measurement was employed to choose the suitable operations necessary to reconstruct the original quantum state in the target qubit. This is the first time that this final step in the teleportation scheme has been experimentally demonstrated. The pulse sequence was tested with six different input states covering the whole Bloch sphere, resulting in a mean fidelity of 83%. This teleportation experiment demonstrated almost all techniques available in our experiment. In addition, it is the most complex experiment carried out so far with our experimental setup including over 30 individual experimental steps. It therefore serves as a kind of benchmark algorithm for our ion trap quantum processor.

The experimental techniques demonstrated in this thesis will be applied in even more complex experiments in the future. A straightforward expansion of the teleportation scheme is *entanglement swapping*, which is teleportation of entanglement in which two previously unentangled qubits become entangled without direct interaction [107, 108]. Another interesting line of experiments would be to investigate entangled states of four and five ions. The generic principle of the pulse sequence shown in Ch. 9 for preparing W-states can be expanded to generate W-states of an arbitrary number of ions. Simulations show that with the current experimental setup W-states of four or five ions can be prepared with a fidelity on the order of $\approx 88\%$ [109].

The results presented in this thesis concerning Bell-states showed that the Bell states Ψ_+ and Ψ_- act as a decoherence free subspace (DFS). It is worth investigating if it is advantageous to encode quantum information in this DFS, i.e. in superpositions of the kind $(a|\Psi_+\rangle + b\Psi_-\rangle)/\sqrt{2}$, even though the number of necessary qubits is doubled by this measure. The success of this strategy will depend greatly on the of difficulty of realizing single qubit operations and quantum gates in the DFS.

The complexity of experiments that can be implemented with the current experimental setup is mainly limited by the number of CNOT gate operations, which can be carried out within the coherence time of the qubits. Since CNOT gate operations take approximately 500μs and the time for an experiment is limited to approximately 1 ms by the single qubit coherence time, only 1-2 gate operations are feasible. This limits the number of interesting experiments that can be implemented with the current setup. This situation could be improved by the following means:

- The coherence time could be increased by improving the frequency stability of the 729 nm laser system and the stability of the ambient magnetic field. Improvements on the former are currently underway. A better construction of the reference cavity and improvements on the electronics of the locking scheme are planned. The stability of the ambient magnetic will hopefully be improved by installing a new magnetic field stabilization system, which promises to suppress magnetic field fluctuations in a larger

frequency range than the currently installed system.

- Proposals for two qubit quantum gates different from the Cirac-Zoller proposal which promise shorter gate times could be tested.

Concerning the latter point, the quantum gate implemented by Leibfried et al. is most noteable [110]. They implemented a phase gate with a fidelity of 97% and a gate time of $\approx 40\mu$s. However, this gate requires the encoding of the quantum information either in a hyperfine or Zeeman splitting of the $S_{1/2}$ ground state. A hyperfine structure is not available in ^{40}Ca$^+$. A new experiment is currently being built, which will use ^{43}Ca$^+$, which has the necessary hyperfine structure.

These improvements of the experimental setup would allow one to implement various interesting experiments. Realizing quantum error correction with our experimental setup would, for example, be an important step towards implementing a scalable ion trap quantum computer. Furthermore, it might become feasible to demonstrate a simplified version of Shor's algorithm similar to the experiment realized by Vandersypen et al. [46].

11. Summary and Outlook

A. Appendix

A.1. Quantum State Tomography

A.1.1. Choice of operators O_i and measurement of expectation values $\langle O_i \rangle$

In Sec. 2.6 it was stated that the density matrix ρ of a n-qubit system can be expanded into a series of mutually orthogonal operators O_i (cf. Eq. 2.21). A convenient choice for a set of operators O_i are the outer products of the Pauli-matrices given by:

$$O_i = \sigma_{i_1} \otimes \sigma_{i_2} \otimes ... \otimes \sigma_{i_n}, \quad i_k \epsilon [1, 4] \tag{A.1}$$

where

$$\sigma_1 = I, \quad \sigma_2 = X, \quad \sigma_3 = Y, \quad \sigma_4 = Z. \tag{A.2}$$

In our experimental setup we obtain the population probabilities p_k of the 2^n computational basis states, i.e. the diagonal elements of the density matrix. Thus, we can directly extract the expectation values $\lambda_i = tr(\rho \cdot O_i)$ from the measured population probabilities for all O_i containing only the Pauli-matrices I and Z. For measurements of the expectation values of operators containing the Pauli-matrices X and Y, the measurement basis has to be changed. For a single qubit this basis transformation works as follows. Since we preferably measure the expectation value of $tr(Z\rho)$, we apply rotations prior to the measurement such that:

$$tr(Z(U_x \rho U_x^\dagger)) = tr((U_x^\dagger Z U_x)\rho) = tr(X\rho), \tag{A.3}$$

$$tr(Z(U_y \rho U_y^\dagger)) = tr((U_y^\dagger Z U_y)\rho) = tr(Y\rho), \tag{A.4}$$

where $U_x = R_{\bar{y}}(\pi)$ and $U_y = R_x(\pi)$ (see Sec. 4.5.1). For a system of n-qubits these rotations have to be applied to the ions, where an operator X or Y is to be measured.

Even though the expectation values of 4^n operators have to be determined actually less measurements are necessary, since a measurement of $\langle Z^{\otimes n} \rangle$ allows us to calculate all expectation values containing all combinations of I and Z. The same is true for $\langle X^{\otimes n} \rangle$ and $\langle Y^{\otimes n} \rangle$ and operators containing only combinations of I and X or I and Y, respectively. Therefore, for two qubits we only have to measure nine expectation values instead of 16 and for three qubits 27 instead of 64 measurements are necessary.

A.1.2. Maximum likelihood estimation

As has been shown in the previous section the density matrix of a quantum system can be directly calculated using Eq. 2.21 from the measured expectation values λ_i. However, it turns out that the density matrices obtained by this direct reconstruction method are often not physical valid. This is caused by inevitable errors in the measurements of the expectation values. A density matrix for a physical state has to be normalized, i.e $tr(\rho) = 1$,

A. Appendix

Hermitian, i.e $\rho^\dagger = \rho$, and positive semidefinite, i.e $\langle\psi|\rho|\psi\rangle \geq 0, \forall|\psi\rangle$. These properties imply that all eigenvalues of ρ are real and must lie in the interval $[0,1]$, which in turn implies $0 \leq tr(\rho^2) \leq 1$ [111].

In order to obtain physical valid density matrices a maximum likelihood estimation of the density matrix can be employed as outlined by James et al. [111]. The procedure for maximum likelihood estimation of the density matrix is as follows:

1. A $2^N \times 2^N$ matrix is constructed, which is normalized, hermitian and positive semidefinite. This matrix will be a function of 4^N real parameters $\mathbf{t} = \{t_1, t_2, ..., t_{4^N}\}$.

2. A likelihood function $\mathcal{L}(\mathbf{t}, \lambda)$ is defined which quantifies how good the density matrix $\rho(\mathbf{t})$ fits the experimental data given by $\lambda = \{\lambda_1, \lambda_2, ..., \lambda_{4^N}\}$.

3. The optimum set $\mathbf{t}^{(\mathrm{opt})}$ maximizing $\mathcal{L}(\mathbf{t}, \lambda)$ is found by numerical optimization, which provides $\rho(\mathbf{t}^{(\mathrm{opt})})$ as the best estimate for the density matrix.

An explicit recipe how to parameterize the density matrix of a two qubit system, such that it is physical valid, can be found in [111]. Construction of a parameterized density matrix for higher dimensional systems can be done analogously. As likelihood function we employed:

$$\mathcal{L}(\mathbf{t}, \lambda) = \prod_i^{4^N} \exp\left[\frac{-(\lambda_i - tr(\rho(\mathbf{t})O_i))^2}{1 - tr(\rho(\mathbf{t})O_i)^2}\right]. \tag{A.5}$$

Instead of finding the maximum of this function, we rather search for the minimum of its logarithm. The density matrix obtained by direct reconstruction is used to calculate the initial guess parameters $\mathbf{t}^{(\mathrm{guess})}$.

A.2. Estimating errors using Monte Carlo simulations

Quantum state tomography is an essential tool in our experiments. The density matrices obtained with this technique are used to derive quantities like the fidelity, various entanglement measures or simply values of certain matrix elements which are used to assess the performance our experiments. These quantities have a certain statistical error, since the estimation of the density matrix itself depends on the results of measurements which are affected by quantum projection noise [86]. Estimating the errors of the derived qualities using the standard methods for calculating the propagation of errors are difficult to apply. Instead, we can employ our knowledge about the source of errors and the resulting probability distribution to estimate the error using Monte Carlo simulations of our experiment [112].

The procedure to estimate the error σ_Q of a quantity $Q(\rho)$ calculated from a measured density matrix is as follows:

Step 1 Calculate the results of the measurements of $\lambda_i = \langle O_i \rangle$ using the density matrix obtained by quantum state tomography.

Step 2 Use these parameters and the probability distribution modelling our errors to simulate data sets $\{\lambda_i\}_k^S$.
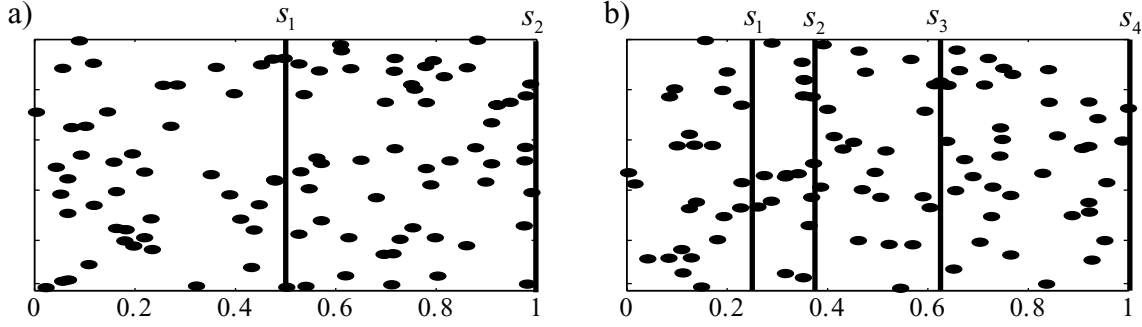
Figure A.1.: a) Set of $N = 100$ random numbers R_i. The probability $p(1) = 0.5$ is indicated by the vertical line. For different sets of random numbers R_i the probability $p^S(1) = $ (Number of $R_i > p(1))/N$ is binomially distributed around $p(1)$ b) Another set of $N = 100$ random numbers. The values of the probabilities $s_k = \sum_{m=1}^{k} p_m$ are indicated. For different sets of numbers R_i the probabilities $s_k^S = $ (Number of $R_i > \sum_{m=1}^{k} p_m)/N$ are obtained from which binomially distributed sets of probabilities $\{p_1^S, p_2^S, p_3^S, p_4^S\}$ which obey the relation $\sum_{i=1-4} p_i^S = 1$.

Step 3 Reconstruct density matrices ρ_k^S from these data sets. Calculate desired quantity $Q_k^S = Q(\rho_k^S)$ for all ρ_k^S and finally determine the standard error $\sigma_Q^S = \left[\sum_k (\bar{Q}^S - Q_k^S)^2\right]^{1/2}$, which serves as an estimator of the error σ_Q.

Implementing Step 2 requires simulating the outcome of experiments for given expectation values λ_i taking quantum projection noise into account. For a single qubit the outcome of a single measurement can either be 0 or 1 and the statistics of N measurements is governed by a binomial probability distribution depending on the probabilities $p(0)$ and $p(1)$ [113].

In order to simulate the outcome of N measurements, a series of N equally distributed random numbers R_i in the interval $[0, 1]$ is generated and the probability $p^S(1) = $ (Number of $R_i > p(1))/N$ calculated, as illustrated in Fig. A.1. By repeating this procedure we obtain a set of simulated data points with value $p^S(1)$ and $p^S(2) = 1 - p^S(1)$, which are binomially distributed around $p(1)$ and $p(2)$, respectively.

For systems of n qubits we have 2^n output states with probabilities $\{p_1, .., p_{2^n}\}$. Even though we have more than two output states, the governing probability distribution is still binomial, since we are always able to separate the quantum states in two groups by investigating the probability to obtain a particular output state and not one of the others. Simulation of data points is done analogous to the single qubit case. A set of N random numbers is generated and the probabilities

$$s_k^S = \frac{\text{Number of } R_i > \sum_{m=1}^{k} p_m}{N} \qquad (A.6)$$

are calculated. The case of two qubits illustrated in Fig. A.1b). From the obtained s_k the probabilities $p^S(i)$ can be successively calculated by $p_1^S = s_1$, $p_1^S = s_1 - p_2^S$ and so forth. The construction of the s_k guarantees that the p_i^S will obey the condition $\sum_i p_i^S = 1$.

A.3. Maximum achievable fidelity for quantum state transfer without teleportation

Teleportation is allowing two parties -Alice and Bob- to perfectly transfer a quantum state using an entangled pair of particles and by communicating two classical bits of information. In Sec. 10.3 a few strategies of Alice and Bob to transfer an unknown quantum state without use of entanglement were discussed.

A.3.1. Measurement and transfer of 1 classical bit of information

Alice is measuring the unknown quantum state in her possession in the z-direction and is obtaining the eigenvalues ± 1 as result. She communicates this one bit of classical information to Bob, who will choose to prepare his qubit in $|0\rangle$ or $|1\rangle$, accordingly. The mean fidelity achievable with this strategy, depends on the distribution of input states. It has to be emphasized that neither Alice nor Bob have any knowledge about the distribution of the input quantum states. Therefore they are not able to adapt their strategy accordingly in order to achieve a higher mean fidelity.

Case 1 (Equal probability distribution): The input state $|\psi^{\text{in}}\rangle$ can be expressed as:

$$\psi^{\text{in}}(\theta, \varphi) = \cos\frac{\theta}{2}|0\rangle + e^{-i\varphi}\sin\frac{\theta}{2}|1\rangle. \tag{A.7}$$

By measuring in z-direction, Alice projects the input state either in $|0\rangle$ or $|1\rangle$, corresponding to the eigenvalues $z = +1$ and $z = -1$, respectively, where the corresponding probabilities are:

$$P(z = +1, \theta, \varphi) = \cos^2\frac{\theta}{2},$$
$$P(z = -1, \theta, \varphi) = \sin^2\frac{\theta}{2}. \tag{A.8}$$

If Bob prepare his qubit accordingly in $|0\rangle$ or $|1\rangle$ the fidelity is given by:

$$F(z = +1, \theta, \varphi) = \cos^2\frac{\theta}{2},$$
$$F(z = -1, \theta, \varphi) = \cos^2\frac{\theta}{2}. \tag{A.9}$$

The mean fidelity over an ensemble of input states, where all states on the Bloch sphere are equal probable, is given by:

$$\mathcal{F} = \frac{1}{4\pi}\sum_{z=\pm 1}\int_0^{2\pi}d\varphi\int_0^\pi d\theta\sin\theta\cdot P(z,\theta,\varphi)\cdot F(z,\theta,\varphi) \tag{A.10}$$

$$= \frac{1}{2}\int_0^\pi d\theta\sin\theta\cdot\left(\cos^4\frac{\theta}{2} + \sin^4\frac{\theta}{2}\right) \tag{A.11}$$

Which results in:

$$\mathcal{F} = \frac{2}{3} \tag{A.12}$$

Case 2 (Finite set of input states): We assume that the unknown quantum states given to Alice comprise only a set of N input states $\psi_i^{\text{in}} = \psi^{\text{in}}(\theta_i, \varphi_i)$. The mean fidelity Alice and Bob can achieve by measuring the unknown quantum state and preparing Bob's qubit in $|0\rangle$ or $|1\rangle$ is:

$$\mathcal{F} = \frac{1}{N} \sum_{z=-1,+1} \sum_{i=1}^{N} P(z, \theta_i, \varphi_i) \cdot F(z, \theta_i, \varphi_i), \tag{A.13}$$

where $P(z, \theta_i, \varphi_i)$ and $F(z, \theta_i, \varphi_i)$ are given in Eq. A.8 and A.9, respectively.

First consider the case of a set of four input states given by:

$$\psi_1^{\text{in}}(\theta_1 = \pi, \varphi_1 = 0) = |1\rangle,$$
$$\psi_2^{\text{in}}(\theta_2 = 0, \varphi_2 = 0) = |0\rangle,$$
$$\psi_3^{\text{in}}(\theta_3 = \frac{\pi}{2}, \varphi_3 = -\frac{\pi}{2}) = \frac{1}{\sqrt{2}}\left(|0\rangle - i|1\rangle\right),$$
$$\psi_4^{\text{in}}(\theta_4 = \frac{\pi}{2}, \varphi_4 = -\pi) = \frac{1}{\sqrt{2}}\left(|0\rangle - |1\rangle\right). \tag{A.14}$$

These states correspond to the vectors on the Bloch sphere along the $\pm z$, y and $-x$-axis, i.e. these vectors span up a quarter of the Bloch sphere. Inserting these states into Eq. A.13 gives the mean fidelity :

$$\mathcal{F}(\text{N=4 input states}) = \frac{3}{4} \tag{A.15}$$

The mean fidelity can be decreased by adding another two states, which correspond to Bloch vectors along the x and $-y$-axis, namely the states:

$$\psi_5^{\text{in}}(\theta_5 = \frac{\pi}{2}, \varphi_5 = \frac{\pi}{2}) = \frac{1}{\sqrt{2}}\left(|0\rangle + i|1\rangle\right),$$
$$\psi_6^{\text{in}}(\theta_6 = \frac{\pi}{2}, \varphi_6 = 0) = \frac{1}{\sqrt{2}}\left(|0\rangle + |1\rangle\right). \tag{A.16}$$

By inserting all six states in Eq. A.14 and A.16 into Eq. A.13 results in a mean fidelity of:

$$\mathcal{F}(\text{N=6 input states}) = \frac{2}{3}. \tag{A.17}$$

A.4. Bell-analysis and Reconstruction

A.4.1. Bell-analysis

Fig. A.2a) shows the operations implementing the Bell-analysis in our teleportation experiment. In order to map the Bell states onto the computational basis one $\pi/2$-rotation is missing. This operation was omitted and instead, we chose to add this operation to the reconstruction operations. Technically, due to the missing $\pi/2$-rotation, we measure in a rotated Bell basis. From the known unitary operation of a phase gate and the applied carrier pulses (cf. Sec. 4.5) the operation of the circuit shown in Fig. A.2(a) including the spin-echo pulse
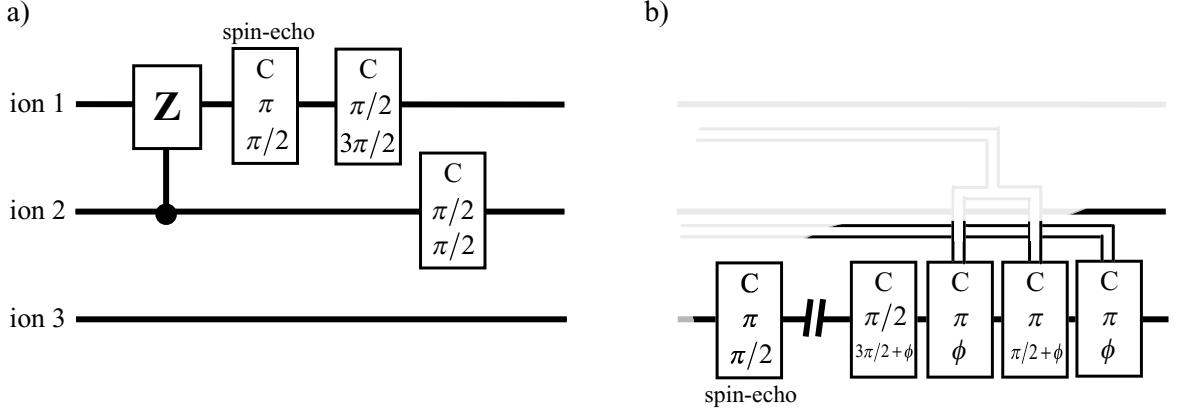
a)

b)

Figure A.2.: a) The circuit implementing the Bell measurement in our teleportation experiment. b) Part of the pulse sequence shown in Fig. 10.4 implementing the reconstruction of the input state in ion 3.

can be inferred to be:

$$U_{\text{analysis}} = \frac{1}{2} \begin{pmatrix} 1 & 1 & 1 & -1 \\ 1 & -1 & 1 & 1 \\ 1 & 1 & -1 & 1 \\ 1 & -1 & -1 & -1 \end{pmatrix}. \tag{A.18}$$

The actual basis in which the measurement is carried out can be inferred, by considering onto which states the computational basis states are mapped by the inverse operation U_{analysis}^{-1}. We obtain:

$$|\zeta_1\rangle = \frac{1}{\sqrt{2}} \left(\Phi_- + \Psi_+ \right) \quad |\zeta_2\rangle = \frac{1}{\sqrt{2}} \left(\Phi_+ + \Psi_- \right) \tag{A.19}$$

$$|\zeta_3\rangle = \frac{1}{\sqrt{2}} \left(\Phi_+ - \Psi_- \right) \quad |\zeta_4\rangle = \frac{1}{\sqrt{2}} \left(\Phi_- - \Psi_+ \right). \tag{A.20}$$

Here, the states $\{|\zeta_1\rangle, |\zeta_2\rangle, |\zeta_3\rangle, |\zeta_4\rangle\}$ are mapped onto $\{|00_L\rangle, |01_L\rangle, |10_L\rangle, |11_L\rangle\}$. The necessary reconstruction operation on the target qubit are obtained, if Eq. 10.3 is rewritten in terms of the basis states $|\zeta_i\rangle$:

$$\frac{1}{\sqrt{8}}[X|\psi_{\text{in}}\rangle_B \otimes |\Phi_+\rangle_A + XZ|\psi_{\text{in}}\rangle_B \otimes |\Phi_-\rangle_A |\psi_{\text{in}}\rangle_B \otimes |\Psi_+\rangle_A + Z|\psi_{\text{in}}\rangle_B \otimes |\Psi\rangle_A]$$

$$= \frac{1}{2}[(XZ + I)|\psi_{\text{in}}\rangle_B \otimes |\zeta_1\rangle_A + (X + Z)|\psi_{\text{in}}\rangle_B \otimes |\zeta_2\rangle_A + (X - Z)|\psi_{\text{in}}\rangle_B \otimes |\zeta_3\rangle_A$$

$$+ (XZ - I)|\psi_{\text{in}}\rangle_B \otimes |\zeta_4\rangle_A] \tag{A.21}$$

A.4.2. Reconstruction operations

In Fig. A.2(b) the operations reconstructing the input state in ion 3 are shown. The pulse implementing a spin-echo on ion 3, the $\pi/2$-pulse omitted in the Bell-analysis and the pulses,

which are applied conditioned on the result of the measurements, are included. The latter four pulses are applied with a variable phase ϕ. The value of ϕ was determined experimentally.

The spin-echo pulse $S = R_3(\pi, \pi/2)$ and the following $R_{\text{basis}} = R_3(\pi/2, 3\pi/2)$ pulse correspond to the unitary operations:

$$S = \begin{pmatrix} 0 & -1 \\ 1 & 0 \end{pmatrix} \quad R_{\text{basis}} = \frac{1}{\sqrt{2}} \begin{pmatrix} 1 & -1 \\ 1 & 1 \end{pmatrix}. \tag{A.22}$$

If these operators are applied to the state of the third ion in Eq. A.21 we obtain:

$$\frac{1}{\sqrt{2}} R_{\text{basis}} \cdot S \cdot (XZ + I)|\psi_{\text{in}}\rangle_B = XZ|\psi_{\text{in}}\rangle_B$$

$$\frac{1}{\sqrt{2}} R_{\text{basis}} \cdot S \cdot (X + Z)|\psi_{\text{in}}\rangle_B = X|\psi_{\text{in}}\rangle_B$$

$$\frac{1}{\sqrt{2}} R_{\text{basis}} \cdot S \cdot (X - Z)|\psi_{\text{in}}\rangle_B = -Z|\psi_{\text{in}}\rangle_B$$

$$\frac{1}{\sqrt{2}} R_{\text{basis}} \cdot S \cdot (XZ - I)|\psi_{\text{in}}\rangle_B = -|\psi_{\text{in}}\rangle_B \tag{A.23}$$

By comparing these results with Eq. **??** we see that the operation $(R_{\text{basis}} \cdot S)$ rotates ion 3, such that can we can apply the conditional reconstruction operations as if we actually measured in the Bell basis. The conditional operations we apply are (cf. A.2):

$$R(\pi, 3\pi/2) \cdot R(\pi, \pi) = -iZ \tag{A.24}$$

$$R(\pi, \pi) = -iX \tag{A.25}$$

The Z-operation is applied whenever ion 1 is found to be in the $|D\rangle = |0_L\rangle$ state and the X-operation whenever ion 2 is found to be in the $|D\rangle = |0_L\rangle$ state. All four conditional operations are:

Measurement result	corresponding basis state	Conditional operation
$|00\rangle$	$|\zeta_1\rangle$	-XZ
$|01\rangle$	$|\zeta_2\rangle$	-iX
$|10\rangle$	$|\zeta_3\rangle$	-iZ
$|11\rangle$	$|\zeta_4\rangle$	I

A.5. Counter electronics for PMT read-out and conditional choice of pulses

The electronic circuit shown in Fig. A.4 allows us to count the TTL-pulses coming from our photo-multiplier, to decide whether the number of counts exceed a preset threshold and to store the result in a Flip-Flop. Depending on the results of these measurements TTL-pulses, which switch on or off a RF-signal going to our 729 nm AOM, are masked by the electronics. This way, the conditional operations in Sec. 9.5.3 and Ch. 10 were implemented. In the following the input and output signal denoted by names in capital letters can be found in the scheme in Fig. A.4.
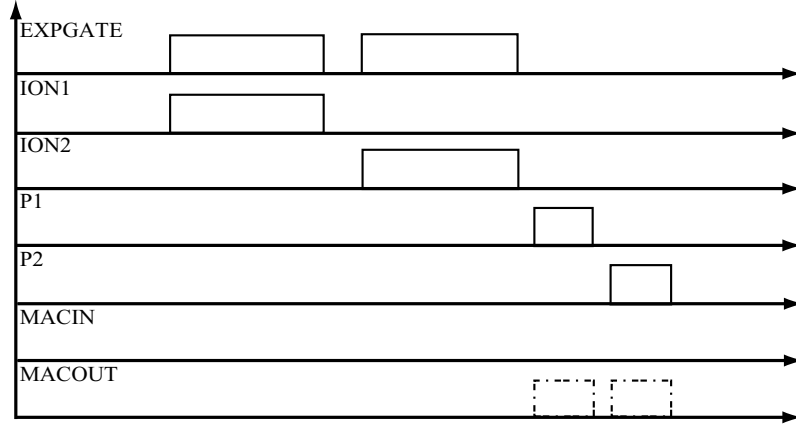
Figure A.3.: Typical sequence of TTL-pulses which control the counter electronics. The EXP-GATE signal defines the intervals during which pulses from the PMT are counted. ION1 and ION2 determine in which of the flip-flops the result of a measurement is stored. P1 and P2 are pulses which depending on the results stored in the flip-flop are to the signal MACIN.

Our photo-multiplier device generates TTL-pulses with a length of 5-8 ns. These pulses are too short to be counted by standard TLL-logic components. Therefore, the initial stage of our counter electronics stretches the pulses from the PMT to a length of $\approx 50ns$. For this purpose a MAX903 comparator is used in a self-latched scheme, where the length of the pulses a the output are determined by the value of the capacitor C_{Latch}.

During the periods in which the input EXPGATE is HIGH, a 74xx191 4-bit-counter counts the TTL-pulses. It is counting down from an initial value, set by switches on the front panel, which control the value of the inputs A-D of the counter. In our experiments this value was usually set to the threshold, which discriminates between the events where ions fluoresce or not. If more events are counted during the measurement period as is set by the threshold its output MAX/MIN switches to HIGH. After the measurement period the state of the output MAX/MIN is stored in a flip-flop. The 74xx109 is containing two flip-flops and can therefore store the results of two measurement periods. In which of the two flip flops the result is stored is chosen by setting either the input ION1 or ION2 to HIGH. Additionally measurement results can be inverted by switches on the back panel, which control the inputs INV1 and INV2.

The following stage of logical gates is either adding the pulses P1 and P2 to the signal MACIN, depending on the result stored in the flip-flops. For instance pulse P1 is added, if flip-flop 1 is storing the result HIGH, i.e. if the counter counted more events than set by the threshold in the corresponding measurement period. If the inverter is activated (INV1=HIGH), the pulse is not added.

The output signal MACOUT is carrying the original pulses from MACIN and the pulses added by our electronics.
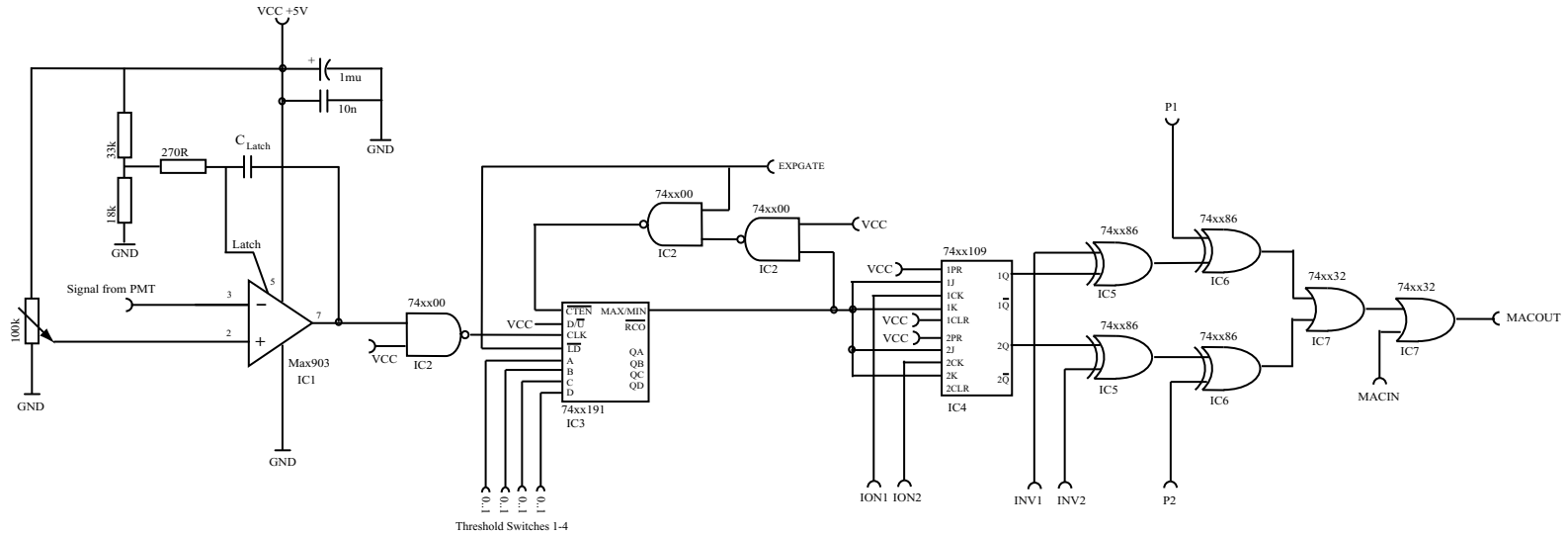
Figure A.4.: Circuit diagram of the electronics counting the signals from the PMT and adding the necessary TTL-pulses for the conditional operations necessary for teleportation.

A. Appendix

Bibliography

[1] A. Einstein, B.Podolsky, and N. Rosen. Can Quantum-Mechanical Description of Physical Reality Be Considered Complete ? *Phys. Rev.*, 47:777, May 1935.

[2] Erwin Schrödinger. Discussion of probability relations between separated systems. *Proc. Camb. Phil. Soc.*, 31:555–563, 1935.

[3] John S. Bell. On the Problem of Hidden Variables in Quantum Mechanics. *Rev. Mod. Phys.*, 38(3):447–452, July 1966.

[4] John S. Bell. On the Einstein-Podolsky-Rosen paradox. *Physics*, 1:195–200, 1964.

[5] J.S. Bell. *Speakable and unspeakable in quantum mechanics*. Cambridge University Press, 1987. A collection of Bell's papers.

[6] John F. Clauser, Michael A. Horne, Abner Shimony, and Richard A. Holt. Proposed experiment to test local hidden-variable theories. *Phys. Rev. Lett.*, 23(15):880, October 1969.

[7] Daniel M. Greenberger, Michael A. Horne, Abner Shimony, and Anton Zeilinger. Bell's theorem without inequalities. *Am. J. Phys.*, 58(12):1131–1143, December 1990.

[8] Alain Aspect, Philippe Grangier, and Gërard Roger. Experimental Realization of Einstein-Podolsky-Rosen-Bohm Gedankenexperiment: A New Violation of Bell's Inequalities. *Phys. Rev. Lett.*, 49(2):91, July 1982.

[9] Z. Y. Ou and L. Mandel. Violation of Bell's Inequality and Classical Probability in a Two-Photon Correlation Experiment. *Phys. Rev. Lett.*, 61(1):50, July 1988.

[10] Benjamin Schumacher. Quantum Coding. *Phys. Rev. A*, 51(4):2738, April 1995.

[11] David Bohm. *Quantum Theory*. Prentice Hall, 1951.

[12] Charles H Bennett, Gilles Brassard, Claude Crépeau, Richard Jozsa, Asher Peres, and William K. Wootters. Teleporting an Unknown Qauntum State via Dual Classical and Einstein-Podolsky-Rosen Channels. *Phys. Rev. Lett.*, 70(13):1895–1899, March 1993.

[13] William K. Wootters. Quantum entanglement as quantifiable resource. *Phil. Trans. R. Soc. Lond. A*, 356:1717–1731, 1998.

[14] Dik Bouwmeester, Jian-Wei Pan, Klaus Mattle, Manfred Einble, Harald Weinfurter, and Anton Zeilinger. Experimental quantum teleportation. *Nature*, 390:575–579, December 1997.

Bibliography

[15] D. Boschi, S. Branca, F. De Martini, L.Hardy, and S. Popescu. Experimental Realization of Teleporting an Unknown Pure Quantum State via Dual Classical and Eintein-Podolsky-Rosen Channels. *Phys. Rev. Lett.*, 80(6):1121–1125, February 1998.

[16] A. Furusawa, J. L. Sørensen, S. L. Braunstein, C. A. Fuchs, H. J. Kimble, and E.S. Polzik. Unconditional Quantum Teleportation. *Science*, 282:706–709, October 1998.

[17] M. A. Nielsen, E. Knill, and R. Laflamme. Complete quantum teleportation using nuclear magnetic resonance. *Nature*, 396:52–55, November 1998.

[18] R. P. Feynman. Simulating physics with computers. *Int. J. Theor. Phys.*, 21:467, 1982.

[19] R. P. Feynman. Quantum mechanical computers. *Foundantions of physics*, 16:507, 1982.

[20] D. Deutsch. Quantum theory, the Church-Turing principle and the universal quantum computer. *Proc. R. Soc. London A*, 400:96, 1985.

[21] Michael A Nielsen and Isaac L Chuang. *Quantum Computation and Quantum Information*. Cambridge University Press, 2000.

[22] D. Deutsch. Quantum computational networks. *Proc. R. Soc. London A*, 425(73), 1989.

[23] R. Cleve, A. Ekert, C. Macciavello, and M. Mosca. Quantum algorithms revisited. *Proc. R. Soc. Lond. A*, 454:339, 1998.

[24] L. K. Grover. A fast quantum mechanical algorithm for database search. In *Proc. 28th Annual ACM Symposium on the Theory of Computing*, page 212, 1996.

[25] Lov K. Grover. Quantum mechanics helps in searching for a needle in a haystack. *Phys. Rev. Lett.*, 79(2):325, 1997.

[26] P.W. Shor. Algorithms for Quantum Computation: Discrete logarithms and factoring. In *Proc. 35th Annual Symposium on Foundations of Computer Science*, 1994.

[27] Ronald L. Rivest, Adi Shamir, and Leonard M. Adleman. A Method for Obtaining Digital Signatures and Public-Key Cryptosystems. *Communications of the ACM*, 21(2):120–126, February 1978. available at http://theory.lcs.mit.edu/ rivest/publications.html.

[28] Richard Josza. *Geometric Issues in the Foundations of Science*, chapter Entanglement and Quantum Computation. Oxford University Press, 1997. also available at arxiv.org quant-ph/9707034.

[29] Artur Ekert and Richard Jozsa. Quantum algorithms: Entanglement-enhanced information processing. *Phil. Trans. R. Soc Lond A*, 356:1769–1782, 1998.

[30] M. Mosca, R. Jozsa, A. Steane, and A. Ekert. Quantum-enhanced information processing. *Phil. Trans. R. Soc. Lond. A*, 358:261–279, 2000.

[31] T.M. Forcer, A.J.G. Hey, D.A. Ross, and P.G.R. Smith. Superposition, entanglement and quantum computation. *Quantum Information and Computation*, 2(2):97–116, 2002.

[32] Richard Jozsa and Noah Linden. On the role of entanglement in quantum-computational speed-up. *Proc. R. Soc. Lond. A*, 459:2011–2032, 2003.

[33] P. W. Shor. Scheme for reducing decoherence in quantum computer memory. *Phys. Rev. A*, 52:2493, 1995.

[34] David P. DiVincenzo. The physical implementation of quantum computation. *Fortschr. Phys.*, 48:771–783, 2000.

[35] E. Knill, R. Laflamme, and G. J. Milburn. A scheme for efficient quantum computation with linear optics. *Nature*, 409:46, January 2001.

[36] P. Domokos, J. M. Raimond, M. Brune, and S. Haroche. Simple cavity-QED two-bit universalquantum logic gate: The principle and expected performances. *Phys. Rev. A*, 52(5):3554, 1995.

[37] J. I. Cirac and P. Zoller. Quantum Computations with Cold Trapped Ions. *Phys. Rev. Lett.*, 74(20):4091, May 1995.

[38] A. M. Steane. The ion-trap quantum information processor. *Appl. Phys. B - Lasers and Optics*, 64(6):623–642, 1997.

[39] Neil A. Gershenfeld. Bulk Spin-Resonance Quantum Computation. *Science*, 275:350, January 1997.

[40] L. M. K. Vandersypen and I. L. Chuang. NMR techniques for quantum control and computation. *Rev. Mod. Phys.*, 76:1037, 2004.

[41] J. E. Mooij, T. P. Orlando, L. Levitov, Lin Tian, Caspar H. van der Wal, and Seth Lloyd. Josephson Persistent-Current Qubit. *Science*, 285:1036, August 1999.

[42] J. Q. You, J. S. Tsai, and Franco Nori. Scalable Quantum Computing with Josephson Charge Qubits. *Phys. Rev. Letters*, 89:197902, October 2002.

[43] Yuriy Makhlin, Gerd Schön, and Alexander Shnirman. Quantum-state engineering with Josephson-junction devices. *Rev. Mod. Phys.*, 73(2):357, 2001.

[44] Daniel Loss and David P. DiVincenzo. Quantum computation with quantum dots. *Phys. Rev. A*, 57(1):120, January 1998.

[45] B. E. Kane. A silicon-based nuclear spin quantum computer. *Nature*, 393:133, May 1998.

[46] Lieven M. K. Vandersypen, Matthias Steffen, Gregory Breyta, Costantino S. Yannoni, Mark H. Sherwood, and Isaac L. Chuang. Experimental realization of Shor's quantum factoring algorithm using nuclear magnetic resonance. *Nature*, 414:883–887, December 2001.

[47] Warren S Warren. The usefulness of NMR quantum computing. *Science*, 277:1688, September 1997.

Bibliography

[48] S. L. Braunstein, C. M. Caves, R. Jozsa, N. Linden, S. Popescu, and R. Schack. Separability of Very Noisy Mixed States and Implications for NMR Quantum Computing. *Phys. Rev. Letters*, 83(5):1054, August 1999.

[49] Rüdiger Schack and Carlton M. Caves. Classical model for bulk-ensemble NMR quantum computation. *Phys. Rev. A*, 60(6):4354, December 1999.

[50] Noah Linden and Sandu Popescu. Good Dynamics versus Bad Kinematics: Is Entanglement Needed for Quantum Computation? *Phys. Rev. Letters*, 87(4):047901, July 2001.

[51] I. Chiorescu, Y. Nakamura, C. J. P. M. Harmans, and J. E. Mooij. Coherent quantum dynamics of a superconducting flux qubit. *Science*, 299:1869, March 1999.

[52] Y. Nakamura, Yu. A. Pashkin, and J. S. Tsai. Coherent control of macroscopic quantum states in a single-Cooper-pair box. *Nature*, 398:786, April 1999.

[53] Yu. A. Pashkin, T. Yamamoto, O. Astafiev, Y. Nakamura, D.V. Averin, and J.S. Tsai. Quantum oscillations in coupled charge qubits. *Nature*, 421:823, February 2003.

[54] T. Yamamoto, Yu. A. Pashkin, O. Astafiev, Y. Nakamura, and J. S. Tsai. Demonstration of conditional gate operation using superconducting charge qubits. *Nature*, 425:941–944, October 2003.

[55] R. McDermott, R. W. Simmonds, Matthias Steffen, K. B. Cooper, K. Cicak, K. D. Osborn, Seongshik Oh, D. P. Pappas, and John M. Martinis. Simultaneous state measurement of coupled Josephson phase qubits. *Science*, 307:1299, February 2005.

[56] J. M. Etzerman, R. Hanson, L. H. Willems van Beveren, B. Witkamp, L. M. K. Vandersypen, and L. P. Kouwenhoven. Single-shot read-out of an individual electron spin in a quantum dot. *Nature*, 430:431, July 2004.

[57] D. Jonathan, M. B. Plenio, and P. L. Knight. Fast quantum gates for cold trapped ions. *Phys. Rev. A*, 62:042307, 2000.

[58] Anders Sørensen and Klaus Mølmer. Quantum Computation with Ions in Thermal Motion. *Phys. Rev. Lett.*, 82(9):1971–1974, March 1998.

[59] C. Monroe, D. M. Meekhof, B. E. King, W. M. Itano, and D. J. Wineland. Demonstration of a Fundamental Quantum Logic Gate. *Phys. Rev. Lett.*, 75(25):4714, December 1995.

[60] Q. A. Turchette, C. S. Wood, B. E. King, C. J. Myatt, D. Leibfried, W. M. Itano, C. Monroe, and D. J. Wineland. Deterministic Entanglement of Two Trapped Ions. *Phys. Rev. Lett.*, 81(17):3631, October 1998.

[61] C. A. Sackett, D. Kielpinski, B. E. King, C. Langer, V. Meyer, C. J. Myatt, M. Rowe, Q. A. Turchette, W. M. Itano, D. J. Wineland, and C. Monroe. Experimental entanglement of four particles. *Nature*, 404:256–259, March 2000.

134

[62] D. Leibfried, B. DeMarco, V. Meyer, D. Lucas, M. Barrett, J. Britton, W.M. Itano, B. Jelenkovic, C. Langer, T. Rosenband, and D.J. Wineland. Experimental demonstration of a robust, high-fidelity geometric two ion-qubit phase gate. *Nature*, 422:412, March 2003.

[63] Hanns-Christoph Nägerl. *Ion Strings for Quantum Computation*. PhD thesis, Universität Innsbruck, September 1998.

[64] Christian F. Roos. *Controlling the quantum state of trapped ions*. PhD thesis, Universität Innsbruck, February 2000.

[65] Harald Rohde. *Experimente zur Quanteninformationsverarbeitung in einer linearen Ionenfalle*. PhD thesis, Universität Innsbruck, 2001.

[66] Stephan Gulde, Mark Riebe, Gavin P.T. Lancaster, Christoph Becher, Jürgen Eschner, Hartmut Häffner, Ferdinand Schmidt-Kaler, Isaac L. Chuang, and Rainer Blatt. Implementation of the Deutsch-Josza algorithm on an ion-trap quantum computer. *Nature*, 421:48, January 2003.

[67] F. Schmidt-Kaler, H. Häffner, M. Riebe, S. Gulde, G. P. T. Lancaster, T. Deuschle, C. Becher, C. F. Roos, J. Eschner, and R. Blatt. Realization of the Cirac-Zoller controlled-NOT quantum gate. *Nature*, 422:408–411, 2003.

[68] Stephan Timo Gulde. *Experimental Realization of Quantum Gates and the Deutsch-Josza Algorithm with Trapped $^{40}Ca^+$ Ions*. PhD thesis, Universität Innsbruck, March 2003.

[69] Adriano Barenco, Charles H Bennett, Richard Cleve, David P. DiVincenzo, Norman Margolus, Peter Shor, Tycho Sleator, John A. Smolin, and Harald Weinfurter. Elementary gates for quantum computation. *Phys. Rev. A*, 52(5):3457, November 1995.

[70] Robert Raussendorf and Hans J. Briegel. A One-Way Quantum Computer. *Phys. Rev. Lett.*, 86(22):5188, May 2001.

[71] I.L. Chuang and M.A. Nielsen. Prescription for experimental determination of the dynamics of a quantum black box. *J. Mod. Opt.*, 44(11-12):2455–2467, 1997. arXive e-print quant-ph/96100001.

[72] Asher Peres. Seperability Criterion for Density Matrices. *Phys. Rev. Lett.*, 77(8):1413, August 1996.

[73] William K. Wootters. Entanglement of Formation and Concurrence. *Quantum Information and Computation*, 1(1):27–44, 2001.

[74] Scott Hill and William K. Wootters. Entanglement of a Pair of Quantum Bits. *Phys. Rev. Lett.*, 78(26):5022, June 1997.

[75] William K Wooters. Entanglement of Formation of an Arbitrary State of Two Qubits. *Phys. Rev. Lett.*, 80(10):2245, March 1998.

[76] P. K. Ghosh. *Ion traps*. Clarendon Press, 1995.

[77] D. G. Enzer, M. M. Schauer, J. J. Gomez, M. S. Gulley, M. H. Holzscheiter, P. G. Kwiat, S .K. Lamoreaux, C. G. Peterson, V. D. Sandberg, D. Tupa, A. G. White, and R. J. Hughes. Observation of Power-Law Scaling for Phase Transitions in Linear Trapped Ion Crystals. *Phys. Rev. Lett.*, 85(12):2466, September 200.

[78] D.F.V. James. Quantum dynamics of cold trapped ions with application to quantum computation. *Appl. Phys. B*, 66:181–190, 1998.

[79] Andrew M. Childs and Isaac L. Chuang. Universal quantum computation with two-level trapped ions. *Phys. Rev. A*, 63:012306, January 2001.

[80] Rodney Loudon. *Quantum Theory of Light*. Oxford University Press, 1983.

[81] Eric D. Black. An introduction to Pound-Drever-Hall laser frequency stabilization. *Am. J. Phys.*, 69(1):79–87, January 2001.

[82] Gregor Thalhammer. Frequenzstabilisierung von Diodenlasern bei 850, 854 und 866 nm mit Linienbreiten im Kilohertz-Bereich. Master's thesis, Universität Innsbruck, Mai 1999. available at http://heart-c704.uibk.ac.at.

[83] Daniel Rotter. Photoionisation von Kalzium. Master's thesis, Universität Innsbruck, January 2003. available at http://heart-c704.uibk.ac.at.

[84] S. Gulde, D. Rotter, P. Barton, F. Schmidt-Kaler, R. Blatt, and W. Hogervorst. Simple and efficient photo-ionization loading of ions for precision ion-trapping experiments. *Applied Physics B*, 73:861–863, 2001.

[85] Technical Note: Introduction to Image Intensifiers for Scientific Imaging. Technical report, Roper Scientific, 2000. available at www.roperscientific.com.

[86] W. M. Itano, J. C. Bergquist, J. J. Bollinger, J. M. Gilligan, D. J. Heinzen, F. L. Moore, M. G. Raizen, and D. J. Wineland. Quantum projection noise: Population fluctuations in two-level systems. *Phys. Rev. A*, 47(5):3554, May 1993.

[87] Jürgen Eschner, Giovanna Morigi, Ferdinand Schmidt-Kaler, and Rainer Blatt. Laser cooling of trapped ions. *J. Opt. Soc. Am. B*, 20(5):1003, May 2003.

[88] Norman F. Ramsey. *Molecular Beams*. Oxford University Press, New York, 1985.

[89] H. Häffner, S. Gulde, M. Riebe, G. Lancaster, C. Becher, J. Eschner, F. Schmidt-Kaler, and Rainer Blatt. Precision Measurement and Compensation of Optical Stark Shifts for an Ion-Trap Quantum Processor. *Phys. Rev. Lett.*, 90(14):143602, April 2003.

[90] A. Kreuter, C. Becher, G.P.T. Lancaster, A.B. Mundt, C. Russo, H. Häffner, C. Roos, J. Eschner, F. Schmidt-Kaler, and R. Blatt. Spontaneuos Emission Lifetime of a Single Trapped Ca^+ Ion in a High Finesse Cavity. *Phys. Rev. Lett.*, 92(20):203002, May 2004.

[91] F. Schmidt-Kaler, S. Gulde, M. Riebe, T. Deuschle, A. Kreuter, G. Lancaster, C. Becher, J. Eschner, H. Häffner, and R. Blatt. The coherence of qubits based on single Ca$^+$ ions. *J. Phys. B*, 36:623–626, January 2003.

[92] K. Sengstock, U. Sterr, J. H. Müller, V. Rieger, D. Bettermann, and W. Ertmer. Optical Ramsey Spectroscopy on Laser Trapped and Thermal Mg-Atoms. *Appl. Phys. B*, 59:99, 1994.

[93] E. L. Hahn. Spin Echoes. *Phys. Rev.*, 80(4):580, November 1950.

[94] E. Hagley, X. Maître, G. Nogues, C. Wunderlich, M. Brune, J. M. Rainond, and S. Haroche. Generation of Einstein-Podolsky-Rosen Pairs of Atoms. *Phys. Rev. Lett.*, 79(1):1, July 1997.

[95] D. Kielpinski, V. Meyer, M. A. Rowe, C. A. Sackett, W. M. Itano, C. Monroe, and D. J. Wineland. A Decoherence-Free Quantum Memory Using Trapped Ions. *Science*, 291:1013, 2001.

[96] F. Schmidt-Kaler, H. Häffner, S. Gulde, G. Lancaster, J. Eschner, C. Becher, and R. Blatt. Quantized AC-Stark shifts and their use for multiparticle entanglement and quantum gates. *Europhys. Lett.*, 65(5):587–593, 2004.

[97] W. Dür, G. Vidal, and J. I. Cirac. Three qubits can be entangled in two inequivalent ways. *Phys. Rev. A*, 62:062314, December 2000.

[98] Manfred Eibl, Nikolai Kiesel, Mohamed Bourennane, Christian Kurtsiefer, and Harald Weinfurter. Experimental Realization of a Three-Qubit Entangled W-State. *Phys. Rev. Lett.*, 92:077901, February 2004.

[99] Jian-Wei Pan, Dik Bouwmeester, Matthew Daniell, Harald Weinfurter, and Anton Zeilinger. Experimental test of quantum nonlocality in three-photon Greenberger-Horne-Zeilinger entanglement. *Nature*, 403:515–519, February 2000.

[100] R. Laflamme, E. Knill, W. H. Zurek, P. Catasti, and S. V. S. Mariappan. NMR Greenberger-Horne-Zeilinger states. *Phil. Trans. R. Soc. Lond. A*, 356:1941–1948, 1998.

[101] Yoon-Ho Kim, Sergei P. Kulik, and Yanshua Shih. Quantum Teleportation of a Polarization State with a Complete Bell measurement. *Phys. Rev. Lett.*, 86(7):1370–1373, February 2001.

[102] M. D. Barrett, J. Chiaverini, T. Schaetz, J. Britton, W.M. Itano, J.D. Jost, E. Knill, C. Langer, D. Leibfried, R. Ozeri, and D.J. Wineland. Deterministic quantum teleportation of atomic qubits. *Nature*, 429:737–739, 2004.

[103] Sandu Popescu. Bell's inequalities versus Teleportation: What is Nonlocality ? *Phys. Rev. Lett.*, 72(6):797–799, February 1994.

[104] S. Massar and S. Popescu. Optimal Extraction of Information from Finite Quantum Ensembles. *Phys. Rev. Lett.*, 74(8), February 1995.

Bibliography

[105] N. Gisin. Nonlocality criteria for quantum teleportation. *Phys. Lett. A*, 210:157–159, January 1996.

[106] D. Kielpinski, C. Monroe, and D.J. Wineland. Architecture for a large-scale ion-trap quantum computer. *Nature*, 417:709–711, 2002.

[107] M. Zukowski, A. Zeilinger, M. A. Horne, and A. K. Ekert. Event-Ready-Detectors Bell Experiment via Entanglement Swapping. *Phys. Rev. Lett.*, 71(26):4287, 1993.

[108] Jian-Wei Pan, Dik Bouwmeester, Harald Weinfurter, and Anton Zeilinger. Experimental Entanglement Swapping: Entangling Photons That Never Interacted. *Phys. Rev. Lett.*, 80(18):3891, May 1998.

[109] Hartmut Häffner. private communications.

[110] D. Leibfried, M. D. Barrett, T. Schaetz, J. Britton, J. Chiaverini, W.M. Itano, J.D. Jost, C. Langer, and D.J. Wineland. Toward Heisenberg-limited apectroscopy with multiparticle entangled states. *Science*, 304:1476–1478, 2004.

[111] Daniel F. V. James, Paul G. Kwiat, William J. Munro, and Andrew G. White. Measurement of qubits. *Phys. Rev. A*, 64:052312, 2001.

[112] William H. Press, Saul A. Teukolsky, William T. Vetterling, and Brian P. Flannery. *Numerical Recipes in C*. Cambridge University Press, sec. edition, 1992.

[113] Philip R. Bevington. *Data Reduction and Error Analysis for the Physical Sciences*. McGraw-Hill, 1969.